

Copyright
by
Kelly Ann Stephani
2012

The Dissertation Committee for Kelly Ann Stephani
certifies that this is the approved version of the following dissertation:

**Development of a Hybrid DSMC/CFD Method for
Hypersonic Boundary Layer Flow over Discrete Surface
Roughness**

Committee:

David Goldstein, Supervisor

Philip Varghese, co-Supervisor

Robert Moser

Laxminarayan Raja

Deborah Levin

**Development of a Hybrid DSMC/CFD Method for
Hypersonic Boundary Layer Flow over Discrete Surface
Roughness**

by

Kelly Ann Stephani, B.Aero.E.&Mechanics; M.S.E.

DISSERTATION

Presented to the Faculty of the Graduate School of
The University of Texas at Austin
in Partial Fulfillment
of the Requirements
for the Degree of

DOCTOR OF PHILOSOPHY

THE UNIVERSITY OF TEXAS AT AUSTIN

May 2012

To my parents and Marco

Acknowledgments

The work presented in this dissertation could not have been possible without the guidance and support of many people, including the outstanding engineering faculty at UT Austin, as well as many colleagues and friends (both at UT and abroad), and of course, my family.

I first must thank my advisors, Prof. David Goldstein and Prof. Philip Varghese, for their guidance and support throughout my graduate studies. They were always happy to discuss new ideas related to this research, and they fostered a collaborative research environment. I benefited greatly from attending many conferences, spending extended periods at NASA-ARC and NASA-JSC, and participating in the CTR Summer Program, all of which they enthusiastically supported. I am grateful to the other members of my committee, Prof. Bob Moser, Prof. Laxminarayan Raja, and Prof. Deborah Levin, for their investment in my education and for their general interest in my research and progress. I especially thank Prof. Bob Moser for bringing the PECOS Center (and ultimately, Marco) to UT Austin.

I also benefited greatly from discussions with Prof. Elena Kustova, Prof. Thierry Magin, and Prof. Alejandro Garcia related to kinetic theory (and kinetic history, thanks to Thierry and Mimmo) and its significance within DSMC. Discussions with Alej guided the first steps towards the extension of

his method to include gas mixtures, and Thierry and Elena answered my many questions regarding the treatment of internal energy within this hybrid framework. I also thank Mike Wright, Todd White, Chun Tang and Mike Barnhardt at NASA Ames for their help with DPLR, and special thanks to Dinesh Prabhu for keeping Marco in check when I wasn't there. Thanks also to Jay LeBeau (a fellow Sconnie and Packer fan), Forrest Lumpkin and especially B  n  dicte Stewart at JSC and for their help with DAC, and thanks also to Chuck Campbell for the discussions regarding the STS BLT flight experiments.

I also thank my friends and colleagues within the CFPL group, and within the Aerospace Engineering Department and PECOS Center at UT Austin, as well as friends and collaborators at Universit  t Stuttgart, VKI, Stanford University, Texas A&M, and the University of Michigan. Thanks to everyone for many stimulating discussions and many wonderful memories at conferences and the Summer Program.

I could not have accomplished any of this without the love and support of my family, especially my Mom and Dad, as well as my sisters and brother, Erin, Sandra, Sara and Gregg (the newest engineer in the family!). Thank you for your constant love and encouragement, and for standing behind me every step of the way.

Finally, I wish to thank a very special person, (Professor) Marco Panesi, who has loved and supported me in so many ways. I am extremely lucky to have a relationship with someone who is incredibly supportive of (and in fact, shares) my research interests and career aspirations.

Development of a Hybrid DSMC/CFD Method for Hypersonic Boundary Layer Flow over Discrete Surface Roughness

Publication No. _____

Kelly Ann Stephani, Ph.D.
The University of Texas at Austin, 2012

Supervisors: David Goldstein
Philip Varghese

This work is focused on the development of a hybrid DSMC/CFD solver to examine hypersonic boundary layer flow over discrete surface roughness. The purpose of these investigations is to identify and quantify the non-equilibrium effects that influence the roughness-induced disturbance field and surface quantities of interest for engineering applications. To this end, a new hybrid framework is developed for high-fidelity hybrid solutions involving five-species air hypersonic boundary layer flow applications.

A novel approach is developed for DSMC particle generation at a hybrid interface for gas mixtures with internal degrees of freedom. The appropriate velocity distribution function is formulated in the framework of Generalized

Chapman-Enskog Theory, and includes contributions from species mass diffusion, shear stress and heat fluxes (both translational and internal) on the perturbation of the equilibrium distribution function. This formulation introduces new breakdown parameters for use in hybrid DSMC/CFD applications, and the new sampling algorithm allows for the generation of DSMC internal energies from the appropriate non-equilibrium distribution for the first time in the literature. The contribution of the internal heat fluxes to the overall perturbation is found to be of the same order as the stress tensor components, underscoring the importance of DSMC particle generation from the Generalized Chapman-Enskog distribution.

A detailed comparison of the transport coefficients is made between the DSMC and CFD solvers, and a general best-fit approach is developed for the consistent treatment of diffusion, viscosity and thermal conductivity for a five-species air gas mixture. The DSMC VHS/VSS model parameters are calibrated through an iterative fitting approach using the Nelder-Mead Simplex Algorithm. The VSS model is found to provide the best fit (within 5% over the temperature range) to the transport models used in the CFD solver. The best-fit five-species air parameters are provided for general use by the DSMC community, either for hybrid applications or to provide improved consistency in general DSMC/CFD applications.

This hybrid approach has been applied to examine hypersonic boundary layer flow over discrete surface roughness for a variety of roughness geometries and flow conditions. An (asymmetric) elongated hump geometry and (sym-

metric) diamond shaped roughness geometry are examined at high and low altitude conditions. Detailed comparisons among the hybrid solution and the CFD no-slip and slip wall solutions were made to examine the differences in surface heating, translational/vibrational non-equilibrium in the flow near the roughness, and the vortex structures in the wake through the Q-criterion. In all cases examined, the hybrid solution predicts a *lower* peak surface heating to the roughness compared to either CFD solution, and a *higher* peak surface heating in the wake due to vortex heating. The observed differences in vortex heating are a result of the predicted vortex structures which are highlighted using the Q-criterion. The disturbance field modeled by the hybrid solution organizes into a system of streamwise-oriented vortices which are slightly stronger and have a greater spanwise extent compared to the CFD solutions. As a general trend, it was observed that these *differences* in the predicted heating by the hybrid and CFD solutions *increase* with increasing Knudsen number. This trend is found for both peak heating values on the roughness and in the wake.

Table of Contents

Acknowledgments	v
Abstract	vii
Nomenclature	xiv
List of Tables	xvii
List of Figures	xviii
Chapter 1. Introduction	1
1.1 Motivation	1
1.2 Attributes of Hypersonic Boundary Layer Flow over Discrete Surface Roughness	3
1.3 Molecular Nature of Gases	6
1.4 Hybrid Methods for Multiscale Flows	9
1.5 Overview	10
1.5.1 Scope of Dissertation	11
1.5.2 Outline	13
Chapter 2. Kinetic Framework of Hybrid Method and Numer- ical Flow Solvers	15
2.1 Overview	15
2.2 Kinetic Theory	16
2.2.1 Boltzmann Equation	16
2.2.2 Chapman-Enskog Theory and the Navier-Stokes Equations	18
2.2.3 Collision Integrals and Transport Coefficients	21
2.3 CFD Method	26
2.3.1 DPLR solver for continuum flows	27

2.3.2	Transport Models	29
2.3.3	Internal Energy Exchange and Relaxation	32
2.4	The Direct Simulation Monte Carlo Method	33
2.4.1	DAC solver for rarefied flows	34
2.4.2	Collision cross section models	38
2.4.3	Internal Energy Exchange and Relaxation	39
2.5	Hybrid Approaches for Continuum/Rarefied Flows	40
2.6	Summary	44
Chapter 3.	Generation of the Hybrid Solution	46
3.1	Overview	46
3.2	Hybrid Particle Generation	47
3.2.1	Volume and Surface Reservoir Approaches	47
3.3	Particle generation using a non-equilibrium surface reservoir approach	49
3.3.1	Surface reservoir approach for a simple gas	49
3.3.2	Surface reservoir approach for a gas mixture with internal degrees of freedom	55
3.4	Evaluation of the breakdown parameters in a five-species air gas mixture	61
3.4.1	Hypersonic 2-D boundary layer flow	63
3.4.2	Hypersonic flow over a cylinder (normal shock flow)	69
3.5	Summary	73
Chapter 4.	Consistent Treatment of Transport Coefficients	75
4.1	Overview	75
4.2	Transport Properties in CFD and DSMC	75
4.3	Consistent Treatment of Transport Properties in DSMC and CFD Solvers	79
4.3.1	Representation of Transport Properties in DSMC: VHS/VSS Collision Cross Section Models	79
4.3.2	Generation of Best-Fit VHS/VSS Parameters	85
4.4	Results	91
4.4.1	Equilibrium Composition and Transport Coefficients of Five-species Air	91

4.4.2	Collision-Averaged Best-Fit Parameters: VHS/VSS Collision Models	93
4.4.3	Collision-Specific Best-Fit Parameters: VHS/VSS Collision Models	99
4.4.4	Extension to Chemical Non-equilibrium	105
4.5	Summary	112
Chapter 5. Application to Hypersonic Boundary Layer Flow Over Discrete Surface Roughness		115
5.1	Overview	115
5.2	Hybrid and CFD Solutions	116
5.2.1	Flow Conditions and Roughness Geometries	116
5.2.2	Convergence Requirements	126
5.3	3D Flowfield Solutions: Flow Features, Breakdown Surfaces and Hybrid Interface Location	130
5.4	Asymmetric Geometry Configuration	142
5.4.1	Flowfield comparisons at 80 km	142
5.4.2	Local surface heating at 80 km	146
5.4.3	Flowfield comparisons at 60 km	152
5.4.4	Local surface heating at 60 km	156
5.5	Symmetric Geometry Configuration	162
5.5.1	Flowfield comparisons at 80 km	162
5.5.2	Local surface heating at 80 km	165
5.6	Summary	171
Chapter 6. Conclusions		177
6.1	Summary	177
6.2	Contributions	182
6.3	Future Considerations	184
6.3.1	Transport properties: extension to weakly ionized flows	184
6.3.2	Finite-rate chemistry	185
6.3.3	Comparative Assessment of CFD/Hybrid Solutions through Bi-Global Stability Analysis of Base Flows	187
Appendices		189

Appendix A. Sampling of the non-equilibrium surface reservoir distributions	190
Appendix B. Perturbation expressed by flux quantities	192
Appendix C. Formulation of Collision Integrals with VHS/VSS Cross Sections	197
Appendix D. Nelder-Mead Initial Conditions and Convergence History Example	201
Appendix E. Computational Cost of CFD/Hybrid Solutions	204
Bibliography	206
Vita	219

Nomenclature

β	inverse most probable thermal speed
\mathbf{C}	thermal velocity vector, $\mathbf{C} = (C_x, C_y, C_z)$
$\delta_{0.99h}$	boundary layer thickness based on enthalpy
ϵ_{rot}	rotational energy
ϵ_{vib}	vibrational energy
$\Gamma(\mathbf{C})$	Chapman-Enskog perturbation function
$\Gamma_s(\mathbf{C}, \mathcal{E}_{int})$	Generalized Chapman-Enskog perturbation function, $s \in \mathbb{S}$
\mathbb{D}_s	scaled diffusion flux, $s \in \mathbb{S}$
\mathbb{S}	species in gas mixture
\mathbf{g}	scaled relative collision speed, $\mathbf{g} = \left(\frac{m}{2k_bT}\right)^{1/2} g$
\mathcal{E}_{int}	scaled internal (rotational or vibrational) energy
\mathcal{C}_i	scaled particle thermal velocity components, $i \in (x, y, z)$
\mathcal{R}_u	uniformly distributed random number $\in [0, 1)$
μ	coefficient of viscosity
$\bar{\mathcal{E}}_{int}$	scaled average internal energy
$\phi_{CE}(\mathbf{C})$	Chapman-Enskog perturbation

$\phi_{GCE,s}(\mathbf{C}, \mathcal{E}_{int})$	Generalized Chapman-Enskog perturbation, $s \in \mathbb{S}$
$\sigma d\Omega$	differential cross section
τ_{ij}	scaled shear stress tensor components, $i, j \in (x, y, z)$
Θ_v	characteristic vibrational temperature of species s
$\tilde{q}_{int,i,s}$	scaled internal heat flux, $i \in (x, y, z)$, $s \in \mathbb{S}$
A	perturbation amplitude parameter
B	breakdown parameter
C_i	particle thermal velocity components, $i \in (x, y, z)$
c_{int}	internal specific heats (rotational or vibrational)
dC_i	differential thermal velocity component
f	velocity distribution function
$f^{(0)}(\mathbf{C})$	Maxwellian distribution function
$f_s^{(0)}(\mathbf{C}, \mathcal{E}_{int})$	Maxwell-Boltzmann distribution function
$f^{(1)}(\mathbf{C})$	Chapman-Enskog distribution function for simple gases
$f_{SR}^{(1)}(\mathbf{C})$	Chapman-Enskog surface reservoir distribution function for simple gases
g	relative collision speed
g_{int}	rotational or vibrational degeneracy
k_b	Boltzmann's constant
K_{tr}	translational thermal conductivity

m	molecular mass
n	number density
p	pressure
q_i	scaled heat flux vector components, $i \in (x, y, z)$
Q_{SR}	surface reservoir macroscopic quantities
R	cylinder radius of curvature
s	species, $s \in \mathbb{S}$
T_w	wall temperature
T_{rot}	rotational temperature
T_{tr}	translational temperature
T_{vib}	vibrational temperature
u, v, w	bulk velocity components
x, y, z	Cartesian coordinate directions
Z_{int}	internal partition function, $Z_{int} = Z_{rot}Z_{vib}$

List of Tables

3.1	Freestream Conditions	63
4.1	Collision-Averaged VHS/VSS Parameters (Fits to Transport Coefficients)	97
4.2	Collision-Specific VHS/VSS Parameters (Fits to Transport Coefficients)	104
4.3	Collision-Averaged/Collision-Specific VSS Parameters (Fits to Collision Integrals)	110
5.1	Boundary layer edge conditions	120
5.2	Computational length scales (Geometry and CFD/hybrid domains)	123
5.3	Total surface heating (asymmetric geometry (80 km))	153
5.4	Total surface heating (asymmetric geometry (60 km))	161
5.5	Total surface heating (symmetric geometry (80 km))	168
D.1	Predicted values of VSS scattering exponent	202
E.1	Computational Summary of CFD/Hybrid Simulations	204

List of Figures

1.1	Shuttle tile with integrated protuberance (pre-flight).	2
1.2	STS-119 BLT Flight Experiment.	2
1.3	Vortex system formed upstream of hemispherical bump in M=3.7 flow.	4
1.4	Temperature contours of M=3.7 flow past hemispherical bump (slices at spanwise center (left), planview (right)).	5
1.5	Local Knudsen number limits of molecular and continuum models.	7
2.1	DAC computational domain with Level-I and Level-II cells and triangulated surface geometry.	37
3.1	Schematic of surface reservoir comprised of fluxing triangles.	50
3.2	Equilibrium surface reservoir velocity distribution functions.	50
3.3	Schematic of sampling procedure for non-equilibrium surface reservoir distribution.	54
3.4	Breakdown parameters and perturbation profile through a hypersonic 2-D boundary layer.	65
3.5	Breakdown parameters and perturbation profile through a hypersonic 2-D boundary layer.	66
3.6	Breakdown parameters along the stagnation streamline.	71
3.7	Breakdown parameters along the stagnation streamline.	72
4.1	Composition and transport properties of equilibrium five-species air	92
4.2	Comparison of diffusion coefficients using collision-averaged fitting approach	94
4.3	Comparison of viscosity coefficients using collision-averaged fitting approach	95
4.4	Comparison of thermal conductivity coefficients using collision-averaged fitting approach	96
4.5	Comparison of diffusion coefficients using collision-specific fitting approach	100

4.6	Comparison of viscosity coefficients using collision-specific fitting approach	101
4.7	Comparison of thermal conductivity coefficients using collision-specific fitting approach	102
4.8	Comparison of diffusion coefficients using collision-specific fitting approach for non-equilibrium conditions	107
4.9	Comparison of viscosity coefficients using collision-specific fitting approach for non-equilibrium conditions	108
4.10	Comparison of thermal conductivity coefficients using collision-specific fitting approach for non-equilibrium conditions	109
5.1	ISS/lunar descent trajectories	117
5.2	Shuttle Orbiter with reference point of STS-119 BLT boundary layer trip.	118
5.3	2D flat plate boundary layer profiles based on edge conditions at STS-119 reference point.	119
5.4	Characteristic lengths of asymmetric geometry and CFD mesh.	121
5.5	Characteristic lengths of symmetric geometry and CFD mesh.	124
5.6	cell Reynolds numbers determined from near-wall cells.	128
5.7	Convergence criteria in DSMC simulations.	130
5.8	Disturbance flowfield and regions of strong non-equilibrium generated by asymmetric roughness.	131
5.9	Surface heating and regions of strong non-equilibrium generated by asymmetric roughness.	134
5.10	Disturbance flowfield and regions of strong non-equilibrium generated by symmetric roughness.	137
5.11	Surface heating and regions of strong non-equilibrium generated by symmetric roughness.	138
5.12	Hybrid domain interface boundaries.	140
5.13	Breakdown parameter profiles taken from hybrid interface boundaries	140
5.14	Streamwise velocity contours and corresponding vortex pairs in wake of asymmetric roughness at 80 km.	143
5.15	Translational/vibrational thermal non-equilibrium in flow surrounding asymmetric roughness at 80 km.	144
5.16	Surface heating generated by asymmetric roughness at 80km.	147

5.17	Schematic of surface heating acquired at various streamwise locations for asymmetric roughness.	148
5.18	Spanwise profiles of surface heating taken at various streamwise locations for asymmetric roughness at 80 km.	151
5.19	Streamwise velocity contours and corresponding vortex pairs in wake of asymmetric roughness at 60 km.	155
5.20	Translational/vibrational thermal non-equilibrium in flow surrounding roughness at 60 km.	155
5.21	Surface heating generated by asymmetric roughness at 60 km.	158
5.22	Spanwise profiles of surface heating taken at various streamwise locations for asymmetric roughness at 60 km.	160
5.23	Streamwise velocity contours and corresponding vortex pairs in wake of symmetric roughness at 80 km.	163
5.24	Translational/vibrational thermal non-equilibrium in flow surrounding symmetric roughness at 80 km.	164
5.25	Surface heating generated by symmetric roughness at 80km. .	166
5.26	Schematic of surface heating acquired at various streamwise locations for symmetric roughness.	167
5.27	Spanwise profiles of surface heating taken at various streamwise locations for symmetric roughness at 80 km.	169
5.28	Roughness peak heating as a function of local Knudsen number.	174
5.29	Peak heating in the wake as a function of Knudsen number. .	175
D.1	Relative error of VSS exponent as a function of iteration . . .	203

Chapter 1

Introduction

1.1 Motivation

Much of the motivation for this work is driven by the challenges encountered in predicting roughness-induced heating augmentation during the Boundary Layer Transition (BLT) Flight Experiments that were designed and flown as part of the STS-119, STS-125, and STS-128 missions [26]. A discrete protuberance was integrated into the shuttle tile material (Figure 1.1) for the BLT flight experiments, and this tile was affixed to the port side wing on the Orbiter belly. The surrounding tiles were instrumented with pressure transducers and thermocouples in efforts to characterize the onset of boundary layer transition, and to measure the heating augmentation to the shuttle surface as a result of this event (Figure 1.2). *A priori* calculations [8] made by high-fidelity Navier-Stokes solvers indicated peak heating on the protuberance that was four times higher than the peak heating measured during the flight experiments. The undisturbed boundary layer flow was expected to be within the continuum regime where the Navier-Stokes solution would be valid. The presence of the roughness, however, introduces local flowfield gradients including the formation of a shock, shear layer, and vortex structures. Under these conditions, the use of the Navier-Stokes solver in the flow region



Figure 1.1: Shuttle tile with integrated protuberance (pre-flight).

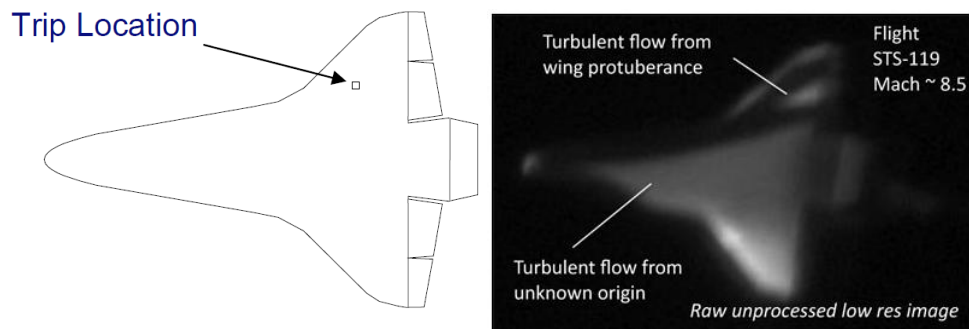


Figure 1.2: STS-119 BLT Flight Experiment.

surrounding the roughness is questionable, and a non-equilibrium flow solver such as DSMC is more appropriate. In order to investigate the importance of non-equilibrium effects, this work is focused on the development of a hybrid DSMC/CFD solver for application to hypersonic boundary layer flow over discrete surface roughness.

1.2 Attributes of Hypersonic Boundary Layer Flow over Discrete Surface Roughness

The disturbance field generated by hypersonic flow over discrete roughness shares several attributes with incompressible boundary layer flows. As an undisturbed laminar boundary layer (compressible or incompressible) approaches the roughness, the solid protuberance from the surface surface imposes an impulsive force on the flow. A complex disturbance field is generated as the flow is pushed in both spanwise directions to pass along the sides of the roughness, or is ejected upwards to pass over the top of the roughness. A recirculation region as well as a horseshoe vortex system form upstream of the geometry near the base (Figure 1.3). The legs of the vortices wrap around the roughness which appear as counter-rotating streamwise-oriented vortex pairs that extend downstream into the wake. A shear layer forms over the top of the roughness, and at sufficiently high Reynolds numbers, this shear layer becomes unsteady, resulting in a periodic shedding of vortices that interact with the legs of the horseshoe vortices downstream of the roughness. A recirculation region may form immediately behind the roughness, and the wake flow is initially dominated by low speed flow, forming a velocity deficit immediately downstream of the roughness. The counter-rotating vortices work to pull high-speed flow from the outer boundary layer down toward the wall in the portion of the wake between the vortex pair. In the same way, low-speed flow near the wall is lifted upwards in the region of the wake outside of the vortex pair. This mechanism works against the velocity deficit, and after a sufficient dis-

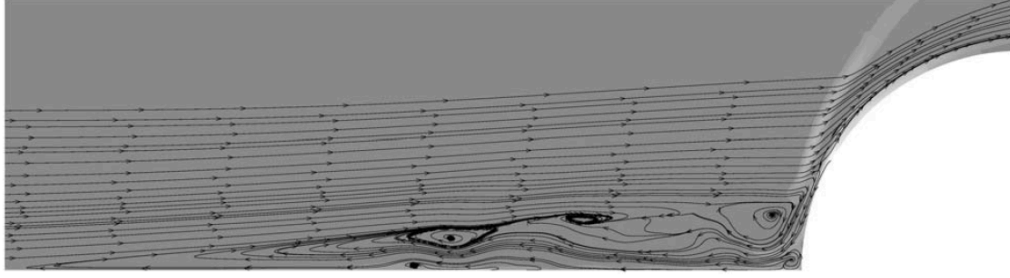


Figure 1.3: Vortex system formed upstream of hemispherical bump in $M=3.7$ flow.

tance downstream of the roughness (referred to as the *inversion length*), the wake flow becomes dominated with high-speed flow due to the presence of the streamwise vortices.

Additional flow features arise when considering hypersonic boundary layer flow over roughness, due to compressibility effects. A bow shock forms on the windward side of the roughness, forming a complex shock-boundary layer interaction region upstream of the roughness (Figure 1.4). After the flow is processed by the shock, an expansion region forms in order to turn the flow as it passes over the leeward portion of the roughness, and a relatively weak recompression shock forms to turn the flow parallel to the wall in the wake of the roughness. These structures introduce local pressure gradients which are imposed on the disturbance field surrounding the roughness. The vortex structures (mentioned previously) that are induced by the presence of the roughness not only impact the wake flow, but they also have a profound impact on the surface properties (including shear stress and heat flux) in the

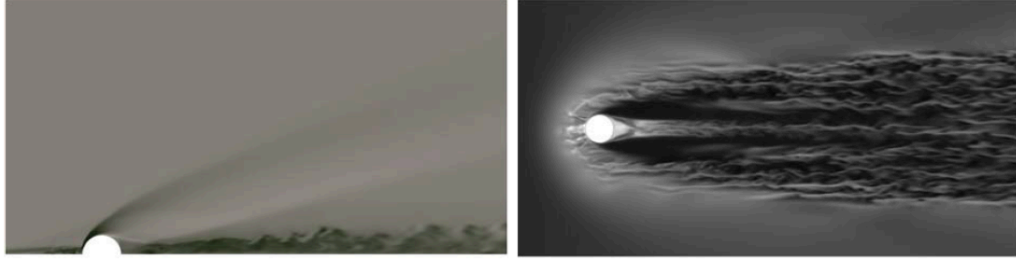


Figure 1.4: Temperature contours of $M=3.7$ flow past hemispherical bump (slices at spanwise center (left), planview (right)).

wake of the roughness. In addition to these new flow structures, the very nature of hypersonic flows introduces new thermo-chemical phenomena that must be considered, including vibrational excitation, chemical reactions, and other real gas effects.

The roughness-induced disturbance field generated at the surface of a vehicle during hypersonic re-entry or high-altitude flight is characterized by multi-scale, multi-physics phenomena, and may include regions of both near-continuum and non-equilibrium flow. In general, the most significant non-equilibrium effects are observed within boundary layers and shock waves, where the gradient length scales of macroscopic flow quantities are comparable to the local molecular mean free path. While the details of non-equilibrium processes are established at the microscopic scale, their influence on the macroscopic description of the overall system, including heat loads, aerodynamics, and gas/surface interactions, can be substantial. Thus, it is necessary to accurately model these multi-scale flows in order to inform important design decisions.

1.3 Molecular Nature of Gases

At the most detailed level, the state of a system is determined by the random thermal motion of molecules and interaction of molecules through collisions. Within the system, each molecule possesses the intrinsic properties of mass, momentum and energy, and each molecular interaction is determined according to the aggregate external force fields (i.e., *interaction potentials*) of the participating molecules. A collisional encounter results in an exchange of mass (in the case of chemical reactions), momentum and translational and internal energy between the molecules. The subsequent post-collision motion of the molecules serves to diffuse the mass, momentum and energy throughout the fluid volume.

Depending on the density of the gas, simplifying assumptions may be made regarding the motion of molecules between collisions and the types of collisions that occur. This work is restricted to the consideration of dilute gases, and so it is assumed that the molecular dimensions are small relative to the mean distance between molecules. Furthermore, it is assumed that the overwhelming majority of molecular collisions in dilute gases may be regarded as binary.

In the absence of transport fluxes, the thermal velocities of molecules in the gas follow an equilibrium *Maxwellian* velocity distribution. This corresponds to the inviscid limit in which the local gradient-based Knudsen number

$$Kn_{\nabla Q} = \frac{\lambda}{Q/\nabla Q} \quad (1.1)$$

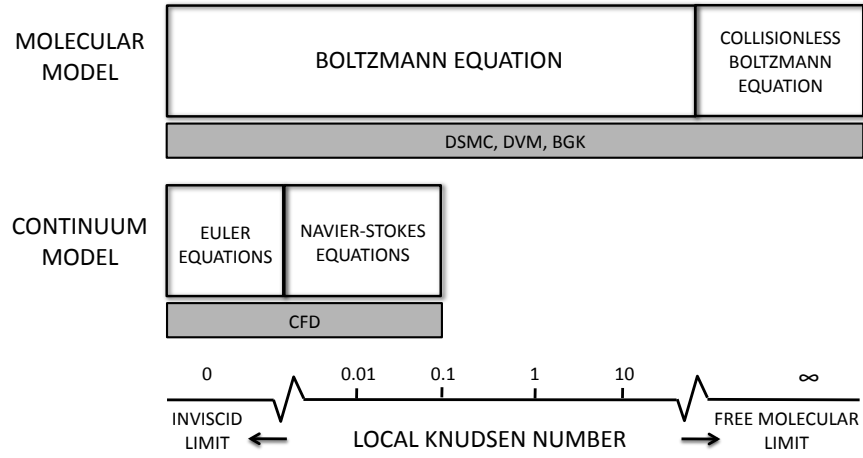


Figure 1.5: Local Knudsen number limits of molecular and continuum models. (corresponding solution methods are shown in gray)

defined as the ratio of the molecular mean free path to a characteristic gradient-based length scale, goes to zero. From a macroscopic point of view, this limit corresponds to the inviscid Euler equations (Figure 1.5).

When gradients in macroscopic properties within the flowfield are not negligible, translational nonequilibrium gives rise to mass diffusion, viscous stresses and heat conduction in the gas. In cases where the local Knudsen number remains less than approximately 0.1, the velocity distribution describing the thermal velocities of molecules in the gas exhibits a small departure from the equilibrium distribution. In this regime, a continuum representation of the flow is still valid, but the Navier-Stokes equations are required for an accurate solution. As will be discussed in Chapter 2, the closure of

the Navier-Stokes equations is made through the expression of the transport fluxes in terms of gradients of macroscopic quantities (e.g., mass diffusion flux, viscous stresses and Fourier heat flux). Furthermore, the formulation of the Navier-Stokes conservation equations via the Chapman-Enskog expansion requires that the departure of the velocity distribution from equilibrium is small. Thus, a continuum description of a flowfield through the solution of the Navier-Stokes equations is valid so long as the macroscopic expressions for the transport fluxes hold.

The Navier-Stokes equations begin to fail in regions of strong translational nonequilibrium where $Kn_{\nabla Q} > 0.1$, such as within a shock or boundary layer flow. In these regions, the gradients of the macroscopic quantities become sufficiently large such that their length scale is of the same order as the local molecular mean free path. The expressions for the transport terms in the Navier-Stokes equations are no longer adequate. Under these circumstances, higher fidelity kinetics-based methods for the solution of the Boltzmann equation must be used to solve the flowfield at the microscopic scale. A kinetics-based approach allows for a microscopic or molecular representation of the gas, in that the position, velocity and internal energy states of the molecules are tracked. This molecular information is then used to provide a macroscopic description of the gas, without making any assumptions *a priori* regarding the underlying velocity distribution describing the molecules. This feature makes kinetics-based approaches highly desirable for the accurate solution of nonequilibrium or rarefied flows. These approaches are valid across the full

range of flows, from continuum to free-molecular (Figure 1.5).

1.4 Hybrid Methods for Multiscale Flows

Many hypersonic flows of interest to the engineering community lie within the continuum regime (i.e., $Kn_{\nabla Q} < 0.1$) where the flow is near equilibrium, and the Navier-Stokes conservation equations may be applied. Methods for the solution of the Navier-Stokes equations using computational fluid dynamics (CFD) have been widely developed and successfully applied for a range of aerospace applications, as they allow for a reasonably accurate and relatively efficient solution of complex high-enthalpy flow problems. CFD methods have been extended to include models for multiphysics phenomena, including thermal and chemical nonequilibrium, ionization and radiation, surface thermal and velocity slip, surface catalysis and ablation, as well as models for transitional and turbulent flows.

As mentioned previously, the Navier-Stokes solutions fail in regions of strong translational nonequilibrium. Therefore, the application of CFD solvers for flowfield solutions involving regions of nonequilibrium, such as shocks and boundary layers, is not appropriate, and the accuracy of the CFD solutions is questionable. In these regions, however, high-fidelity kinetics-based methods, such as direct simulation Monte Carlo (DSMC) [2], may be used to accurately capture non-equilibrium effects that drive important thermo-chemical processes. The DSMC method was introduced as a direct, physical approach for the solution of the Boltzmann equation, by emulating the discrete molecu-

lar structure of the gas using simulated particles. Although this work focuses on the DSMC method, it should be mentioned that other approaches have been developed for the approximate solution of the Boltzmann equation, such as discrete velocity methods (DVM) and the Bhatnagar-Gross-Krook (BGK) model.

The DSMC method has also been widely developed and includes models for a variety of collision cross sections, as well as models for internal energy exchange and relaxation, several chemistry models for dissociation, recombination and exchange reactions, surface catalysis and high-fidelity surface interaction models, and approaches for including effects from ionization and radiation. While the DSMC solution is valid from free-molecular to continuum regimes, the time step and cell size requirements become computationally prohibitive in the continuum limit. It is precisely in this regime, however, that a CFD solver may be employed. Thus, a combined DSMC/CFD hybrid approach is often adopted as a way to capture rarefaction effects by solving regions of translational nonequilibrium using DSMC, while capitalizing on the computational efficiency of CFD in near equilibrium regions.

1.5 Overview

While hybrid methods have been developed and successfully applied for a variety of flow scenarios, the detailed formulation of these approaches limits their application to simple (single species, monatomic) gases. Many hypersonic flows of interest to the engineering community, however, require the solution

of a system involving gas mixtures with internal energy in addition to complex physical phenomena. As evident by the post-flight analyses of the BLT Flight experiments, the challenges faced in modeling the flow over discrete surface roughness underscore the need for improved hybrid and multiscale approaches.

1.5.1 Scope of Dissertation

The objective of this work is to develop a general, consistent hybrid DSMC/CFD approach, with application to hypersonic boundary layer flow over discrete surface roughness. The hybrid approach allows for an efficient yet detailed solution of the nonequilibrium disturbance field generated by the roughness. This capability is necessary in order to understand and quantify the influence of rarefaction in the multiscale flow application examined in this work. The flow conditions examined are representative of typical laminar boundary layer edge conditions on the shuttle orbiter belly during early stages of a reentry trajectory. Therefore, the hybrid approach presented here has been extended to include effects of species diffusion and heat flux from internal energy modes for application in a five species air mixture. Ionized or chemically reacting flows are not considered in the present work.

Hybrid methods require a careful treatment of the physical models employed in the CFD and DSMC solvers. Although significant modification of the DSMC solver was required for this hybrid application, this work utilized (where possible) the existing models available within the DSMC and CFD solvers. This work introduces an approach for achieving consistency in the

transport properties of mass diffusion, viscosity and thermal conductivity between the two solvers. A consistent approach for vibrational thermal relaxation is also employed. A novel approach for hybrid particle generation is also presented for the five species air mixture, which can be applied for general gas mixtures with internal energy. This approach allows for the sampling of particle internal energies from a non-Boltzmann distribution for the first time in the literature. Additional modifications were made to the DSMC solver to allow for the large scale simulations necessary for the three-dimensional boundary layer flow simulations. The major efforts and contributions of this dissertation are summarized below.

- Devised an approach for achieving consistency in transport properties between DSMC and CFD solvers, including species diffusion, mixture viscosity, and translational and internal thermal conductivities.
- Formulated a novel approach for hybrid particle generation in nonequilibrium flows involving gas mixtures with internal energy, based on Generalized Chapman-Enskog Theory.
- Implemented Millikan and White thermal relaxation rates (with Gimelshein correction factor) and Park's high temperature correction in DSMC solver and libraries.
- Modified DSMC solver to examine influence of near-wall cell population on the predicted surface heat flux.

- Implemented new hybrid particle generation algorithm in DSMC libraries, preprocessors and solvers.
- Modified DSMC libraries, preprocessors and solvers to enable simulations with unprecedented number of simulated particles.
- Generated and compared continuum and hybrid flowfield solutions for various roughness geometries and conditions relevant to aerospace applications.
- Analyzed disturbance velocity field in wake of roughness using Q-criterion for vortex structures in CFD and hybrid solutions; established relationship between vortex strength/size and observed surface heating in the wake of roughness.
- Established general trends in the differences in CFD/hybrid predicted peak surface heating with respect to the local Knudsen number.

1.5.2 Outline

The discussion in this chapter has provided an introduction to the motivation of this work, the challenges that are faced in modeling multiscale, multiphysics flows, and the tools that must be developed to address these problems. Chapter 2 outlines the relevant concepts from kinetic theory upon which the hybrid framework is constructed, as well as the details of the CFD and DSMC solvers used in this work. Chapters 3 and 4 discuss in detail the generation of the hybrid solution, including a new algorithm for hybrid particle

generation and corresponding breakdown criteria. A consistent treatment of the transport properties is also discussed. In Chapter 5, the three-dimensional hybrid flowfield solutions are presented in which a variety of surface roughness geometries and conditions are examined. Convergence requirements of both the CFD and hybrid solutions are discussed, and comparisons are made between the flowfield and predicted surface flux quantities generated by the CFD and hybrid solutions. Computational requirements of the CFD and hybrid solutions are also presented. The results from this work are concluded in Chapter 6, and recommendations are made for future work in this field.

Chapter 2

Kinetic Framework of Hybrid Method and Numerical Flow Solvers

2.1 Overview

In this chapter, the governing equations used to model the flowfields of interest from both a continuum and molecular perspective are presented. The scope and progression of the material discussed in this chapter is intended to serve two purposes. The first is to provide a molecular interpretation of macroscopic gas dynamics and transport processes, and to establish the relationship between (and limitations of) the continuum and kinetic approaches used in this work. The second purpose of this chapter is to develop the fundamental concepts established from kinetic theory that provide the framework from which the hybrid approaches, outlined in Chapters 3 and 4, are constructed.

This chapter begins with a brief discussion of the Boltzmann equation and the equilibrium Maxwellian distribution. The focus is then shifted to nonequilibrium gas flows, with emphasis on Chapman-Enskog Theory. The Chapman-Enskog perturbation function is introduced, and the significance of the Chapman-Enskog perturbation within the hybrid framework is discussed. The formulation of the Navier-Stokes equations from the Chapman-Enskog

expansion is presented next. An important relationship is established between the molecular collision processes described by the collision integrals and the continuum definition of transport fluxes.

The next sections present the CFD and DSMC solution methods used in this work, and the physical models employed within each solver. Finally, a review of previous work in the area of hybrid CFD/DSMC approaches for continuum/rarefied flows is presented.

2.2 Kinetic Theory

2.2.1 Boltzmann Equation

For a simple (dilute gas) system comprising a single, monatomic gas species, the Boltzmann equation may be used to provide a description of the evolution of this system in terms of the velocity distribution function, $f(C)$. The Boltzmann equation (neglecting external forces) is expressed in the form

$$\frac{\partial}{\partial t}[nf(C)] + \mathbf{C} \cdot \frac{\partial}{\partial \mathbf{x}}[nf(C)] = \int_{-\infty}^{\infty} \int_0^{4\pi} n^2 (f' f'_1 - f f_1) g \sigma d\Omega d\mathbf{C}_1. \quad (2.1)$$

The dependent variable, f , in this equation represents the fraction of molecules that belong to a particular velocity class at a specified time and spatial location.

The first term on the left hand side of (2.1) represents the rate of change of the number of molecules belonging to a specified velocity class in a differential volume in physical and velocity space. This rate of change has

contributions from a convection of molecules across the differential volume surface (second term on left hand side of (2.1)), as well as from particle collisions, according to the collision operator on the right hand side of (2.1). The collision operator expresses the effect of two competing replenishing/depleting processes during binary molecular collisions. Replenishing collisions result in a molecule with a post-collision velocity belonging to the specified class. In depleting collisions, molecules with pre-collision velocities belonging to the specified class are removed after collision. The collision operator thus represents the total rate of increase of molecules to the specified velocity class through collisions, given by the integration over all scattering angles and all possible velocities of the collision partner.

When the total number of depleting collisions of molecules in a velocity class balances the total number of replenishing collisions, the flow is said to be in *equilibrium*. The velocity distribution function in this special case is the equilibrium Maxwellian distribution function

$$f^{(0)} = \left(\frac{m}{2\pi k_b T} \right)^{3/2} \exp^{-m\mathbf{C}^2/2k_b T} . \quad (2.2)$$

When the pressure tensor and heat flux vector are computed assuming this distribution, the pressure tensor reduces to the thermodynamic pressure and the heat flux vector is zero. Substitution of these results into the mass, momentum and energy conservation equations yields the inviscid Euler equations. [12, 21]

2.2.2 Chapman-Enskog Theory and the Navier-Stokes Equations

Under conditions of weak non-equilibrium, the velocity distribution describing the thermal velocities of molecules within the flow exhibits a small departure from the equilibrium (Maxwellian) distribution. In this case, the solution to the Boltzmann equation may be obtained using the Chapman-Enskog perturbation method. In the Chapman-Enskog approach, the distribution function f is expanded as a power series in a small parameter ϵ , which is a measure of the degree of nonequilibrium of the gas flow. To first order, the perturbed distribution function is expressed as

$$f^{(1)} = f^{(0)} (1 + \phi^{(1)}) , \quad (2.3)$$

where $\phi^{(1)}$ is the perturbation of the equilibrium distribution to first order. Using the method of Chapman and Enskog, substitution of this distribution into the Boltzmann equation results in a general form for the perturbation,

$$\phi^{(1)} = -\frac{1}{n}A(C)\mathbf{C} \cdot \nabla \log T - \frac{1}{n}B(C) (\mathbf{C}\mathbf{C} - 1/3C^2\mathbf{I}) : \nabla v. \quad (2.4)$$

Using this expression for the perturbation, the perturbed distribution in (2.3) may be used to compute the first-order corrections to the pressure tensor and heat flux vector. To first order, the pressure tensor correction is given as

$$\mathbf{p}^{(1)} = \int m\mathbf{C}\mathbf{C}f^{(1)}d^3C = -\frac{1}{5}k_bT [\mathbf{B}, \mathbf{B}] \mathbf{S}. \quad (2.5)$$

In the evaluation of the integrand, the term in the perturbation involving $A(C)$ is odd in \mathbf{C} and drops out, and so the pressure tensor is expressed in terms of

the bracket integral $[\mathbf{B}, \mathbf{B}]$ and the rate of shear tensor \mathbf{S} , which is given as

$$\mathbf{S} = \frac{1}{2} (\partial_j v_i + \partial_i v_j) - \frac{1}{3} \partial_k v_k \delta_{ij}. \quad (2.6)$$

At this point, the kinetic definition of the coefficient of viscosity is introduced, which is expressed in terms of the bracket integral of the tensor $\mathbf{B} = B(C) (\mathbf{C}\mathbf{C} - 1/3 C^2 \mathbf{I})$,

$$\mu = \frac{1}{10} k_b T [\mathbf{B}, \mathbf{B}]. \quad (2.7)$$

Thus, combining the equilibrium result for thermodynamic pressure and the first order correction from (2.5), the pressure tensor to first order in the Chapman-Enskog approximation is

$$\mathbf{p} = p \mathbf{I} - 2\mu \mathbf{S}. \quad (2.8)$$

Similarly, the correction to the heat flux vector is given as

$$\mathbf{q}^{(1)} = \int \frac{1}{2} m C^2 \mathbf{C} f^{(1)} d^3 C = -\frac{1}{3} k_b T [\mathbf{A}, \mathbf{A}] \nabla \log T. \quad (2.9)$$

In this case, the term in the perturbation involving $B(C)$ drops out, as the integrand in (2.9) is odd in this term. The heat flux vector is expressed in terms of the bracket integral $[\mathbf{A}, \mathbf{A}]$ of the vector $\mathbf{A} = A(C) \mathbf{C}$, and the kinetic definition of the coefficient of translational thermal conductivity is introduced

$$K_{tr} = \frac{1}{3} k_b [\mathbf{A}, \mathbf{A}]. \quad (2.10)$$

The heat flux vector to first order in the Chapman-Enskog approximation is thus

$$\mathbf{q} = -K_{tr} \nabla T, \quad (2.11)$$

as there is no contribution from the (zero-order) equilibrium result.

Substitution of the Chapman-Enskog results from (2.8) and (2.11) into the mass, momentum and energy conservation equations (absent body forces) results in the Navier-Stokes equations

$$\frac{1}{\rho} \frac{d\rho}{dt} = -\nabla \cdot \mathbf{v} \quad (2.12)$$

$$\rho \frac{d\mathbf{v}}{dt} = -\nabla p + 2\mu \nabla \cdot \mathbf{S} \quad (2.13)$$

$$\rho \frac{dT}{dt} = -\frac{2m}{3k_b} (-\nabla \cdot K_{tr} \nabla T + p \nabla \cdot \mathbf{v} - n\mu \mathbf{S} : \nabla \mathbf{v}) \quad (2.14)$$

The current discussion has been limited to single species gases with no internal structure; however, as discussed in the next section, the Navier-Stokes equations are easily extended to enable the modeling of gas mixtures with internal degrees of freedom, which is the focus of this hybrid work.

At this point, the Navier-Stokes equations in (2.12)-(2.14), as well as the first-order Chapman-Enskog perturbation in (2.4), are expressed in terms of the unknown quantities \mathbf{A} and \mathbf{B} . The next task is to introduce the solution of the bracket integrals $[\mathbf{A}, \mathbf{A}]$ and $[\mathbf{B}, \mathbf{B}]$ found in the expressions for the transport coefficients μ and K_{tr} . This is an important step that provides closure of the Navier-Stokes equations and allows for a more convenient representation of the perturbation $\phi^{(1)}$. Moreover, this step introduces the *collision integrals* which serve as an important connection between the two numerical methods used in this hybrid work.

2.2.3 Collision Integrals and Transport Coefficients

The solution of the bracket integrals requires knowledge of the molecular interaction potentials, and with the exception of the Maxwellian molecule, an exact solution is not possible. Therefore, an approximate solution method is used which involves an expansion of the *trial functions* \mathbf{a} and \mathbf{b} (corresponding to the solution of $[\mathbf{A}, \mathbf{A}]$ and $[\mathbf{B}, \mathbf{B}]$, respectively) in finite linear combinations of the Sonine polynomials. A brief outline is presented here to provide continuity in the discussion of the later chapters and appendices, but the details of this formulation are discussed in Chapman & Cowling and Ferziger & Kaper [12, 21].

Recalling the expression (2.7) for the coefficient of viscosity, the trial function \mathbf{b} is expanded in the Sonine polynomials

$$S_v^{(n)}(x) = \sum_{p=0}^n \frac{\Gamma(v+n+1)}{(n-p)!p!\Gamma(v+p)}(-x)^p = \begin{cases} 1 & \text{if } n = 0 \\ v+1-x & \text{if } n = 1 \end{cases} \quad (2.15)$$

such that

$$\mathbf{b} = \sum_{p=0}^{n-1} b_p^n S_{5/2}^{(p)}(\mathcal{C}^2) \left(\mathcal{C}\mathcal{C} - \frac{1}{3}\mathcal{C}^2\mathbf{I} \right). \quad (2.16)$$

It can be shown that the bracket integral $[\mathbf{B}, \mathbf{B}]$ can be expressed in terms of the coefficients b_p^n such that

$$[\mu]_n = \frac{1}{10}k_bT [\mathbf{B}, \mathbf{B}] = \frac{1}{2}k_bT b_0^n \quad (2.17)$$

where the coefficients b_0^n are determined from the equations

$$\sum_{q=0}^{n-1} H^{pq} b_q^n = \frac{2}{kT} \delta_{p0} \quad p = 0, \dots, n-1. \quad (2.18)$$

The coefficient H^{pq} in (2.18) is defined in terms of the bracket integral (following from (2.16))

$$H^{pq} = \frac{2}{5k_b T} \left[S_{5/2}^{(q)}(\mathcal{C}^2)(\mathcal{C}\mathcal{C} - \frac{1}{3}\mathcal{C}^2\mathbf{I}), S_{5/2}^{(q)}(\mathcal{C}^2)(\mathcal{C}\mathcal{C} - \frac{1}{3}\mathcal{C}^2\mathbf{I}) \right]. \quad (2.19)$$

Bracket integrals of the Sonine polynomials similar to the form shown in (2.19) appear frequently in transport property calculations, and are often expressed in a more compact form involving the Ω -integrals (or *collision integrals*) defined as

$$\Omega^{(l)}(r) = 2\pi \left(\frac{k_b T}{2m} \right)^{1/2} \int_0^\infty \int_0^\infty e^{-\mathbf{g}^2} \mathbf{g}^{2r+3} \{1 - \cos^l \chi\} b \, db \, d\mathbf{g}. \quad (2.20)$$

Many bracket integrals have been evaluated in terms of the corresponding collision integrals and are available in tabulated form for calculation of the transport coefficients [21, 38]. The first order ($n = 1$) approximation to the coefficient of viscosity $[\mu]_1$ may now be evaluated in terms of the collision integrals. The coefficient b_0^1 must first be determined from (2.18), for $p, q = 0$, such that

$$b_0^1 = \frac{2}{k_b T H^{00}}, \quad (2.21)$$

and the coefficient H^{00} reduces to

$$H^{00} = \frac{8}{5k_b T} \Omega^{(2)}(2). \quad (2.22)$$

Finally, the coefficient of viscosity is

$$[\mu]_1 = \frac{5k_b T}{8\Omega^{(2)}(2)}. \quad (2.23)$$

Following the same procedure for the coefficient of thermal conductivity (2.10), the trial function \mathbf{a} is expanded in the Sonine polynomials such that

$$\mathbf{a} = - \left(\frac{m}{2k_b T} \right)^{1/2} \sum_{p=1}^n a_p^n S_{3/2}^{(p)}(\mathcal{C}^2) \mathcal{C}. \quad (2.24)$$

The coefficient of thermal conductivity can then be expressed in terms of the coefficients a_p^n such that

$$[K_{tr}]_n = \frac{1}{3} k_b [\mathbf{A}, \mathbf{A}] = \frac{5}{4} k_b a_1^n, \quad (2.25)$$

where the coefficients a_1^n are determined from the equations

$$\sum_{q=1}^n \Lambda^{pq} a_q^n = \frac{4}{5k} \delta_{p1} \quad p = 1, \dots, n. \quad (2.26)$$

Similar to (2.19), the coefficient Λ^{pq} is defined as the bracket integral

$$\Lambda^{pq} = \frac{8m}{75k_b^2 T} \left[S_{3/2}^{(q)}(\mathcal{C}^2) \mathcal{C}, S_{3/2}^{(p)}(\mathcal{C}^2) \mathcal{C} \right]. \quad (2.27)$$

For the first order approximation of the thermal conductivity, the coefficient Λ^{11} reduces to

$$\Lambda^{11} = \frac{16}{25c_v k_b T} \Omega^{(2)}(2), \quad (2.28)$$

and the coefficient of thermal conductivity to first order in the Sonine polynomials is

$$K_{tr} = \frac{25c_v k_b T}{16\Omega^{(2)}(2)}. \quad (2.29)$$

The collision integrals $\Omega^{(l)}(r)$ appearing in the expressions for the transport coefficients are an important quantity in the hybrid framework, as they

provide a connection between the macroscopic transport fluxes and the microscopic details of binary collisions. Within the expression (2.20), the portion

$$\Phi^{(l)} = 2\pi \int_0^\infty (1 - \cos^l \chi) b \, db \quad (2.30)$$

represents the total interaction cross-section. The collision integrals thus represent an (orientational and thermal) average collision probability between two molecules. Therefore, given a representation of the total interaction cross-section or the molecular interaction potential, the collision integrals and Chapman-Enskog Theory may be used to determine the transport coefficients and transport fluxes of a gas system. This step provides closure to the Navier-Stokes equations, as the transport fluxes in (2.12)-(2.14) are now completely specified. Moreover, given any representation of the collision integral (e.g., collision cross-section model, interaction potential, molecular beam scattering data, etc.), the results from Chapman-Enskog Theory allow for the complete description of the transport properties in a gas system. As will be discussed later in Sections 2.3 and 2.4 and Chapter 4, this is an important attribute within the DSMC/CFD framework. The transport of mass, momentum and energy is achieved in different ways within each solver, and so the ability to quantify and calibrate the transport model parameters is a necessary step for a consistent treatment of transport properties within a hybrid solution.

The Chapman-Enskog Theory also provides a connection between the macroscopic transport fluxes (determined from the solution of the Navier-Stokes equations), and the non-equilibrium distribution describing the molecular thermal velocities at the hybrid interface. This connection is established

through the perturbation (2.4). Recalling the perturbed (non-equilibrium) distribution function given in (2.3), the perturbation was expressed in general form in terms of the vector $\mathbf{A} = A(C)\mathbf{C}$ and the tensor $\mathbf{B} = B(C)(\mathbf{C}\mathbf{C} - 1/3C^2\mathbf{I})$. Using the results from the trial functions \mathbf{a} (2.24) and \mathbf{b} (2.16), the functions \mathbf{A} and \mathbf{B} may be determined to first order in Sonine polynomials as

$$\mathbf{A} = - \left(\frac{m}{2k_b T} \right)^{1/2} \frac{4K_{tr}}{5k_b} \left(\frac{5}{2} - \mathcal{C}^2 \right) \mathcal{C}, \quad (2.31)$$

$$\mathbf{B} = - \frac{2\mu}{k_b T} \left(\mathcal{C}\mathcal{C} - \frac{1}{3}\mathcal{C}^2\mathbb{I} \right). \quad (2.32)$$

After substitution of these expressions into (2.4) and some simple algebra, the perturbation may be expressed in terms of the transport flux quantities obtained from the solution of the Navier-Stokes equations

$$\begin{aligned} \phi^{(1)} = & (q_x \mathcal{C}_x + q_y \mathcal{C}_y + q_z \mathcal{C}_z) \left(\frac{2}{5} \mathcal{C}^2 - 1 \right) \\ & - 2 (\tau_{xy} \mathcal{C}_x \mathcal{C}_y + \tau_{xz} \mathcal{C}_x \mathcal{C}_z + \tau_{yz} \mathcal{C}_y \mathcal{C}_z) \\ & - (\tau_{xx} \mathcal{C}_x^2 + \tau_{yy} \mathcal{C}_y^2 + \tau_{zz} \mathcal{C}_z^2). \end{aligned} \quad (2.33)$$

This result allows for the generation of the DSMC particles from the proper non-equilibrium distribution as determined from Chapman-Enskog Theory (2.3), and particles are generated by sampling this distribution prescribed at the hybrid interface. The hybrid interface is the computational boundary between the CFD and DSMC computational domains, and this interface enables the passing of flux information between the two individual solutions. The details of the hybrid interface mechanics are discussed at the end of Chapter 3.

At this point, it is convenient to evaluate the roadmap of the hybrid framework discussed in this chapter. The formulation of the Navier-Stokes equations from Chapman-Enskog Theory has been outlined for a simple gas, and the transport fluxes (expressed in terms of the collision integrals) were presented, providing closure for the Navier-Stokes equations. The Chapman-Enskog framework also provides a consistent approach for hybrid DSMC particle generation, which will be explored in detail for gas mixtures with internal energy in Chapter 3. The collision integrals are an important component of the hybrid framework and will be revisited throughout this work. Their utility in achieving consistency in the transport coefficients will be examined in Chapter 4. The material introduced in this section was meant to provide a simplified overview of the kinetic theory and general concepts employed for construction of the hybrid approach. The next sections shift focus toward the details of the CFD and DSMC solvers used in this work, with emphasis on the physical models and their range of applicability. An overview of existing hybrid approaches is provided in the following section.

2.3 CFD Method

Computational fluid dynamics (CFD) methods have been widely developed as a means for providing accurate and efficient solutions to the Navier-Stokes equations. As mentioned in the previous section, the Navier-Stokes equations achieve closure through the Chapman-Enskog approximation of the transport fluxes. Thus, the application of CFD methods are limited to con-

tinuum, near-equilibrium flows. In this section, a more complex five-species air system is considered, and the physical models employed within the DPLR solver for the flowfield solutions considered in this work are presented and discussed.

2.3.1 DPLR solver for continuum flows

The continuum flowfield solutions used in this hybrid work are generated using the DPLR solver [88]. The DPLR software suite was developed at NASA Ames Research Center as a tool for modeling the aerothermodynamic environments of many (re-)entry vehicles for Earth and Mars applications. DPLR is a parallel, structured, finite-volume code for the solution of the Navier-Stokes equations. The flow in the computational domain is initialized to the specified freestream conditions, and the solution is marched forward in time using implicit DPLR time integration, until steady state is reached. Time accurate (unsteady) calculations are not considered in this work. A third-order upwind biased MUSCL Steger-Warming scheme with a minmod flux limiter is used for the extrapolation of the Euler fluxes in the streamwise, wall-normal and spanwise directions. The eigenvalue limiters were chosen to minimize additional dissipation within the boundary layer.

The gas flows considered in this work are restricted to a frozen, non-ionized five species air (N_2 , O_2 , NO , N , O) mixture. A multi-temperature model is used whereby the energy in the translational, rotational and vibrational modes are characterized by separate temperatures T_{tr} , T_{rot} and T_{vib} , respec-

tively. This requires a solution of five species equations, three momentum equations and three energy equations. The primary flowfields generated in this work are two-dimensional compressible boundary layer flows over a discrete, three-dimensional surface roughness geometry. Several gas-surface interaction models are available within DPLR, but this work is limited to the study of non-reacting slip- and no-slip surface models. The no-slip condition assumes that the flow velocities at the stationary wall are equal to zero, and the flow temperatures (T_{tr}, T_{rot}, T_{vib}) at the wall are specified by the temperature of the surface. The slip model employed in this work is the Gökçen slip model [29], which is similar to a Maxwellian slip condition at the wall, but includes a modified accommodation coefficient to improve results for high Knudsen number flows. Maxwell's slip model specifies a slip velocity, u_s , at the wall that is proportional to the wall-normal gradient ($\partial/\partial y$) of the flow velocity, u , tangential to the wall,

$$u_s = A \left(\frac{2 - \sigma_u}{\sigma_u} \right) \lambda_u \left. \frac{\partial u}{\partial y} \right|_{y=0}. \quad (2.34)$$

In this model, A is a constant and σ_u is the momentum accommodation coefficient, which varies according to the surface material. The mean free path λ_u characterizes momentum transport and is defined as [29]

$$\lambda_u = \frac{2\mu}{\rho \bar{c}} \quad (2.35)$$

A slip temperature (or temperature jump) may also be specified according to

$$T_s = \left(\frac{2 - \sigma_T}{\sigma_T} \right) \lambda_T \left. \frac{\partial T}{\partial y} \right|_{y=0} \quad (2.36)$$

where σ_T is the thermal accommodation coefficient and λ_T is the thermal mean free path. The mean free path λ_T characterizes energy transport and is defined as [29]

$$\lambda_T = \frac{2K_{tr}}{\rho \bar{c} c_v} \quad (2.37)$$

In place of the accommodation coefficients in (2.34) and (2.36), Gökçen's slip model uses the modified accommodation coefficient

$$\sigma_{u,T} = 2\lambda_{u,T} \left. \frac{\partial(u, T)}{\partial y} \right|_{y=0}. \quad (2.38)$$

2.3.2 Transport Models

The transport of mass, momentum and energy within a five species air gas mixture is characterized by the species mass and thermal diffusions, viscosity and bulk viscosity, and thermal conductivity with contributions from the translational and internal modes. In this work, the mass diffusion, viscosity and translational and internal thermal conductivities are considered. The coefficients of thermal diffusion and bulk viscosity are not modeled in DPLR, and they are likely negligible for the flows examined here, although future work in this area should investigate these effects.

As discussed in the first part of this chapter, rigorous kinetic theory derivations of the transport coefficients may be obtained from the Chapman-Enskog procedure. The solution method has been extended to gas mixtures, species with internal energy, as well as ionized gas mixtures [12, 38, 51, 89]. The calculation of the transport coefficients requires two steps. First, the collision

integrals $\Omega_{st}^l(r)$ must be obtained for each species pair, s, t . The Chapman-Enskog formulas may then be evaluated for the $[\mathbb{S} \times \mathbb{S}]$ system. In the past, the evaluation of the full $[\mathbb{S} \times \mathbb{S}]$ system was generally quite expensive, and so mixing rules were often used in CFD solvers as an approximation to the Chapman-Enskog solution. However, iterative methods have been demonstrated as an efficient approach for solution of the full Chapman-Enskog matrix [20]. Comparisons among the available mixing rules and the Chapman-Enskog results which characterize their accuracy and efficiency are available in the literature [51, 52, 60].

The species diffusion coefficients are computed in DPLR using the self-consistent effective binary diffusion (SCEBD) model [66]. The SCEBD model is a simplification of the Stefan-Maxwell equations, which use the full set of multi-component diffusion coefficients to compute the species mass fluxes for a multicomponent gas mixture. Instead of computing the full multi-component species diffusion coefficient matrix that is obtained from Chapman-Enskog Theory, this model uses a diagonal matrix of effective diffusion coefficients. The resulting mass flux represents the diffusion of species s through a composite pseudo-species comprising the remaining constituents in the mixture. This model will also be used to approximate the diffusion coefficients obtained through the DSMC collision cross section models; a detailed formulation of the SCEBD model is presented in Chapter 4.

The mixture viscosity and translational thermal conductivity coefficients in DPLR are computed from the model by Gupta *et al.* with Yos

mixing rules [34]. Again, this model is an approximation to the full set of coefficients computed from Chapman-Enskog Theory. The mixture viscosity in DPLR is computed according to Eq. 41 of [34]

$$[\mu]_1 = \sum_{i=1}^{\mathbb{S}} \left(\frac{\chi_i (M_i / N_A)}{\sum_{j=1}^{\mathbb{S}} \chi_j \Delta_{ij}(2)} \right), \quad (2.39)$$

and the mixture translational thermal conductivity is computed according to Eq. 42(a) of [34]

$$[K_{tr}]_1 = \frac{15}{4} \sum_{i=1}^{\mathbb{S}} \left(\frac{\chi_i}{\sum_{j=1}^{\mathbb{S}} \alpha_{ij} \chi_j \Delta_{ij}(2)} \right). \quad (2.40)$$

In these expressions, α_{ij} is defined as

$$\alpha_{ij} = 1 + \frac{(1 - M_i/M_j)(0.45 - 2.54M_i/M_j)}{(1 + (M_i/M_j))^2}, \quad (2.41)$$

where M is the molar mass and N_A is Avogadro's number, and Δ_{ij} is given by

$$\Delta_{ij}(2) = \frac{16}{5} \left[\frac{2M_i M_j}{\pi N_A k_b T (M_i + M_j)} \right]^{1/2} \pi \bar{\Omega}_{ij}^2(2), \quad (2.42)$$

where $\bar{\Omega}_{ij}^l(r)$ are the reduced collision integrals defined as the ‘standard’ collision integral (introduced in (2.20)) normalized by the collision integral for the rigid hard sphere cross section.

The internal thermal conductivities of the molecular components within the air mixture are computed in DPLR using Eucken's approximation. The same assumption is used for the calculation of the DSMC internal thermal conductivities from the collision cross section models. Briefly, the Eucken approximation may be obtained from Generalized Chapman Enskog Theory by

assuming an elastic cross section for the transport of internal energy [57]. This results in a transport of the internal energy throughout the system according to the diffusion of that species. The details concerning the calculation of the internal thermal conductivities from Eucken’s approximation is presented in Chapter 4.

2.3.3 Internal Energy Exchange and Relaxation

As mentioned previously, the DPLR simulations presented in this work allow for thermal non-equilibrium, with a separate energy equation for translational, rotational and vibrational energy. The time rate of change of energy per unit volume has contributions from the convection and conduction of energy through the system, as well as vibrational-translational and rotational-translational energy exchange (recall that the flow is frozen and chemical reactions are neglected). The rate of vibrational relaxation is specified by the vibrational-translational relaxation time, τ_v , which is determined from the correlation by Millikan and White [56],

$$p\tau_{v,MW} = \exp \left[A(T_{tr}^{-1/3} - B) - 18.42 \right] \quad [atm - s] \quad (2.43)$$

A high temperature correction by Park is also employed within DPLR, which is necessary to limit the excitation rates at high temperatures due to the cutoff of elastic cross sections. This correction is given as

$$\tau_c = \left(n\sigma_v \sqrt{8k_b T_{tr} / \pi m} \right)^{-1}, \quad (2.44)$$

and the total vibrational relaxation time is then

$$\tau_v = \tau_{v,MW} + \tau_c. \quad (2.45)$$

The rotational-translational relaxation of the gas is modeled using the expression for a rotational relaxation time from Parker [63],

$$\tau_r = \frac{Z_r^\infty \tau}{\left[1 + \frac{\pi^{3/2}}{2} \left(\frac{T^*}{T_{tr}} \right)^{1/2} + \left(\frac{\pi^2}{4} + \pi \right) \left(\frac{T^*}{T_{tr}} \right) \right]}, \quad (2.46)$$

where τ is the average time between collisions and the values T^* and Z_r^∞ are tabulated constants.

2.4 The Direct Simulation Monte Carlo Method

The direct simulation Monte Carlo (DSMC) method is used in this work to model regions of non-equilibrium flow. In this section, a brief overview of the DSMC method is provided, and the details of the DAC flow solver as well as the physical models employed within DAC are discussed.

The DSMC method is a particle-based, probabilistic approach for the solution of the Boltzmann equation [2]. The gas flow is modeled with a large number of simulated particles of which the mass, velocity, position and internal energy state are tracked throughout the simulation. Each simulated particle represents a prescribed number of real molecules in the gas, thus the DSMC solution is subject to statistical noise that is larger than the thermal fluctuations within a real gas. The particles move throughout the computational domain and undergo collisions with other particles or with surfaces, and

the macroscopic flow information is computed from the particle information sampled within each computational cell.

There are two primary steps involved in a DSMC simulation. Particles are first ‘created’ (that is to say, they are generated either at computational boundaries or within a computational cell) and moved throughout the computational domain according to their prescribed velocity for a single time step. Following the dilute gas assumption and neglecting any external body forces or collisions with surfaces, this motion is a straight trajectory. In the second step, these particles are then sorted into computational cells, and pairs of particles within each cell are randomly selected to undergo collisions. In the case of an elastic collision, the post-collision scattering direction along with the conservation of momentum and energy determine the post-collision velocities of the colliding pair. In the case of an inelastic collision, the total energy of the colliding particles is redistributed according to the Larsen-Borgnakke model (discussed in Section 2.4.3). These two steps are repeated until the flow reaches a steady state.

2.4.1 DAC solver for rarefied flows

The hybrid DSMC solutions presented in this work are generated using a *modified* version of the DSMC Analysis Code (DAC) rarefied flow solver [48]. DAC was developed at NASA JSC as a simulation tool for general rarefied gas flows. The solver comprises a main driver program for the actual DSMC calculation, and includes several pre- and post-processing modules and libraries

as well as a surface geometry preprocessor. DAC includes both serial and parallel versions of the pre-processor and driver programs, and can be used to solve axi-symmetric and two- and three-dimensional flow problems.

Prior to the DSMC simulation in DAC, a ‘water-tight’ geometry must be constructed using a grid generation program. The water-tight geometry is then imported into DAC, which can set up a variety of external or internal flow problems, e.g. flow around a sphere or expanding nozzle flows. In this work, the flow problem within DAC is set up as an internal flow, in which the water-tight geometry is a rectangular box. The details of the flow boundary conditions and roughness geometry are discussed later in Chapters 3 and 5, while an overview of the geometry setup and DAC-specific mechanics are outlined here. Five sides (front, back, left, right and top) are designated as inflow boundaries, and the sixth side (bottom) is specified as a solid wall, comprising the flat surface and the discrete surface roughness. The six faces of the water-tight geometry are created as triangulated surfaces, and each surface is constructed such that all surface normals are pointing *into* the box, where the DSMC flowfield is created.

Prior to creating the computational volume cells within this water-tight geometry, the inflow pointwise boundary conditions must first be specified at each node on the triangulated surface through the STP geometry preprocessor in DAC. The macroscopic flow quantities specified at these nodes are later used for DSMC particle generation, which occurs on the ‘fluxing triangles’ referred to later in Chapter 3. The surface triangles in DAC are defined according to

a continuous connectivity list and node positions based on the global (x, y, z) coordinate system of the computational domain, but a local coordinate system, defined by the two sides of the triangle and the surface normal, is used for particle generation on each surface triangle. This allows for very complex geometries to be handled easily and consistently in DAC. However, this requires that all of the macroscopic flow quantities in vector form (velocity, diffusion fluxes and heat fluxes) and tensor form (shear stresses) necessary for non-equilibrium DSMC particle generation (Chapter 3) must first be projected onto the local coordinate system of each fluxing surface triangle. This transformation is accomplished later on within DAC using the three-dimensional rotation matrix. This is not necessary for quantities that are rotationally invariant (e.g., number density, temperature).

After the solid surface and inflow boundary conditions have been specified in STP, the surface discretization file is loaded into the flow preprocessor DPREDAC (parallel version). The flow preprocessor builds a structured computational domain (comprising coarse Level-I and finer resolution Level-II computational volume cells [47]) that contains the *entire* water-tight geometry. The triangulated surfaces of the water-tight geometry obviously cut through a portion of the computational cells. To handle these, the preprocessor computes the intersection of the surface triangles and computational cells and determines the volume of the cut cell that lies *inside* the flowfield. This portion of the cut cell is tagged as flowfield, while the other portion is tagged as non-flowfield and is not used in the DAC simulation. Cells lying entirely inside or outside

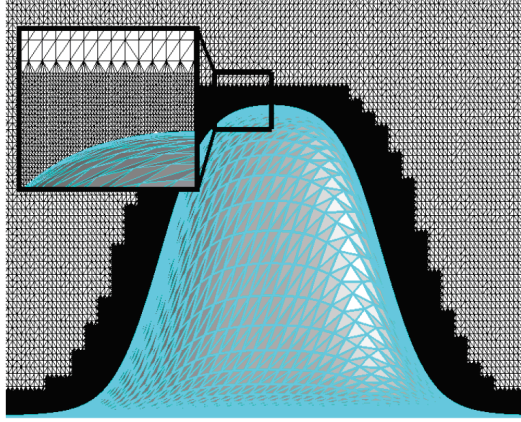


Figure 2.1: DAC computational domain with Level-I and Level-II cells and triangulated surface geometry (shown in gray with blue unstructured surface mesh). The Level-II cells enhance the resolution of the computational grid near the geometry surface.

of the flowfield region are also tagged appropriately. The preprocessor also discerns near-body cells (cells near the triangulated surface), which after some modification to DPREDAC, is exploited later in Chapter 5 to improve the predicted total surface heating within the DSMC solution. An example of the final computational domain, including the Level-I and Level-II flowfield cells, is shown in Figure 2.1

Once the computational domain is completely specified, the flowfield files are loaded into the main DAC solver. The computational domain is initialized as a vacuum, and DSMC particles flux into the computational domain from the surface triangles that were specified as inflow boundaries in STP. The simulation is continued until the average number of particles fluxing into the domain balances that of particles fluxing out of the domain, and the surface

heating has reached a steady state. The details of the DAC simulations and convergence requirements for the cases examined in this work are described in Chapter 5.

2.4.2 Collision cross section models

The transport properties within the DSMC method are a result of the transfer of mass, momentum and energy through particle movement and collision dynamics. The DSMC collision cross section models examined in this work include the variable hard sphere (VHS) and variable soft sphere (VSS) models. Within this framework, the DSMC simulation particles are modeled as hard spheres of diameter d which is a function of g , the relative speed of the collision pair, such that $d \sim (1/g)^{\omega-1/2}$. The VSS model also includes a scattering angle specified by the coefficient α , such that values of $\alpha > 1.0$ result in a scattering angle smaller than the corresponding value of the VHS model (in which $\alpha = 1.0$). The reduced scattering angle effectively establishes a forward-scattering tendency of the colliding particles. This feature in VSS provides a model in which both the diffusion and viscosity cross sections are consistent with those from any intermolecular potential [43]. The VHS and VSS models are discussed in detail later in Chapter 4, where a thorough analysis is presented regarding the calibration of the collision model parameters. This calibration is conducted in order to achieve a consistent set of transport properties within the hybrid DSMC/CFD framework.

For the chemically frozen five-species air hybrid simulations presented

in this work, the variable hard sphere (VHS) model is considered, since as will be found later, the diffusion fluxes in the flows considered here are negligible. Use of the VHS model in the same flow conditions for a *reacting* gas mixture would be questionable, however, due to the strong influence of the diffusion heat flux in reacting flows.

2.4.3 Internal Energy Exchange and Relaxation

The Larsen-Borgnakke model [4] is used in DSMC for energy redistribution in inelastic collisions, for both translational/rotational and translational/vibrational exchanges. The internal energy exchange is determined on a collisional basis according to the probability defined as $1/Z$, where Z is the collision number of the internal mode.

The vibrational relaxation times in both DPLR and DAC are determined using the Landau-Teller model for simple harmonic oscillators, along with empirical correlations for the vibrational relaxation time from Millikan and White [56] with Park's high-temperature correction [61]. The rotational collision number used in the present work is assumed to be constant, with $Z_r=5$. To ensure consistency in the vibrational relaxation times achieved in both solvers, the DSMC vibrational collision number is determined according to the expression[27]:

$$Z_v^{DSMC} = Z_v^{NS} \left(\frac{1}{1 + \frac{0.5\xi_v^2 \exp(\theta_v/T)}{(4-2\omega)}} \right) \quad (2.47)$$

where θ_v is the characteristic vibrational temperature and ξ_v is the temperature-dependent number of vibrational degrees of freedom for a harmonic oscillator given by:

$$\xi_v = \left(\frac{2\theta_v/T}{\exp(\theta_v/T) - 1} \right) \quad (2.48)$$

The Navier-Stokes collision number, Z_v^{NS} is computed as:

$$Z_v^{NS} = (\tau_v^{MW} + \tau_v^{Park}) \nu \quad (2.49)$$

and τ_v^{MW} is determined from the empirical correlation:

$$\tau_v^{MW} = \frac{1}{p} \exp(A(T^{-1/3} - B) - 18.42) \quad (2.50)$$

In (2.50), A and B are vibrational constants specified for each collision pair [61], and p is in atmospheres. The collision frequency ν of species s in a mixture is determined by:

$$\nu_s = \sum_t \left(n_t (d_{ref})_t^2 \left(\frac{8\pi k_b T_{ref,t}}{m_t^*} \right)^{1/2} \left(\frac{T}{T_{ref,t}} \right)^{1-\omega_t} \right) \quad (2.51)$$

All quantities in (2.51) are determined according to the DSMC cell-based macroscopic quantities as outlined in Deschenes *et al.* [19]. This vibrational relaxation approach has been demonstrated to provide good agreement between the vibrational relaxation times produced by DSMC and continuum flow solvers in a heat bath of five species air [40].

2.5 Hybrid Approaches for Continuum/Rarefied Flows

Although CFD approaches provide an efficient and accurate solution in near-continuum flow regimes, the underlying continuum assumption inherent

in the solution of the Navier-Stokes equations breaks down in strong non-equilibrium flows. In this regime, high-fidelity kinetics-based methods, such as direct simulation Monte Carlo (DSMC)[2], must be used to accurately capture non-equilibrium effects that drive important thermo-chemical processes. While the DSMC solution is valid from free-molecular to continuum regimes, the time step and cell size requirements become computationally prohibitive in the continuum limit. It is precisely in this regime, however, that a CFD solver may be employed. Thus, a combined DSMC/CFD hybrid approach is often adopted as a way to achieve high-fidelity solutions while maintaining computational efficiency.

Hybrid methods have been developed and successfully applied for a variety of flow scenarios[18, 36, 65, 69, 71–74]. The hybrid flowfield solution is generally obtained by first determining the location of the hybrid interface, which forms the boundary between the CFD and DSMC solvers, at or near the breakdown of the Navier-Stokes solution. Since the breakdown location can not be determined *a priori*, an initial CFD solution is generally used to determine the interface location based on a breakdown criterion. This criterion may be either parameter-based, or based on a direct comparison of flow quantities or distributions[6, 9, 13, 22, 73]. The interface is then used to pass flowfield information between the two solvers. Macroscopic flowfield quantities from the CFD solution are used to prescribe the appropriate distribution function from which DSMC particle thermal velocities and internal energies are sampled. These particles may be created and fluxed into the non-equilibrium

computational domain using either volume reservoir or surface reservoir approaches. The DSMC solver is then used to generate the local non-equilibrium flow solution.

The generation of hybrid solutions that involve the coupling of DSMC and CFD solutions requires a careful and consistent formulation of a proper boundary condition for the transfer of flux information across the hybrid interface. In equilibrium conditions (i.e., $\mathbb{D}_i = \tau_{ij} = q_i = 0$, or Euler solution), DSMC particle information may be sampled from an equilibrium Maxwell-Boltzmann distribution. Under non-equilibrium conditions, however, (i.e., $\mathbb{D}_i, \tau_{ij}, q_i \neq 0$, or Navier-Stokes solution) DSMC particle information must be sampled from the Chapman-Enskog distribution, to ensure the preservation of flux information across the hybrid interface. Garcia and Alder presented an acceptance-rejection algorithm for generating particle velocities from a Chapman-Enskog distribution within a volume reservoir [23]. This formulation, however, is limited to simple (single-species, monatomic) gas flows, and includes only the shear stress tensor and translational heat flux vector components in the expression for the perturbation. In efforts to extend these hybrid methods to more complex flows often encountered in hypersonic applications, this work presents an extension of the Chapman-Enskog boundary condition to include gas mixtures and gases with internal energy. This new boundary condition is formulated in the framework of Generalized Chapman-Enskog Theory[7, 44, 57], and includes contributions from Navier-Stokes fluxes arising from species diffusion, viscosity, and translational and internal thermal

conductivity.

An additional consideration that is necessary for a quality hybrid solution is the consistent treatment of the thermo-chemical models employed by each of the solvers. For simulations of hypersonic flows, this includes models for thermal relaxation and general thermodynamics, chemical reactions, and mass, momentum and energy transport. Consistency in these models promotes a smooth transition from one computational region to the other by ensuring that the same flow ‘problem’ is being solved in each region. It also allows for a consistent comparison of the CFD and DSMC solutions by ensuring that any differences between the solutions are due to fundamental non-equilibrium processes, rather than differences in the physical models. Previous studies have presented consistent treatments for the thermal relaxation processes[19, 27] and chemical reactions in five-species air systems [41] for use in hybrid applications, or direct DSMC/CFD comparisons. This manuscript examines the transport properties generated by the DSMC and CFD models for a five-species air gas mixture. A general approach for the calibration of the DSMC collision model parameters is presented, in which both the variable hard sphere (VHS) and variable soft sphere (VSS) collision cross section models are examined. The method for prescribing the collision partner parameters (either collision-averaged or collision-specific) is also examined in the fitting of DSMC transport coefficients. The resulting transport coefficients from the calibrated DSMC parameters are compared with the transport coefficient models employed in the CFD solver.

To generate the hybrid solution, the DPLR code is first used to compute the flowfield over the geometry of interest. The hybrid interface is formed in the flow region surrounding the surface roughness, and the macroscopic parameters obtained from the Navier-Stokes solution are used to generate the appropriate velocity distribution function for hybrid particle generation at the interface. The DAC solver is then used to compute the non-equilibrium solution in the region surrounding the roughness. The details involved with obtaining the hybrid solution are presented in the following Chapters.

2.6 Summary

The material presented in this chapter lays the groundwork for the novel hybrid methods (presented in Chapters 3 and 4) that have been developed for these studies, as well as the analysis of the hybrid and CFD flow-field solutions presented in Chapter 5. The construction of a consistent hybrid DSMC/CFD framework relies on the fundamental principles established through (Generalized) Chapman-Enskog Theory. This theory establishes the relationship between the DSMC and CFD methods through the Boltzmann equation. The CFD method, which involves solution of the Navier-Stokes equations, is limited to flows which are near equilibrium, as the Navier-Stokes equations are formulated assuming (*a priori*) that the flow is described by the Chapman-Enskog distribution. The DSMC method is a particle-based, probabilistic approach for the solution of the Boltzmann equation, and makes no underlying assumption of the probability distribution function describing the

flow. The DSMC method can therefore be used to accurately model strong non-equilibrium flows.

The collision-integrals and the expression for the perturbation are two important principles that are established from Chapman-Enskog theory. The perturbation formulated from Generalized Chapman-Enskog Theory (discussed in Chapter 3), provides a link between the non-equilibrium macroscopic fluxes determined from CFD, and the non-equilibrium distribution function describing particle thermal velocities and internal energies in DSMC. This perturbation thus provides a transition from the continuum CFD solution to the non-equilibrium DSMC solution in the hybrid solution. Although the discussion of the perturbation in this chapter was limited to simple gases, the general concepts presented here are easily extended to the five-species air system considered in this work through Generalized Chapman Enskog Theory.

The collision-integrals provide a link between the microscopic collision dynamics and the definition of the transport coefficients, and thus the macroscopic transport fluxes. The importance of the collision-integrals within the hybrid framework is exemplified in Chapter 4, where the consistency in transport properties modeled in DSMC and CFD is discussed in detail. The thermo-chemical models used in the DAC (DSMC) and DPLR (CFD) solvers were presented in this chapter as well, and consistency in vibrational relaxation rates used in both solvers is achieved following the work of Gimelshein *et al.* [27] and Deschenes *et al.* [19], as discussed in this chapter.

Chapter 3

Generation of the Hybrid Solution

3.1 Overview

In this chapter, an approach for the generation of particles at a hybrid Navier-Stokes/DSMC interface is presented for simple gases and gas mixtures with internal degrees of freedom. DSMC particles generated at a hybrid boundary are assigned thermal velocities using a non-equilibrium surface reservoir approach, in which the fluxes of mass, momentum and energy determined from the Navier-Stokes solution are used to prescribe the appropriate velocity distribution function used in the DSMC particle generation. The non-equilibrium surface reservoir approach is first outlined for a simple (single-species, monatomic) gas, and is then extended to gas mixtures with internal degrees of freedom, in which additional diffusion and internal heat flux terms are included in the Generalized Chapman-Enskog formulation of the perturbation. The significance of the diffusion, shear stress and heat flux parameters in the perturbation are examined at a hybrid interface within non-equilibrium boundary layer flow, as well as within the breakdown region near a normal shock, in a five-species air gas mixture. The validity of the Chapman-Enskog perturbation at each of these hybrid interfaces is assessed by comparison with the Generalized Chapman-Enskog perturbations. Finally, the concepts intro-

duced here are applied to a three-dimensional flowfield of hypersonic boundary layer flow over surface roughness.

3.2 Hybrid Particle Generation

The quality of a hybrid solution involving direct simulation Monte Carlo (DSMC) and Navier-Stokes solvers relies on the accurate representation of the flowfield across the hybrid interface. The transfer of information from the Navier-Stokes solution to the DSMC solver is made almost exclusively through the velocity distribution function, which is used to prescribe the thermal velocities of particles generated at the hybrid interface. When the flowfield at the location of the hybrid interface is in equilibrium, the particle thermal velocities may be prescribed from a Maxwellian distribution. In contrast, DSMC particles that are generated at an interface within a non-equilibrium region follow a perturbed velocity distribution which, for small departures from equilibrium, may be described by the Chapman-Enskog distribution function.

3.2.1 Volume and Surface Reservoir Approaches

Particles generated at the hybrid interface may be introduced into the computational domain using either a volume reservoir or surface reservoir approach [24, 71]. The volume reservoir approach populates reservoir or ‘ghost’ cells with randomly distributed simulation particles whose thermal velocities are prescribed according to the appropriate velocity distribution function. These particles are allowed to move within the reservoir cells and into the

computational domain during the initial particle creation. Particles that enter the computational domain are used in the simulation, while any particles remaining in the reservoir cells are deleted.

The surface reservoir is an alternative approach to hybrid particle generation. A surface reservoir may be thought of as a surface which emits randomly distributed particles at a rate that is consistent with the macroscopic properties of the fluid. The surface reservoir approach may be more computationally efficient than the volume reservoir approach, since all particles generated at the hybrid domain boundary are used in the simulation. The velocity distribution function describing the thermal velocities of these particles is formulated by computing the distribution of particles in an infinite reservoir which would cross the surface reservoir boundary and enter into the computational domain during a single timestep.

The current work seeks to extend the surface reservoir approach to particles generated in a non-equilibrium flowfield region. The non-equilibrium surface reservoir distribution function is derived first for a simple gas assumed to follow a Chapman-Enskog distribution (Section 3.3.1), and a general approach for particle sampling from this distribution is outlined at the end of this section and Appendix A. This surface reservoir approach is then extended to a gas mixture with internal degrees of freedom by way of the Generalized Chapman-Enskog framework (Section 3.3.2 and Appendix B), and a general approach for particle sampling from these distributions is provided at the end of Section 3.3.2. In Section 3.4 a simple analysis is presented in which the sig-

nificance of the diffusion flux, shear stress and heat flux contributions to the Generalized Chapman-Enskog perturbation are assessed for a hybrid interface within a non-equilibrium boundary layer flowfield (Section 3.4.1), as well as within the breakdown region near a normal shock (Section 3.4.2).

3.3 Particle generation using a non-equilibrium surface reservoir approach

3.3.1 Surface reservoir approach for a simple gas

The surface reservoir approach employed in this work may be thought of as a fluxing triangulated surface that emits randomly distributed particles into the DSMC computational domain (Figure 3.1). In equilibrium conditions (i.e., $\tau_{ij} = q_i = 0$), the thermal velocity components tangential to the fluxing surface may be generated from a Maxwellian distribution, however the thermal velocity component normal to the fluxing surface is prescribed from a *one-sided* Maxwellian distribution [24, 50] as shown in Figure 3.2. Under non-equilibrium conditions (i.e., $\tau_{ij}, q_i \neq 0$), the Chapman-Enskog distribution should be employed for cases in which the flow exhibits a small departure from equilibrium [23, 36, 71]. Garcia and Alder presented an acceptance-rejection algorithm for generating particle velocities from a Chapman-Enskog distribution within a volume reservoir [23]. To generate particles under non-equilibrium conditions using a surface reservoir approach, we must first derive the appropriate velocity distribution for a non-equilibrium surface reservoir.

Consider a simple gas inside a reservoir extending from $(-\infty < x \leq$

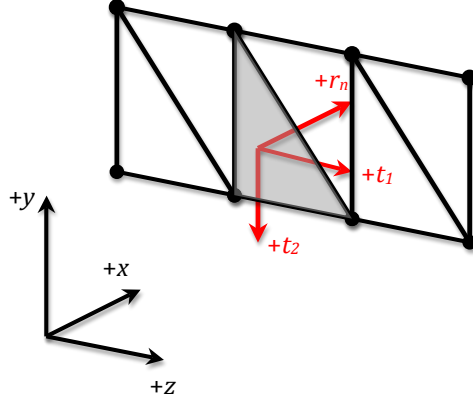


Figure 3.1: Schematic of surface reservoir comprised of fluxing triangles. Particles are randomly distributed over shaded surface and then released into computational domain (in $+x$ -direction).

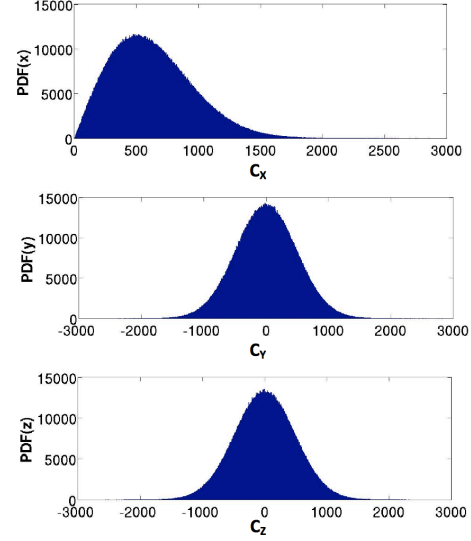


Figure 3.2: Equilibrium surface reservoir velocity distribution functions corresponding to normal (one-sided Maxwellian distribution; top) and tangential (Maxwellian distribution; middle, bottom) velocity components.

0) which follows a Chapman-Enskog distribution. The velocity distribution describing the particle thermal velocities within the reservoir may be expressed as [12, 21, 38]:

$$f^{(1)}(\mathbf{C}) = f^{(0)}(\mathbf{C})\Gamma(\mathbf{C}), \quad (3.1)$$

where $f^{(0)}(\mathbf{C})$ is the equilibrium Maxwellian distribution defined by:

$$f^{(0)}(\mathbf{C}) = \left(\frac{\beta}{\pi^{1/2}}\right)^3 \exp \left[-(\beta^2 C_x^2 + \beta^2 C_y^2 + \beta^2 C_z^2)\right]. \quad (3.2)$$

The quantity $\Gamma(\mathbf{C}) = 1 + \phi_{CE}(\mathbf{C})$ is the perturbation function describing the

small departure from the equilibrium state which may be expressed as:

$$\begin{aligned}\Gamma(\mathbf{C}) = & 1 + (q_x \mathcal{C}_x + q_y \mathcal{C}_y + q_z \mathcal{C}_z) \left(\frac{2}{5} \mathcal{C}^2 - 1 \right) \\ & - 2 (\tau_{xy} \mathcal{C}_x \mathcal{C}_y + \tau_{xz} \mathcal{C}_x \mathcal{C}_z + \tau_{yz} \mathcal{C}_y \mathcal{C}_z) \\ & - (\tau_{xx} \mathcal{C}_x^2 + \tau_{yy} \mathcal{C}_y^2 + \tau_{zz} \mathcal{C}_z^2),\end{aligned}\tag{3.3}$$

where, for compactness, the product of the thermal velocity components and the inverse most probable thermal speed is expressed as $\mathcal{C}_i = C_i \beta$. The variable \mathcal{C}_i is the scaled thermal velocity component in the direction i where $i, j \in (x, y, z)$, $\beta = \sqrt{m/2k_b T_{tr}}$ is the inverse most probable thermal speed, m is the molecular mass, k_b is Boltzmann's constant and T_{tr} is the translational temperature of the gas. In equation (3.3), $\mathcal{C}^2 = \mathcal{C}_x^2 + \mathcal{C}_y^2 + \mathcal{C}_z^2$ is the square of the magnitude of the normalized particle thermal velocity, and τ_{ij} and q_i are the dimensionless shear stress and heat flux components defined as:

$$\tau_{ij} = \frac{\mu}{p} \left(\partial_j v_i + \partial_i v_j - \frac{2}{3} \partial_k v_k \delta_{ij} \right) = \frac{\tau_{ij}^{NS}}{p},\tag{3.4}$$

$$q_i = -\frac{2\beta K_{tr}}{p} \partial_i T_{tr} = \frac{2\beta q_i^{NS}}{p},\tag{3.5}$$

where μ and K_{tr} are the coefficients of viscosity and translational thermal conductivity, respectively, and p is pressure.

We would like to determine the distribution function $f_{SR}^{(1)}(C)$ of the molecules within this reservoir which cross the surface reservoir (SR) boundary at $x = 0$ and enter into the computational domain per unit time and area. This is equivalent to determining the ratio of the differential flux of molecules which cross the surface reservoir boundary to the total flux of molecules that

would enter the computational domain. This ratio may be expressed as:

$$f_{SR}^{(1)}(\mathbf{C})d\mathbf{C} = \frac{n(C_x + u)f^{(1)}(\mathbf{C})dC_zdC_ydC_x}{n \int_{-u}^{\infty} \int_{-\infty}^{\infty} \int_{-\infty}^{\infty} (C_x + u)f^{(1)}(\mathbf{C})dC_zdC_ydC_x}. \quad (3.6)$$

Here, n is the number density, dC_i is the differential thermal velocity component, and we have allowed for a non-zero bulk velocity u in the $+x$ direction. Using (3.1) and (3.2), we may write (3.6) as:

$$f_{SR}^{(1)}(\mathbf{C})d\mathbf{C} = \frac{(C_x + u) \left(\frac{\beta}{\pi^{1/2}} \right)^3 \exp [-(\mathcal{C}_x^2 + \mathcal{C}_y^2 + \mathcal{C}_z^2)] \Gamma(\mathbf{C})d\mathbf{C}}{\int_{-u}^{\infty} \int_{-\infty}^{\infty} \int_{-\infty}^{\infty} (C_x + u) \left(\frac{\beta}{\pi^{1/2}} \right)^3 \exp [-(\mathcal{C}_x^2 + \mathcal{C}_y^2 + \mathcal{C}_z^2)] \Gamma(\mathbf{C})d\mathbf{C}}. \quad (3.7)$$

We seek to express (3.7) as the product of the distribution functions describing the normal and tangential thermal velocities of particles crossing the surface reservoir boundary into the computational domain, and the corresponding perturbation function. After multiplying and dividing through by $(2\sqrt{\pi}\beta)$ and evaluating the triple integral over velocity space, the expression in (3.7) becomes:

$$f_{SR}^{(1)}(\mathbf{C}) = f_{SR}(C_x)f_{SR}(C_y)f_{SR}(C_z)\Gamma(\mathbf{C}). \quad (3.8)$$

The tangential surface reservoir distributions, $f_{SR}(C_y)$, $f_{SR}(C_z)$ of expression (3.8) follow regular Maxwellian distributions:

$$f_{SR}(C_y, C_z) = \left(\frac{\beta}{\pi^{1/2}} \right) \exp (-\beta^2 C_{(y,z)}^2). \quad (3.9)$$

The normal surface reservoir distribution $f_{sR}(C_x)$ of expression (3.8) contains the form of the equilibrium one-sided Maxwellian distribution, but is modified by the integration over the perturbation included in (3.6), and is given as:

$$f_{sR}(C_x) = \frac{2\beta^2(C_x + u) \exp(-\beta^2 C_x^2) / (u\sqrt{\pi}\beta)}{\left\{ 1 + \operatorname{erf}(\beta u) + \frac{1}{u\sqrt{\pi}\beta} \exp(-\beta^2 u^2) - \frac{q_x}{5\sqrt{\pi}} \exp(-\beta^2 u^2) \right.} \quad (3.10)$$

$$\left. - \left[\frac{1}{u\sqrt{\pi}\beta} \exp(-\beta^2 u^2) + \frac{1}{2}[1 + \operatorname{erf}(\beta u)] \right] \tau_{xx} \right.$$

$$- \frac{1}{2} \left[\frac{1}{u\sqrt{\pi}\beta} \exp(-\beta^2 u^2) + [1 + \operatorname{erf}(\beta u)] \right] \tau_{yy}$$

$$\left. - \frac{1}{2} \left[\frac{1}{u\sqrt{\pi}\beta} \exp(-\beta^2 u^2) + [1 + \operatorname{erf}(\beta u)] \right] \tau_{zz} \right\}.$$

To generate particles from this non-equilibrium surface reservoir distribution given in (3.8), we follow an acceptance-rejection algorithm very similar to the approach outlined in Garcia and Alder [23]:

1. Generate the equilibrium thermal velocity components $(\mathcal{C}_x, \mathcal{C}_y, \mathcal{C}_z)$ from the distributions given by (3.9) and (3.10). (sampling details are outlined in Appendix A)
2. Compute the amplitude parameter $A = 1 + 30B$, where B is the breakdown parameter determined by $B = \max(|\tau_{ij}|, |q_i|)$.
3. If $(A\mathcal{R}_u \leq \Gamma(\mathbf{C}))$, accept $(\mathcal{C}_x, \mathcal{C}_y, \mathcal{C}_z)$, otherwise go to (1). (\mathcal{R}_u is a uniformly distributed random number over the interval $[0,1)$)
4. If non-zero bulk velocity components exist in the tangential (y, z) directions, these are simply added to the accepted thermal velocity components from Step (3), yielding $(\mathcal{C}_x, \mathcal{C}_y + \beta v, \mathcal{C}_z + \beta w)$.

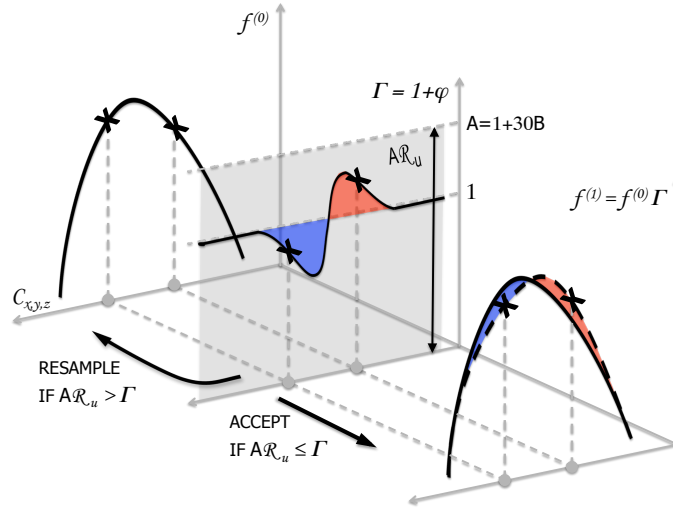


Figure 3.3: Schematic of sampling procedure for a non-equilibrium surface reservoir distribution. Thermal velocities sampled from the equilibrium distribution are rejected more often in the region where $\Gamma < 1$, and are accepted more often in the region where $\Gamma > 1$, resulting in the perturbed distribution, $f^{(1)}$.

Since the non-equilibrium nature of the flowfield modeled using this surface reservoir approach is assumed to be adequately described by the Chapman-Enskog approximation, the distributions should only exhibit a small departure from equilibrium. Thus, to sample this distribution, we use the values of $(\mathcal{C}_x, \mathcal{C}_y, \mathcal{C}_z)$ generated from the surface reservoir distributions $f_{SR}(C_x, C_y, C_z)$ (details in Appendix A) as an ‘educated guess’ to determine the correct non-equilibrium distribution. The thermal velocities determined from Step 1 are finally accepted for use in the simulation after meeting the condition in Step 3. The acceptance criterion in Step 3 can be thought of as a ‘non-equilibrium filter’ on the thermal velocities from Step 1, resulting in the proper non-

equilibrium distribution function (Figure 3). It has been suggested that this approach should be valid for values $B \leq 0.1$, and this breakdown criterion is adopted for this work [23].

The perturbation function for the surface reservoir in (3.3) describes the non-equilibrium state of a simple gas and only accounts for heat flux contributions from gradients in the translational temperature as well as shear stress contributions from gradients in the velocity field. Thus, the macroscopic quantities Q_{SR} required for generating the DSMC particles at the non-equilibrium surface reservoir interface in a simple gas are:

$$Q_{SR} = (n \ p \ T_{tr} \ v_i \ \tau_{ij}^{NS} \ q_i^{NS}). \quad (3.11)$$

3.3.2 Surface reservoir approach for a gas mixture with internal degrees of freedom

The above analysis is now extended to a gas mixture with internal degrees of freedom, to include the additional diffusion flux term arising from the relative motion of species s , as well as the additional heat flux due to internal energy transport in the gas. Consider a gas mixture of S species with internal degrees of freedom inside a reservoir extending from $(-\infty < x \leq 0)$ which is perturbed slightly from the equilibrium Maxwell-Boltzmann distribution. In the Generalized Chapman-Enskog framework, the velocity distribution describing the particle thermal velocities of species s within the reservoir may be expressed as [57]:

$$f_s^{(1)}(\mathbf{C}, \mathcal{E}_{int}) = f_s^{(0)}(\mathbf{C}, \mathcal{E}_{int}) \Gamma_s(\mathbf{C}, \mathcal{E}_{int}), \quad s \in S, \quad (3.12)$$

where $f_s^{(0)}(\mathbf{C}, \mathcal{E}_{int})$ is the equilibrium Maxwell-Boltzmann distribution defined by:

$$f_s^{(0)}(\mathbf{C}, \mathcal{E}_{int}) = \left(\frac{\beta}{\pi^{1/2}} \right)^3 \frac{g_{int}}{Z_{int}} \exp \left[-(\beta^2 C_x^2 + \beta^2 C_y^2 + \beta^2 C_z^2) - \mathcal{E}_{int} \right]. \quad (3.13)$$

Here, $Z_{int} = Z_{rot} Z_{vib}$ is the internal partition function, which can be written as the product of Z_{rot} and Z_{vib} assuming the molecules in the system follow rigid rotator and harmonic oscillator models, and $\mathcal{E}_{int} = \epsilon_{int}/k_b T_{int}$ is the scaled internal energy. In this work, it is assumed [57] that the rotational relaxation occurs rapidly such that $T_{tr} \approx T_{rot}$, resulting in the scaling $\mathcal{E}_{rot} = \epsilon_{rot}/k_b T_{tr}$. Vibrational relaxation processes occur at a much longer timescale, such that $T_{tr} \neq T_{vib}$, resulting in the scaling $\mathcal{E}_{vib} = \epsilon_{vib}/k_b T_{vib}$. Note also that the degeneracy g_{vib} of the harmonic oscillator is unity. In (3.12), $\Gamma_s(\mathbf{C}, \mathcal{E}_{int}) = 1 + \phi_{GCE,s}(\mathbf{C}, \mathcal{E}_{int})$ is the perturbation function describing the small departure from the equilibrium state for species s , which may be expressed in terms of the macroscopic fluxes as:

$$\begin{aligned} \Gamma_s(\mathbf{C}, \mathcal{E}_{int}) = & 1 + 2(\mathbb{D}_{x,s} \mathcal{C}_{x,s} + \mathbb{D}_{y,s} \mathcal{C}_{y,s} + \mathbb{D}_{z,s} \mathcal{C}_{z,s}) \\ & + (q_{x,s} \mathcal{C}_{x,s} + q_{y,s} \mathcal{C}_{y,s} + q_{z,s} \mathcal{C}_{z,s}) \left(\frac{2}{5} \mathcal{C}_s^2 - 1 \right) \\ & + (\tilde{q}_{int,x,s} \mathcal{C}_{x,s} + \tilde{q}_{int,y,s} \mathcal{C}_{y,s} + \tilde{q}_{int,z,s} \mathcal{C}_{z,s}) (\mathcal{E}_{int,s} - \bar{\mathcal{E}}_{int,s}) \\ & - 2(\mathcal{C}_{x,s} \mathcal{C}_{y,s} \tau_{xy,s} + \mathcal{C}_{x,s} \mathcal{C}_{z,s} \tau_{xz,s} + \mathcal{C}_{y,s} \mathcal{C}_{z,s} \tau_{yz,s}) \\ & - \mathcal{C}_{x,s}^2 \tau_{xx,s} - \mathcal{C}_{y,s}^2 \tau_{yy,s} - \mathcal{C}_{z,s}^2 \tau_{zz,s}. \end{aligned} \quad (3.14)$$

The perturbation $\phi_{GCE,s}$ in (3.14) is the Generalized Chapman-Enskog (GCE) perturbation, which is written in terms of the dimensionless species diffusion flux, shear stress and heat flux components. As will be shown in Section 3.4,

these dimensionless fluxes, or breakdown parameters, can be used as a measure of the non-equilibrium nature of the flowfield, and are demonstrated to provide an indication of the importance of the diffusion and internal heat fluxes on the overall perturbation. The translational heat flux and shear stress components in (3.14) are defined as before in (3.4) and (3.5) for species s :

$$\tau_{ij,s} = \frac{\mu_s}{p_s} \left(\partial_j v_i + \partial_i v_j - \frac{2}{3} \partial_k v_k \delta_{ij} \right) = \frac{\tau_{ij,s}^{NS}}{p_s}, \quad (3.15)$$

$$q_{i,s} = -\frac{2\beta_s}{p_s} K_s \partial_i T_s = \frac{2\beta q_{i,s}^{NS}}{p_s}, \quad (3.16)$$

and for the gas mixture we introduce the dimensionless diffusion and internal heat flux components defined as:

$$\mathbb{D}_{i,s} = \frac{\beta_s \rho_s V_{i,s}}{\rho_s} = \frac{\beta_s D_{i,s}^{NS}}{\rho_s}, \quad (3.17)$$

$$\tilde{q}_{int,i,s} = -\frac{2\beta_s K_{int,s}}{\rho_s c_{int,s} T_{int,s}} \partial_i T_{int,s} = \frac{2\beta_s q_{int,i,s}^{NS}}{\rho_s c_{int,s} T_{int,s}}, \quad (3.18)$$

where $D_{i,s}^{NS} = \rho_s V_{i,s}$ is the species diffusion flux, and c_{int} represents the internal (rotational or vibrational) specific heats. The bulk viscosity is not considered in this work and is excluded in the derivation of the perturbation function. The details of the formulation of $\phi_{GCE,s}$ are provided in Appendix B.

Proceeding in the same way as for the simple gas, we would like to determine the distribution function of the molecules of species s within this reservoir which cross the surface reservoir boundary at $x = 0$ and enter into the computational domain per unit time and area. The ratio of the flux of species s molecules which cross the hybrid surface into the computational domain to

the total flux of molecules that would enter into the computational domain is expressed as:

$$f_{SR,s}^{(1)}(\mathbf{C}, \mathcal{E}_{int})d\mathbf{C} = \frac{n(C_x + u_s)f_s^{(1)}(\mathbf{C}, \mathcal{E}_{int})dC_zdC_ydC_x}{n \int_{-u}^{\infty} \int_{-\infty}^{\infty} \int_{-\infty}^{\infty} (C_x + u_s)f_s^{(1)}(\mathbf{C}, \mathcal{E}_{int})dC_zdC_ydC_x}. \quad (3.19)$$

After evaluation of this expression, we arrive at the distribution function for particles of species s generated at a surface reservoir within a non-equilibrium gas mixture:

$$f_{SR,s}^{(1)}(\mathbf{C}, \mathcal{E}_{int}) = f_{SR,s}(C_x)f_{SR,s}(C_y)f_{SR,s}(C_z)\Gamma_s(\mathbf{C}, \mathcal{E}_{int}). \quad (3.20)$$

Again, we have expressed this distribution as a product of the surface reservoir distributions and the corresponding perturbation. The tangential surface reservoir distributions, $f_{SR,s}(C_y)$, $f_{SR,s}(C_z)$ of expression (3.20) follow regular Maxwellian distributions:

$$f_{SR,s}(C_y, C_z) = \left(\frac{\beta_s}{\pi^{1/2}} \right) \exp(-\beta^2 C_{(y,z)}^2), \quad (3.21)$$

The normal surface reservoir distribution $f_{SR,s}(C_x)$ of expression (3.20) contains the form of the equilibrium one-sided Maxwellian distribution, but is modified by the integration over the perturbation included in (3.19), and is

given as:

$$\begin{aligned}
f_{SR,s}(C_x) = & \frac{2\beta_s^2(C_x + u_s) \exp(-\beta_s^2 C_x^2) / (u_s \sqrt{\pi} \beta_s)}{\left\{ 1 + \operatorname{erf}(\beta_s u_s) + \frac{1}{u_s \sqrt{\pi} \beta_s} \exp(-\beta_s^2 u_s^2) + \frac{\mathbb{D}_{x,s}}{u_s \beta_s} [1 + \operatorname{erf}(\beta_s u_s)] \right.} \\
& - \frac{q_{x,s}}{5\sqrt{\pi}} \exp(-\beta_s^2 u_s^2) + \frac{\tilde{q}_{int,x,s}(\mathcal{E}_{int,s} - \bar{\mathcal{E}}_{int,s})}{2u_s \beta_s} (1 + \operatorname{erf}(\beta_s u_s)) \\
& - \left[\frac{1}{u_s \sqrt{\pi} \beta_s} \exp(-\beta_s^2 u_s^2) + \frac{1}{2} [1 + \operatorname{erf}(\beta_s u_s)] \right] \tau_{xx,s} \\
& - \frac{1}{2} \left[\frac{1}{u_s \sqrt{\pi} \beta_s} \exp(-\beta_s^2 u_s^2) + [1 + \operatorname{erf}(\beta_s u_s)] \right] \tau_{yy,s} \\
& \left. - \frac{1}{2} \left[\frac{1}{u_s \sqrt{\pi} \beta_s} \exp(-\beta_s^2 u_s^2) + [1 + \operatorname{erf}(\beta_s u_s)] \right] \tau_{zz,s} \right\}. \quad (3.22)
\end{aligned}$$

Particles are generated from the distribution given by (3.20) following an approach similar to that for the simple gas, however the distribution for the gas mixture is computed specifically for each species according to the species-specific flux information provided by the Navier-Stokes solution. The perturbation function is now dependent on the particle internal energy as well as the thermal velocity, thus the rotational and vibrational internal energy levels must be determined for each particle before the perturbation function can be completely specified. It is also important to note that the non-equilibrium distribution for a gas mixture with internal energy is prescribed by a perturbation of the Maxwell-Boltzmann distribution (3.13). This perturbation therefore describes not only the non-equilibrium nature of the velocity distribution functions, but also the non-equilibrium nature of the internal energy distribution functions, according to the macroscopic flux quantities comprising the perturbation in (3.14). In order to sample this distribution, both the ther-

mal velocities and internal energies are included in the acceptance/rejection step, thereby ‘filtering’ these sampled quantities to reflect the non-equilibrium nature of the flow. To generate particle thermal velocities and internal energies from the non-equilibrium distribution in (3.20), we use the following acceptance-rejection algorithm:

1. Generate the particle rotational and vibrational energy from the Boltzmann distribution according to [2]:

$$(a) \ \epsilon_{rot} = -\log(\mathcal{R}_u)k_bT_{rot}, \text{ such that } \mathcal{E}_{rot} = \epsilon_{rot}/k_bT_{tr},$$

$$(b) \ \epsilon_{vib} = ik_b\Theta_v \ (i = \lceil -\log(\mathcal{R}_u)T_{vib}/\Theta_v \rceil), \text{ such that } \mathcal{E}_{vib} = \epsilon_{vib}/k_bT_{vib}. \\ (\Theta_v \text{ is the characteristic vibrational temperature of species } s)$$

2. Generate the equilibrium thermal velocity components $(\mathcal{C}_x, \mathcal{C}_y, \mathcal{C}_z)$ from the distributions given by (3.21) and (3.22). (sampling details are outlined in Appendix A)

3. Compute the average rotational and vibrational energy of a particle using the rigid rotor/harmonic oscillator approximations [2]:

$$(a) \ \bar{\mathcal{E}}_{rot} = \frac{k_bT_{rot}}{k_bT_{tr}},$$

$$(b) \ \bar{\mathcal{E}}_{vib} = \frac{\left(\frac{k_b\Theta_v}{\exp(\Theta_v/T_{vib}) - 1} \right)}{k_bT_{vib}}.$$

4. Compute the amplitude parameter $A = 1 + 30B$, where B is the breakdown parameter determined by $B = \max(|\mathbb{D}_s|, |\tau_{ij,s}|, |q_{i,s}|, |\tilde{q}_{int,i,s}|)$.

5. If $(A\mathcal{R}_u \leq \Gamma_s(\mathbf{C}, \mathcal{E}_{int}))$, accept $(\mathcal{C}_x, \mathcal{C}_y, \mathcal{C}_z, \mathcal{E}_{rot}, \mathcal{E}_{vib})$, otherwise go to (1).
6. If non-zero bulk velocity components exist in the tangential (y, z) directions, these are simply added to the accepted thermal velocity components from Step (5), yielding $(\mathcal{C}_x, \mathcal{C}_y + \beta v, \mathcal{C}_z + \beta w)$.

Thus, the macroscopic Navier-Stokes quantities Q_{SR} required for generating the DSMC particles at the non-equilibrium hybrid interface within a gas mixture are:

$$Q_{SR,s} = (D_s^{NS} \ n_s \ p \ \rho_s \ T_{tr,s} \ T_{rot,s} \ T_{vib,s} \ c_{rot,s} \ c_{vib,s} \ v_i \ \tau_{ij,s}^{NS} \ q_{i,s}^{NS} \ q_{int,i,s}^{NS}). \quad (3.23)$$

If species-specific flux information is not available for the shear stress or heat fluxes, then lower-fidelity mixture quantities may be used instead.

3.4 Evaluation of the breakdown parameters in a five-species air gas mixture

In this section, we present a simple analysis to assess the importance of the additional diffusion and internal heat flux terms that are introduced through the formulation of the Generalized Chapman-Enskog perturbation. The analysis that is outlined in this section is applied to two general flow cases, but this analysis can be easily extended to any Navier-Stokes flowfield solution to determine (a) where the Navier-Stokes solution breaks down (spatially), and (b) the macroscopic flux parameter(s) that lead to breakdown, according to

the breakdown criterion of $B \leq 0.1$ suggested for Chapman-Enskog particle generation [23]. Finally, this analysis can be used to determine whether DSMC particles may be generated from the regular Chapman-Enskog distribution (in cases where diffusion or internal heat flux contributions are negligible), or if the Generalized Chapman-Enskog distribution is required. To demonstrate this analysis, we evaluate the relative sizes of each of the breakdown parameters in two types of flows: (1) hypersonic flat-plate boundary layer flow, and (2) the breakdown region near a shock formed by two-dimensional hypersonic flow over a cylinder.

In each of these cases, we consider a reacting five-species air gas mixture, with the freestream conditions shown in Table 3.1. In both cases, the flat plate and cylinder surfaces are treated as non-catalytic, isothermal walls (where $T_w = 1000\text{ K}$), and a no-slip wall condition is enforced. The flowfields are computed using DPLR [88], in which reactions are computed using Park's finite-rate chemistry model [61]. The flow is modeled allowing for translational, rotational and vibrational thermal non-equilibrium, and the mixture transport coefficients (diffusion, viscosity and thermal conductivities) are computed using the self-consistent effective binary diffusion (SCEBD) and Gupta-Yos models [34, 66]. Note that the SCEBD model uses a mixing rule to approximate the effective diffusion coefficient of each species s in the gas mixture, while the Gupta-Yos model computes mixture viscosity and thermal conductivities. Therefore, in the analysis of the cases that follow, the flux parameters (given by (3.15) - (3.18)) and perturbations (ϕ_{CE} from (3.3) and $\phi_{GCE,s}$ from (3.14))

or (B.29)) are determined using *species-specific* diffusion fluxes and *mixture* shear stress and heat fluxes that are output from the DPLR solution.

Table 3.1: Freestream Conditions

	Flat Plate (boundary layer)	Cylinder (normal shock)
M	3.0	11.4
p	2100 Pa	52 Pa
T	4000 K	265 K
u	4100 m/s	3740 m/s
χ_{N_2}	6.04×10^{-1}	7.9×10^{-1}
χ_{O_2}	1.0×10^{-3}	2.1×10^{-1}
χ_{NO}	7.0×10^{-3}	—
χ_N	8.0×10^{-3}	—
χ_O	3.80×10^{-1}	—

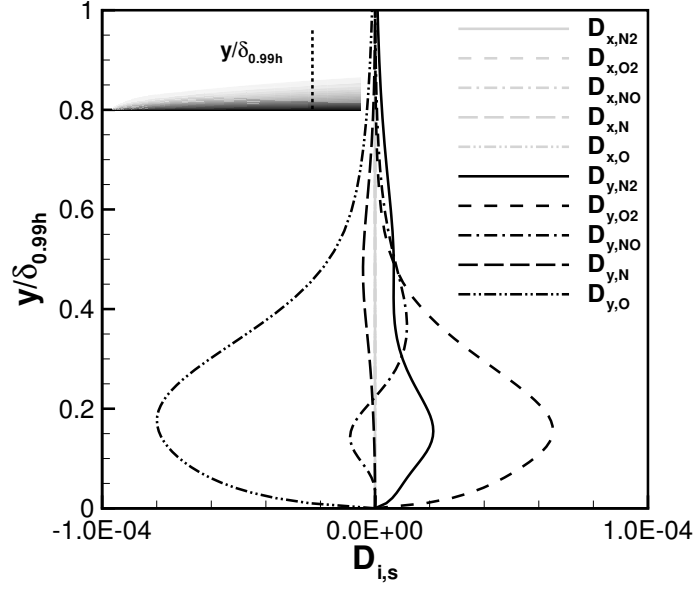
3.4.1 Hypersonic 2-D boundary layer flow

The breakdown parameters from the flat-plate boundary layer flow case are presented in Figure 3.4 and Figure 3.5. The diffusion, shear stress and heat flux breakdown parameters were computed according to (3.15)-(3.18), using either species-specific or mixture quantities as stated previously. The breakdown parameters are plotted as a function of wall-normal distance, normalized by the boundary layer thickness, $\delta_{0.99h}$, as indicated schematically in Figure 3.4(a). The boundary layer thickness was determined as the location above the surface where the enthalpy had recovered to 99% of the freestream value.

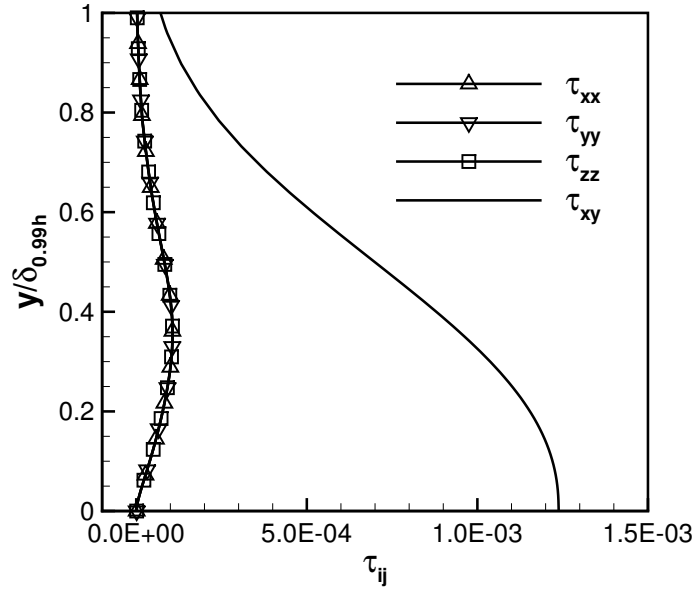
In Figure 3.4(a), the diffusion breakdown parameter is plotted for each

species s , and for each flux direction (x, y) in the boundary layer flow. The diffusion flux computed in DPLR is determined for gradients in concentration only, while the thermal diffusion (flux due to gradients in temperature) is neglected. Note that the diffusion fluxes due to streamwise concentration gradients ($\mathbb{D}_{x,s}$) are all essentially zero. The diffusion fluxes due to wall-normal concentration gradients ($\mathbb{D}_{y,s}$) are largest near the wall, with maximum values observed at approximately $0.2\delta_{0.99h}$. The strongest diffusion occurs for the atomic oxygen and molecular oxygen, and all diffusion fluxes decay towards zero approaching the boundary layer edge. The magnitudes of the diffusion breakdown parameters are relatively small in comparison to the shear stress breakdown parameters, shown in Figure 3.4(b). The relevant stress tensor quantities in this two-dimensional boundary layer flow are the normal stress components, $\tau_{xx}, \tau_{yy}, \tau_{zz}$ and the shear stress component τ_{xy} , while the remaining stress tensor components are zero. The maximum values of the normal stress breakdown parameters are comparable in magnitude to the diffusion breakdown parameters, but the shear stress breakdown parameter is an order of magnitude larger, with a maximum value at the wall of approximately 1.25×10^{-3} .

The heat flux breakdown parameters are provided in Figure 3.5(a) as a function of wall-normal distance. The parameters in the figure represent the translational, rotational and vibrational heat fluxes due to streamwise and wall-normal temperature gradients. Note again that the streamwise component of the heat flux breakdown parameters are essentially zero, as shown

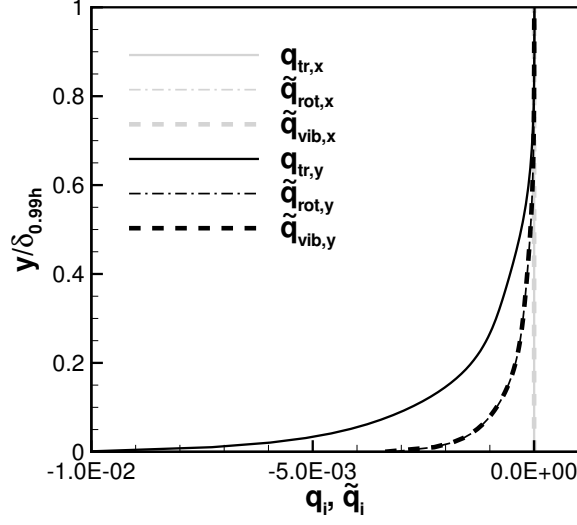


(a) Diffusion breakdown parameter, $\mathbb{D}_{i,s}$ (per flux direction, per species) through boundary layer.

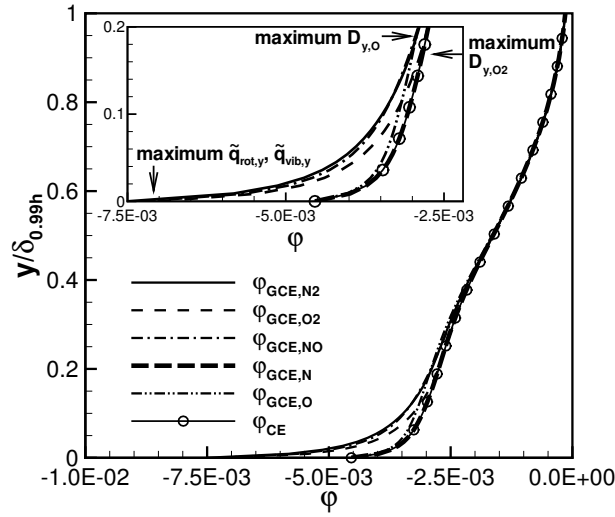


(b) Shear stress breakdown parameter, τ_{ij} (per tensor component) through boundary layer.

Figure 3.4: Breakdown parameters (a) $\mathbb{D}_{i,s}$, (b) τ_{ij} through a hypersonic 2-D boundary layer in five-species air, plotted as a function of wall-normal distance (shown schematically in the inset figure of (a)).



(a) Heat flux breakdown parameter, q_i , \tilde{q}_i (per mode, per flux direction) through boundary layer.



(b) Comparison of perturbation, $\phi_{GCE,s}$ (Generalized Chapman-Enskog (GCE) per species), ϕ_{CE} (Chapman-Enskog (CE)) through boundary layer.

Figure 3.5: Breakdown parameters (a) q_i , \tilde{q}_i through a hypersonic 2-D boundary layer in five-species air, plotted as a function of wall-normal distance (shown schematically in the inset figure of Figure 3.4(a)). (b) Comparison of perturbation ϕ computed using Chapman-Enskog (CE) formulation (Equation (3.3)) or Generalized Chapman-Enskog (GCE) formulation for each species (Equation (3.14)).

for $q_{tr,x}$, $\tilde{q}_{rot,x}$, and $\tilde{q}_{vib,x}$. Each of the wall-normal heat flux breakdown parameters have maximum values at the wall, and it is observed that for this boundary layer flow solution, $q_{tr,y}$ provides the largest contribution to the non-equilibrium perturbation up to a distance of approximately $0.4\delta_{0.99h}$. It is also important to note that the internal heat flux breakdown parameters are approximately the same magnitude as the shear stress breakdown parameter throughout the boundary layer, which suggests the importance of including the internal energy contributions in determining the non-equilibrium velocity distribution function.

To assess the significance of these breakdown parameters, we use the breakdown parameter profiles provided in Figures 3.4 and 3.5, as well as the local flowfield information, to approximate the perturbation ϕ in the boundary layer according to the Generalized Chapman-Enskog formulation $\phi_{GCE,s}$ (3.14) and the Chapman-Enskog formulation ϕ_{CE} (3.3). The particle thermal velocity and the particle internal energies are approximated by their most probable values, and so \mathcal{C}_i and \mathcal{E}_{int} in these expressions take on values of unity for purposes of this approximation. The purpose of this comparison between the perturbations ϕ_{GCE} and ϕ_{CE} is to understand the overall effect of the additional diffusion and internal heat flux contributions on the calculation of the perturbed distribution function. The resulting profiles are shown in Figure 3.5(b). The perturbations computed from the Generalized Chapman-Enskog formulation for each of the five species are represented by the solid and broken lines, and are plotted as a function of wall-normal distance. The solid

line with an open circle symbol represents the perturbation computed from the regular Chapman-Enskog formulation. Several observations can be made from the comparison of these perturbations. First, it is seen that the perturbations are nearly indistinguishable in the outer part of the boundary layer, for $0.4 < y/\delta_{0.99h}$. It is also observed that the perturbation $\phi_{GCE,N}$ for atomic nitrogen follows the Chapman-Enskog perturbation ϕ_{CE} almost perfectly, which is consistent with the fact that the diffusion flux of atomic nitrogen is very small throughout the boundary layer, as shown in Figure 3.4(a). The perturbation $\phi_{GCE,O}$ of atomic oxygen, on the other hand, is seen to deviate slightly from ϕ_{CE} by approximately 5% at a distance $0.2\delta_{0.99h}$, which corresponds to the location of maximum diffusion flux $\mathbb{D}_{y,O}$ in the boundary layer.

The comparison of the perturbations ϕ_{GCE} and ϕ_{CE} for the molecular species N_2, O_2 and NO show considerable differences near the wall (Figure 3.5(b), enlarged inset figure), which can be attributed to the inclusion of the internal heat flux in the calculation of the perturbation ϕ_{GCE} . The magnitude of the Generalized Chapman-Enskog perturbation at the wall is approximately 30 – 40% larger than the perturbation predicted by the Chapman-Enskog formulation. The perturbation ϕ_{GCE,O_2} of molecular oxygen is driven towards the Chapman-Enskog perturbation ϕ_{CE} for wall-normal distances greater than $0.2\delta_{0.99h}$, which corresponds to the large positive diffusion flux observed in this region in Figure 3.4(a). Approaching the wall, however, the heat flux contribution dominates the perturbation, and the perturbation ϕ_{GCE,O_2} follows the asymptotic trend of the other molecular constituents (molecular

nitrogen and nitric oxide) toward the wall. Note that the diffusion flux breakdown parameters of molecular nitrogen and nitric oxide are comparatively small throughout the boundary layer. It should also be noted that although the perturbation ϕ_{GCE} becomes considerably larger than ϕ_{CE} near the wall, the magnitude of the breakdown parameters are less than 0.1 throughout the boundary layer, and thus Generalized Chapman-Enskog Theory is still expected to adequately represent the perturbation of the velocity distribution function [23].

3.4.2 Hypersonic flow over a cylinder (normal shock flow)

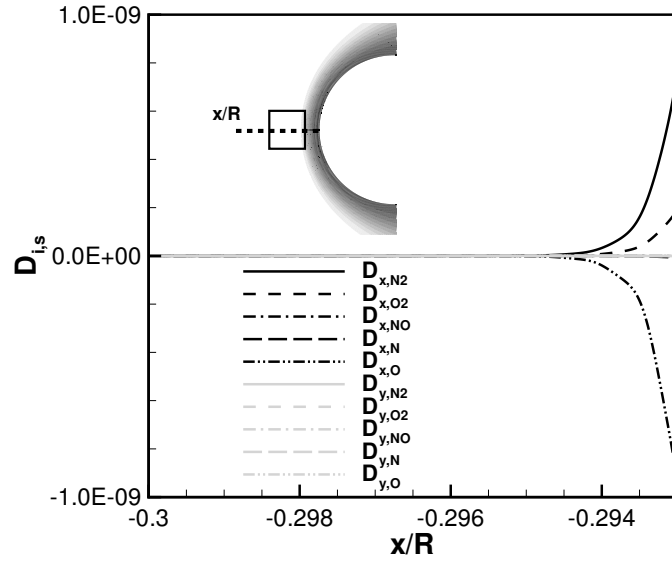
The breakdown parameters from the hypersonic flow over a cylinder are shown in Figure 3.6 and Figure 3.7 as a function of the distance along the stagnation line x/R , where the cylinder surface is located at $x/R = 0$, and the shock is located at $x/R \approx -0.289$. The diffusion flux, shear stress and heat flux breakdown parameters are computed in the same way as discussed in Section 3.4.1. Unlike the boundary layer flow case, the gradients within the normal shock become large very quickly, and the breakdown criterion is exceeded by the parameters at various x/R locations. To present the results from this analysis, we only show the breakdown parameter profiles up to the x/R location where the first parameter exceeds the breakdown criterion, $B \leq 0.1$. This region is upstream of the normal shock, and is represented schematically in the inset figure of Figure 3.6(a). As will be shown, the translational heat flux parameter exceeds this breakdown criterion first, at a location of

approximately $x/R = -0.293$. After this point (for larger values of x/R), the approximations used to formulate the perturbation become invalid.

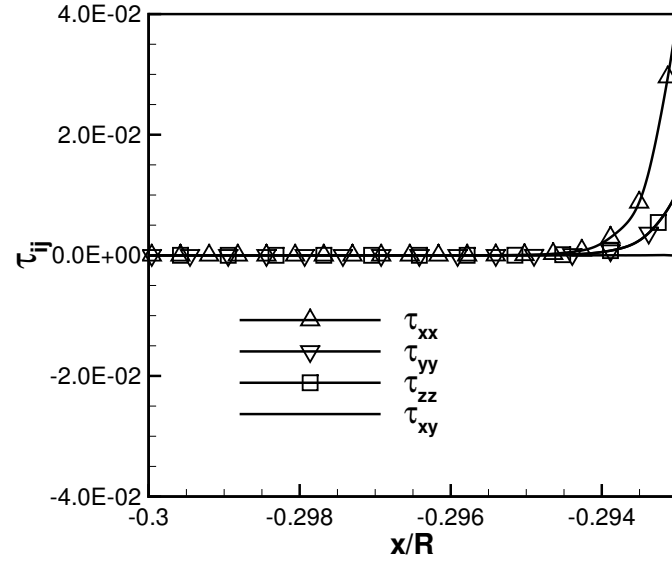
The diffusion flux breakdown parameters are shown in Figure 3.6(a) per flux direction and per species. Although the diffusion fluxes become larger within the shock and shock layer, they are completely negligible within the breakdown region presented here. This observation, as well as the resulting analysis of the boundary layer flow, suggests that the mass diffusion flux plays a relatively minor role in the total perturbation of the velocity distribution function.

The stress tensor breakdown parameters are shown in Figure 3.6(b). In this case, the normal stresses increase appreciably before the breakdown location, with $\tau_{xx} = 4.0 \times 10^{-2}$ and $\tau_{yy}, \tau_{zz} = 1.0 \times 10^{-2}$, while the shear stress parameter remains negligible, in contrast to the boundary layer flow case. The translational, rotational and vibrational heat flux parameters are presented next in Figure 3.7(a). The translational heat flux is the first parameter to exceed the breakdown criterion, with $|q_{tr}| = 0.1$ at a location of $x/R = -0.2935$. The values of the rotational and vibrational heat flux parameters, which lag the translational contribution, are also observed to increase before the breakdown location.

The dominance of this translational heat flux is evident in the total perturbation, plotted in Figure 3.7(b) as a function of distance x/R . In this figure, we have again computed the perturbation from the Generalized Chapman-Enskog formulation which includes the contributions from the diffusion fluxes

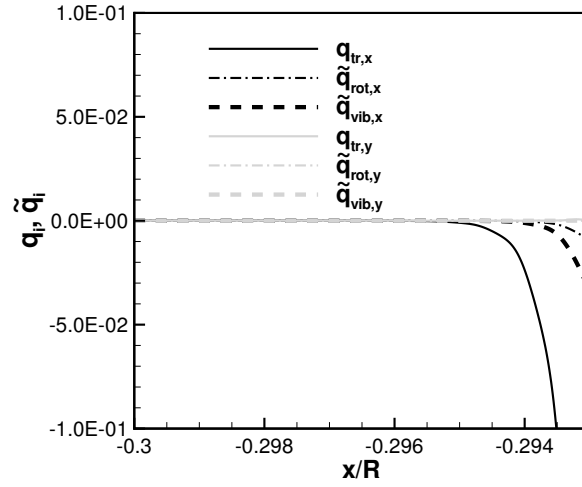


(a) Diffusion breakdown parameter, $\mathbb{D}_{i,s}$ (per flux direction, per species) along stagnation line, up to breakdown location.

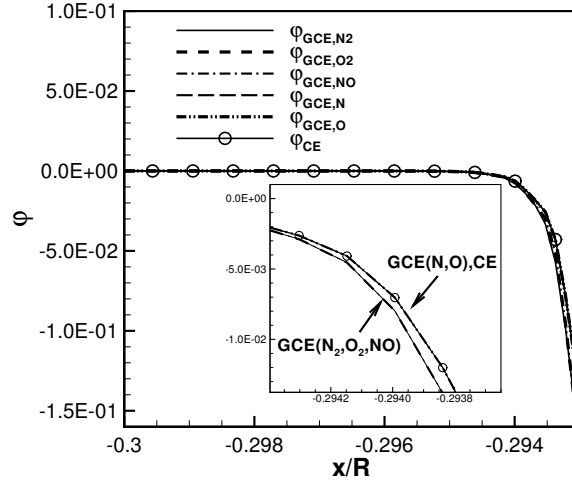


(b) Shear stress breakdown parameter, τ_{ij} (per tensor component) along stagnation line, up to breakdown location.

Figure 3.6: Breakdown parameters (a) $\mathbb{D}_{i,s}$, (b) τ_{ij} along the stagnation streamline, plotted as a function of streamwise distance in the breakdown region upstream of a normal shock (shown schematically in the inset figure of (a)).



(a) Heat flux breakdown parameter, q_i , \tilde{q}_i (per mode, per flux direction) along stagnation line, up to breakdown location.



(b) Comparison of perturbation, $\phi_{GCE,s}$ (Generalized Chapman-Enskog (GCE) per species), ϕ_{CE} (Chapman-Enskog (CE)) along stagnation line, up to breakdown location.

Figure 3.7: Breakdown parameters (a) q_i , \tilde{q}_i along the stagnation streamline, plotted as a function of streamwise distance in the breakdown region upstream of a normal shock (shown schematically in the inset figure of Figure 3.6(a)). (b) Comparison of perturbation ϕ computed using Chapman-Enskog (CE) formulation (Equation (3.3)) or Generalized Chapman-Enskog (GCE) formulation for each species (Equation (3.14)).

and internal heat fluxes on the total perturbation of the velocity distribution function. The curves representing the perturbation $\phi_{GCE,s}$ of the atomic species N, O are indistinguishable from the regular Chapman-Enskog perturbation; this underscores the fact that the diffusion flux has no effect on the total perturbation for this flow case. The curves representing the perturbation of the molecular species do deviate slightly from the regular Chapman-Enskog perturbation, due to the influence of the internal heat fluxes on the total perturbation, but this difference ($\approx 2\%$) is negligible in comparison to the boundary layer flow case. As indicated by the breakdown parameters in this analysis, it would be necessary to generate the surface reservoir at the breakdown location of $x/R \approx -0.293$, but it is seen that the regular Chapman-Enskog perturbation ϕ_{CE} adequately represents the total perturbation, and the use of the Generalized Chapman-Enskog perturbation is unnecessary for the normal shock flow conditions considered here.

3.5 Summary

As a recap, the first part of this chapter presented an approach for generating a hybrid DSMC/Navier-Stokes solution using a non-equilibrium surface reservoir. The non-equilibrium surface reservoir was first derived for a simple gas, in which the DSMC particles are assumed to follow the Chapman-Enskog distribution. The non-equilibrium surface reservoir formulation was then extended to gas mixtures with internal degrees of freedom, in which contributions from the species diffusion and internal energy flux terms were considered

in the Generalized Chapman-Enskog framework. This extension allows for a non-equilibrium description of the thermal velocity distributions as well as the internal energy distributions for hybrid particle sampling, based on the fluxes comprising the perturbation on the Maxwell-Boltzmann distribution.

To illustrate the significance of the additional diffusion and internal heat flux terms present in the Generalized Chapman-Enskog perturbation, the relative magnitudes of the diffusion, shear stress and heat flux parameters were examined at a hybrid interface within non-equilibrium boundary layer flow, as well as within the breakdown region near a normal shock. A simple analysis was also presented in which the Generalized Chapman-Enskog perturbations and the regular Chapman-Enskog perturbation were approximated and compared within the non-equilibrium flow regions. The purpose of this analysis was to present a detailed and systematic approach to determine, for a five-species air gas mixture:

1. The breakdown location in the Navier-Stokes flowfield solution, which is determined as the location where the first parameter exceeds the breakdown criterion ($B \leq 0.1$).
2. How the Navier-Stokes solution breaks down, as indicated by the breakdown parameters $\mathbb{D}_{i,s}$, τ_{ij} , q_i and $\tilde{q}_{int,i}$.
3. Whether the hybrid interface requires the Generalized Chapman-Enskog perturbation to properly describe the perturbed distribution function, or if the Chapman-Enskog perturbation is sufficient.

Chapter 4

Consistent Treatment of Transport Coefficients

4.1 Overview

The quality of a hybrid simulation involving direct simulation Monte Carlo (DSMC) and Navier-Stokes (CFD) solvers relies on the level of consistency achieved in the physical models employed by the flow solvers, including models for mass, momentum and energy transport as well as thermo-chemical models [40, 79, 80]. This work presented in this chapter aims to address the consistency of transport properties between DSMC and CFD solvers in the context of either hybrid applications or general comparisons between independent DSMC and CFD solutions. Finally, conclusions and recommendations for use of these fitted parameters in DSMC applications are given in Section 4.5.

4.2 Transport Properties in CFD and DSMC

Within many CFD solvers, the coefficients of diffusion, viscosity and thermal conductivity for a gas mixture may be computed directly from Chapman-Enskog theory, which determines the transport fluxes to first order in the So-

nine polynomial expansion. Simplified approaches have been developed for approximation of the transport coefficients for gas mixtures. These approximate methods generally adopt simplifications to the Chapman-Enskog solution through the use of mixing rules, and provide reasonable results at low to moderate temperatures for neutral gas mixtures. The details of these transport models are available in the literature [3, 15, 34, 66, 86], and comparisons have been made among the models regarding their computational efficiency and accuracy relative to the full Chapman-Enskog solution [45, 51, 60]. The transport coefficients generated from these models are often obtained from expressions involving the collision integrals as a function of temperature. The collision integrals are computed from potentials based on *ab initio* calculations [76, 77] or from potentials determined from experimental analysis [16] (e.g., molecular-beam scattering results).

The DSMC method does not use a direct model to obtain the transport coefficients of the gas; rather, DSMC uses a variety of collision cross section models, in which the simulation particles are modeled as spheres of diameter d which is a function of g , the relative speed of the collision pair. The transport properties are a result of the transfer of mass, momentum and energy through particle movement and collision dynamics; the transport properties are thus adjusted by modifying the parameters used in the collision model. In this work, the variable hard sphere (VHS) and variable soft sphere (VSS) models are considered, although other models exist [2, 37]. To determine the proper adjustment or calibration of these collision model parameters, the DSMC col-

lision cross sections can be used to compute the collision integrals $\Omega_{st}^1(1)$ and $\Omega_{st}^2(2)$ and ratio of collision integrals B_{st} , allowing for the calculation of the DSMC transport coefficients from Chapman-Enskog Theory. This formulation enables a direct comparison between the transport coefficients obtained from the more realistic intermolecular potentials (herein referred to as *first principles* calculations) in CFD solvers, and those obtained from the phenomenological cross section models in DSMC. It also allows for a systematic calibration of the DSMC model parameters to obtain consistency in the transport coefficients employed in DSMC/CFD applications.

The VHS collision model is widely used throughout the DSMC community, and has been found to yield good agreement in the viscosity and thermal conductivity coefficients when used for hybrid simulations involving simple (single-species) gases [71, 79]. Deficiencies in the VHS collision model make its extension to hybrid simulations involving gas mixtures difficult, as consistency in the transport properties must be extended to include the mass diffusion coefficients. As an alternative to VHS, the VSS collision model was introduced by Koura and Matsumoto as a preferred collision model for use in Monte Carlo simulations of gas mixtures when species diffusion plays an important role [43]. The diffusion process is particularly important when considering chemically reacting flows or flows involving interaction with catalytic surfaces, as the dominant heat flux contribution comes from the diffusion heat flux. The diffusion heat flux arises due to the transport of energy through dissociation/recombination reactions that occur as a result of the diffusion

process, which is in turn driven by gradients in pressure, temperature and species concentration.

The aim of this work is to establish a general approach for achieving consistency in the transport properties between DSMC and CFD solvers. To this end, it is assumed that the transport coefficients determined from more realistic intermolecular potentials within the CFD transport models serve as the ‘standard’ values for coefficients of diffusion, viscosity and thermal conductivity. The details regarding the formulation of the DSMC transport coefficients from Chapman-Enskog Theory are provided in Section 4.3.1. The DSMC transport coefficients are compared to the transport coefficients computed from first principles, and a least-squares fitting process (described in Section 4.3.2) is employed. In the fitting process, the VHS and VSS collision model parameters are calibrated to provide the best fit of the DSMC transport coefficients to the transport coefficients from first principles. The aim of this DSMC parameter calibration is two-fold. We would first like to determine which model (VHS or VSS) is best-suited to modeling a five-species air mixture relative to the transport coefficients determined from first principles. The second objective is to present a recommended set of DSMC collision model parameters that provide optimal agreement with the transport coefficients computed from more realistic intermolecular potentials over a range of temperatures and that are common to non-ionized re-entry boundary layer flow conditions. The results from the fitting process and recommended VHS/VSS parameter values are presented in Section 4.4.

4.3 Consistent Treatment of Transport Properties in DSMC and CFD Solvers

As mentioned previously, the transport coefficients determined from first principles within the CFD transport models serve as the ‘standard’ values for the calibration of the DSMC collision model parameters. Various models are available for computing the mass diffusion, viscosity and thermal conductivity coefficients in continuum CFD solvers. In this work, the diffusion coefficients are determined using the self-consistent effective binary diffusion (SCEBD) model, and the viscosity and thermal conductivity coefficients are determined from the model by Gupta *et al.* with Yos approximate mixing rules (herein referred to as Gupta *et al.*-Yos) [34, 66]. In this section, the details of the VHS and VSS collision cross section models and corresponding collision integrals are presented, and the general fitting approach for the calibration of the DSMC collision model parameters is described.

4.3.1 Representation of Transport Properties in DSMC: VHS/VSS Collision Cross Section Models

The DSMC collision cross section models examined in this work include the variable hard sphere (VHS) and variable soft sphere (VSS) models. Within this framework, the DSMC simulation particles are modeled as hard spheres of diameter d which is a function of g , the relative speed of the collision pair, such that $d \sim (1/g)^{\omega-1/2}$. The VSS model also includes a scattering angle specified by the coefficient α , such that values of $\alpha > 1.0$ result in a scattering angle smaller than the corresponding value of the VHS model (in which $\alpha =$

1.0). The reduced scattering angle effectively establishes a forward-scattering tendency of the colliding particles. This feature in VSS provides a model in which both the diffusion and viscosity cross sections can be made consistent with those from any intermolecular potential [43].

The fitting of the transport coefficients computed from VHS/VSS cross sections to the transport coefficients from first principles is achieved through application of the Nelder-Mead Simplex Method, which is used to determine the set of VHS and VSS model parameters that provide the best fit in the transport coefficients. It should be mentioned that while this approach produces a single best-fit value for each parameter examined, more sophisticated approaches may be used to construct probability distributions describing the best fit model parameter values [54, 55]. Before outlining the Nelder-Mead approach, we first present the expressions used to determine the mixture diffusion, viscosity and thermal conductivity coefficients based on the VHS and VSS cross sections.

To allow for a consistent comparison to the species diffusion coefficients from the SCEBD model [66], we compute the effective diffusivities D_s from VHS/VSS cross sections according to

$$D_s = \left(1 - \frac{w_s}{w}\right) \left(\sum_{t \neq s} \frac{\chi_t}{\mathcal{D}_{st}}\right)^{-1}. \quad (4.1)$$

Here, χ_t is the mole fraction of species t , w and w_s represent the weighting factors defined as

$$w_s = \frac{\rho_s}{\sqrt{M_s}}, \quad (4.2)$$

$$w = \sum_s w_s. \quad (4.3)$$

In (4.2), ρ_s is the density of species s , M_s is the molar mass of species s , and \mathcal{D}_{st} is the binary diffusion coefficient for species pair s, t

$$\mathcal{D}_{st} = \frac{3k_b T}{16nm_{st}^* \Omega_{st}^1(1)}. \quad (4.4)$$

In (4.4), k_b is Boltzmann's constant, n and T are the number density and temperature, respectively, and m_{st}^* is the reduced mass. In the case of the species diffusion, it would be best to use the full matrix of multicomponent (Chapman-Enskog) diffusion coefficients, D_{st} , in the fitting process directly, rather than using the effective binary diffusion coefficients as shown in (4.1). However, the SCEBD model considered in this work uses a mixing rule to approximate the full multicomponent diffusion coefficient matrix as five effective binary diffusion coefficients, D_s . We therefore adopt this model to represent the species diffusion coefficients from VHS/VSS, allowing for a consistent comparison between the two sets of transport coefficients.

The mixture viscosity from the VHS/VSS cross section models can be determined from the first-order Chapman-Enskog approximation of the mixture viscosity [12] which is defined as

$$[\mu]_1 = \sum_s b_s. \quad (4.5)$$

The quantity b_s is the contribution of each species to the overall mixture viscosity [12] and may be determined by solving the following system

$$\chi_s = b_s \left\{ \frac{\chi_s}{[\mu_s]_1} + \sum_{t \neq s} \frac{3\chi_t}{(\rho'_s + \rho'_t)\mathcal{D}_{st}} \left(\frac{2}{3} + \frac{m_t}{m_s} A_{st} \right) \right\} - \chi_s \sum_{t \neq s} \frac{3b_t}{(\rho'_s + \rho'_t)\mathcal{D}_{st}} \left(\frac{2}{3} - A_{st} \right). \quad (4.6)$$

The quantities μ_s and A_{st} in (4.6) are defined as

$$[\mu_s]_1 = \frac{5k_b T}{8\Omega_1^2(2)}, \quad (4.7)$$

$$A_{st} = \frac{\Omega_{st}^2(2)}{5\Omega_{st}^1(1)}. \quad (4.8)$$

The terms ρ'_s, ρ'_t refer to the density of species (s, t) when pure at the pressure and temperature of the actual gas mixture, and m_s, m_t are the molecular masses of species s, t , respectively.

The mixture translational thermal conductivity [12] is determined by

$$[K_{tr}]_1 = \sum_s a_s. \quad (4.9)$$

The quantity a_s is the contribution of each species to the overall mixture translational thermal conductivity [12] and may be determined by solving the following system

$$\chi_s = a_s \left\{ \frac{\chi_s}{[\lambda_s]_1} + \sum_{t \neq s} \frac{T\chi_t}{5p\mathcal{D}_{st}} \left(6 \left[\frac{m_s}{(m_s + m_t)} \right]^2 + (5 - 4B_{st}) \left[\frac{m_s}{(m_s + m_t)} \right] \right. \right. \\ \left. \left. + 8 \frac{m_s m_t}{(m_s + m_t)^2} A_{st} \right) \right\} - \chi_s \sum_{t \neq s} a_t \left[\left(T \frac{m_s m_t}{(m_s + m_t)^2} \right) / 5p\mathcal{D}_{st} \right] (11 - 4B_{st} - 8A_{st}). \quad (4.10)$$

In (4.10) the quantities $[\lambda_s]_1$ and B_{st} are defined

$$[\lambda_s]_1 = \frac{25c_vk_bT}{16\Omega_1^2(2)}, \quad (4.11)$$

$$B_{st} = \frac{5\Omega_{st}^1(2) - \Omega_{st}^1(3)}{5\Omega_{st}^1(1)}, \quad (4.12)$$

where c_v is the specific heat at constant volume of species s , and p is the pressure of the gas mixture.

The rotational and vibrational conductivities are determined using Eucken's formula, in which it is assumed that the conductivity of the gas is separated into two non-interacting parts, $[K_{tr}]_1$ and K_{int} [12]. The internal thermal conductivities are given by

$$K_{rot} = \sum_{i \in s} \frac{\rho_i c_{rot}}{\sum_{j \in t} \chi_j / \mathcal{D}_{ij}}, \quad (4.13)$$

$$K_{vib} = \sum_{i \in s} \frac{\rho_i c_{vib}}{\sum_{j \in t} \chi_j / \mathcal{D}_{ij}}, \quad (4.14)$$

where ρ_i is the partial density defined as the product of the mixture density, ρ and the species mass fraction, Y_i

$$\rho_i = \rho Y_i. \quad (4.15)$$

Finally, the collision integrals involved in computing (4.5) and (4.9) and the ratio of collision integrals in (4.12) can be expressed in terms of the VHS parameters as follows

$$\Omega_{st}^1(1)\Big|_{VHS} = \frac{\pi}{2} d_{ref}^2 \left(\frac{k_b T}{2\pi m_{st}^*} \right)^{1/2} \left(\frac{T_{ref}}{T} \right)^{\omega-1/2} \left[\frac{\Gamma(7/2 - \omega)}{\Gamma(5/2 - \omega)} \right], \quad (4.16)$$

$$\Omega_{st}^2(2)\Big|_{VHS} = \frac{\pi}{3} d_{ref}^2 \left(\frac{k_b T}{2\pi m_{st}^*} \right)^{1/2} \left(\frac{T_{ref}}{T} \right)^{\omega-1/2} \left[\frac{\Gamma(9/2 - \omega)}{\Gamma(5/2 - \omega)} \right], \quad (4.17)$$

$$B_{st}\Big|_{VHS} = \frac{5\Gamma(9/2 - \omega) - \Gamma(11/2 - \omega)}{5\Gamma(7/2 - \omega)}. \quad (4.18)$$

The collision integrals are expressed according to the VSS collision model as

$$\Omega_{st}^1(1)\Big|_{VSS} = \left(\frac{2}{\alpha + 1} \right) \Omega_{st}^1(1)\Big|_{VHS}, \quad (4.19)$$

$$\Omega_{st}^2(2)\Big|_{VSS} = \left[\frac{4\alpha}{(\alpha + 1)(\alpha + 2)} \right] \Omega_{st}^2(2)\Big|_{VHS}. \quad (4.20)$$

The ratio of collision integrals $B_{st}\Big|_{VSS}$ for the VSS collision model is identical to the expression for $B_{st}\Big|_{VHS}$ given in (4.18). In (4.7), the collision integral $\Omega_1^2(2)$ is of the form given in (4.16) or (4.19) with $s = t$, and in (4.16)-(4.20), $\Gamma(x)$ is the gamma function. A detailed formulation of these collision integrals is provided in Appendix C.

Within DSMC, the VHS and VSS parameters in (4.16)-(4.20) are often determined simply as the average values of species s and t (e.g., $d_{ref} = \frac{1}{2}(d_{ref,s} + d_{ref,t})$), regardless of the specific collision partners involved in the collision. The model parameters determined using this approach are herein

referred to as *collision-averaged* values. When considering collisions within a gas mixture, however, the VHS and VSS model parameters should be prescribed for each specific collision pairing, rather than using a simple averaging rule for all collision pairs [2, 40]. The model parameters determined with this approach are herein referred to as *collision-specific* values.

4.3.2 Generation of Best-Fit VHS/VSS Parameters

The aim of the fitting process is to determine a best fit of the DSMC collision model parameters that yield good agreement between the transport coefficients determined from more realistic intermolecular potentials and from the VHS/VSS cross section models. The gas mixture considered in the present work is a five-species air gas mixture (N_2, O_2, NO, N, O). The conditions considered in this work represent typical boundary layer edge conditions for the Orbiter re-entry trajectory point of Mach 20, which corresponds to a pressure of 2300 *Pa*. The temperatures considered in the present work range from 1000 *K* to 5000 *K*, which are well within the limits of the transport models considered here. The transport coefficients obtained from first principles are computed at temperature increments of 100 *K* assuming an equilibrium or (prescribed) non-equilibrium composition.

Several approaches may be taken to achieve an optimal fit of the VHS and VSS parameters. Previous studies have used the collision integrals as the fitting metric to determine the best fit of the DSMC collision model parameters, while other works compute and fit to the transport coefficients di-

rectly [40, 43]. Use of the collision integrals in the fitting process is the more physically consistent approach, in that the collision integrals provide the link between the dynamics of binary collisions and the macroscopic transport coefficients. This work has found, however, that this approach does not allow for the best representation of the SCEBD/Gupta *et al.*-Yos transport coefficients by the VHS/VSS models when the DSMC collision model is inadequate (as may be the case for VHS applied to gas mixtures) or overconstrained (as may be the case for collision-averaged pairing). Under these circumstances, it is important to note that fits to the collision integrals do not inherently include any information regarding the composition of the gas mixture being considered, as the collision integrals are dependent on temperature only. This feature of the collision integrals is evident when considering gas mixtures comprising one or two primary constituents with several trace species. The use of collision integrals for the fitting of transport coefficients becomes problematic, since the fits made for collisions between trace species are weighted equally with collisions between the major constituents. A careful fitting of a collision model with a sufficient number of parameters should be able to overcome this issue, but the fitting of any collision model parameters in which the problem is over-constrained proves challenging without introducing a form of weighting in the fitting of the collision integrals.

The work presented here highlights the use of transport coefficients in the fitting process, because information regarding the gas mixture composition is inherently included in the determination of the transport coefficients.

In this work, only the reference diameters, temperature exponents and, where necessary, the VSS parameter α are considered as variable parameters in the fitting process, while the reference temperature is assumed to have a constant value of 2880 K. To remain physically consistent with the VHS and VSS models, the temperature exponent should be constrained to within the limits of a Maxwell molecule and a hard sphere molecule, such that ω is less than 1.0, but greater than 0.5. In the cases examined here, reasonable fits were achieved by allowing the reference diameter to remain unconstrained, while the temperature exponents were constrained to values of 0.73 ± 0.05 . The VSS exponent α is also constrained to remain within values of $1.0 < \alpha < 2.0$, where $\alpha = 1.0$ corresponds to the VHS deflection angle, and $\alpha = 2.0$ is an accepted upper limit to the VSS exponent [2]. The fits are generated for the VHS and VSS models using either *collision-averaged* or *collision-specific* pairing implementations. Considering the VHS model, this requires the solution of a best-fit problem involving ten parameters for the collision-averaged and thirty parameters for the collision-specific pairing approaches. The VSS model requires the solution of a best-fit problem involving fifteen parameters for the collision-averaged and forty-five parameters for the collision-specific pairing approaches.

To construct the fitting problem, initial values are prescribed for all VHS and VSS parameters. The transport coefficients are then computed and collectively expressed in vector form as a function of the VHS or VSS parameters (using collision integrals calculated from the VHS/VSS cross sections)

over the desired temperature range according to (4.1), (4.5), (4.9), (4.13), and (4.14). Note that while the transport coefficients of mass diffusion, viscosity and thermal conductivity are functions of temperature, the VHS and VSS parameters are not. A second vector comprising the transport coefficients given by the ‘standard’ SCEBD and Gupta *et al.*-Yos models (using collision integrals calculated from more realistic intermolecular potentials) is constructed, and the goal of the fitting process is to minimize the distance (or error) between the two vectors by adjusting the VHS or VSS parameters.

The VSS model is developed from the VHS model, and often the same values are used for the common parameters d_{ref} and ω . To this end, the parameters d_{ref} and ω are first calibrated by fitting the mixture viscosity and translational thermal conductivity coefficients from the VHS and Gupta *et al.*-Yos models. The additional parameter α in the VSS model mostly influences the diffusion-driven coefficients (i.e., the coefficients of diffusion and internal thermal conductivities). The VSS exponents α are thus subsequently calibrated by fitting the internal thermal conductivities and diffusion coefficients, while the d_{ref} and ω parameters are held ‘fixed’. It is important to note that while modification of the parameter α mostly affects the diffusion-driven coefficients, it does have a non-negligible influence on the viscosity and translational thermal conductivity coefficients. In some cases, the best-fit values of the parameters d_{ref} and ω used in the VSS model are allowed to relax slightly during the calibration of the α parameters, to achieve the best fit in all of the transport coefficients.

The adjustment of the VHS/VSS parameters is performed using the Nelder-Mead Simplex Method [46, 59]. This method uses an iterative direct search algorithm to determine the appropriate set of variables required to achieve a minimum difference between the two vectors. The vector of transport coefficients computed from the initial VHS/VSS parameter values forms the first function iteration. The simplex method then perturbs the parameters, and the new transport coefficients are computed and assembled into vector form. If the resulting perturbation produces a smaller distance between the vectors, the simplex method extends the perturbation in the same direction and continues the search. If the perturbation resulted in a larger distance between the two vectors, the simplex method searches in the opposite direction. For the fitting problems examined in this work, the Nelder-Mead algorithm demonstrated rapid convergence within several thousand iterations, and the solution was not sensitive to the initial values chosen, provided they were realistic. The convergence history and sensitivity of the best-fit parameters to the initial values is presented for one of the cases in Appendix D.

To demonstrate the improvement in the agreement between the transport coefficients using this fitting approach, we apply the same techniques to construct a fitting problem involving the collision integrals as a function of temperature as the fitting metric. Initial values are prescribed for all VHS and VSS parameters, and the collision integrals are computed and collectively expressed in vector form according to (4.16)-(4.18) or (4.18)-(4.20). A second vector comprising the collision integrals from first principles used in the

SCEBD/Gupta *et al.*-Yos models is constructed, and the Nelder-Mead Simplex Method is again applied to determine the set of best-fit VHS or VSS parameters. The best-fit VHS/VSS transport coefficients are then computed from these parameters and compared to the SCEBD/Gupta *et al.*-Yos transport coefficient values, allowing for comparison between the fitting approaches.

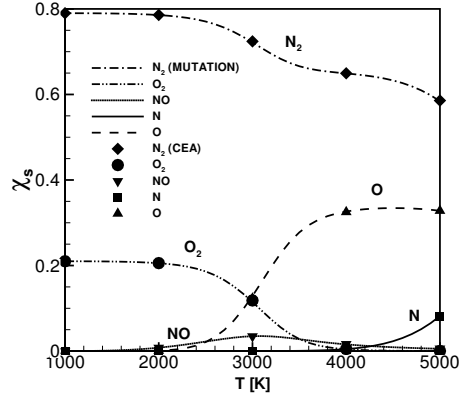
The aim of this DSMC parameter fitting is two-fold. We would first like to determine which model (VHS or VSS) is best-suited for modeling a five-species air mixture with regards to the transport coefficients discussed above. We then aim to establish the best approach for determining these quantities on a collisional basis, using either collision-averaged or collision-specific pairing. Both of these items are investigated in the context of a five-species air gas mixture in *chemical equilibrium*, in which the composition is well-defined. A recommended set of VHS/VSS collision model parameters are presented based on the equilibrium composition. These recommended collision model parameters are then examined for use in three (extreme) chemical non-equilibrium gas mixtures. The transport coefficients in these mixtures are computed from the DSMC collision models using the best fit parameters from the equilibrium transport coefficient fits, and from the collision integral fits. These values are then compared to the corresponding SCEBD/Gupta *et al.*-Yos values. The final objective is to provide a recommended set of collision model parameters that closely match the SCEBD and Gupta *et al.*-Yos transport coefficients over a range of temperatures that are common to non-ionized re-entry conditions.

4.4 Results

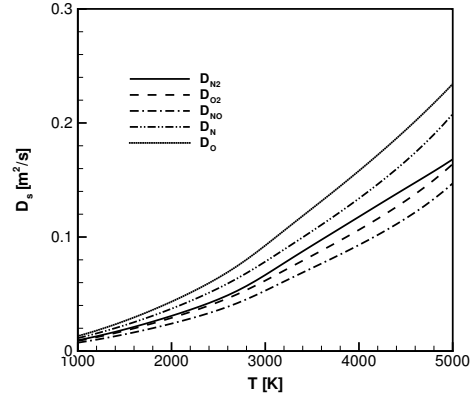
4.4.1 Equilibrium Composition and Transport Coefficients of Five-species Air

Before presenting the VHS and VSS fits, we first examine the diffusion, viscosity and thermal conductivity coefficients for the five-species air mixture from the SCEBD and Gupta *et al.*-Yos models. The transport coefficients are computed over the temperature range of $1000K$ to $5000K$ assuming an equilibrium mixture composition, which is computed using the MUTATION library [51]. The mixture composition is shown in Figure 4.1(a). It should be noted that the CEA thermodynamic database used for the calculation of the SCEBD/Gupta *et al.*-Yos transport coefficients is consistent with the MUTATION library, as demonstrated by the excellent agreement in the equilibrium composition shown in Figure 4.1(a). The species concentrations exhibit the strongest variation at temperatures of around $3000K$ and again at $5000K$, corresponding to the dissociation/recombination temperatures of O_2 and N_2 , respectively.

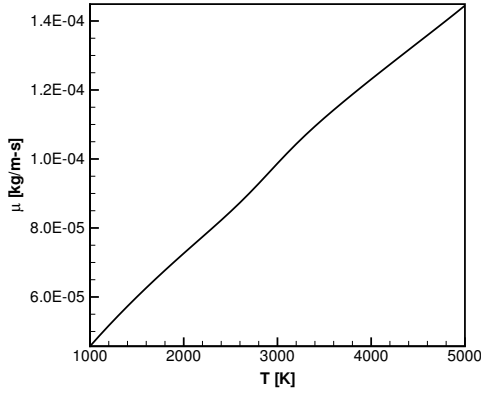
The effective binary diffusion coefficients, mixture viscosity coefficients and thermal conductivity coefficients of the gas mixture are shown in Figure 4.1(b-d) as a function of temperature. The translational thermal conductivity (shown by the solid line in Figure 4.1(d)) provides the largest contribution to the total mixture conductivity, and also shows the strongest variation due to dissociation/recombination of O_2 at $3000K$.



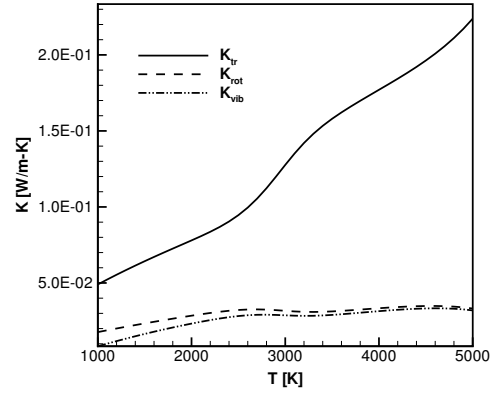
(a) Composition (by mole fraction).



(b) Effective diffusion coefficients.



(c) Mixture viscosity coefficient.



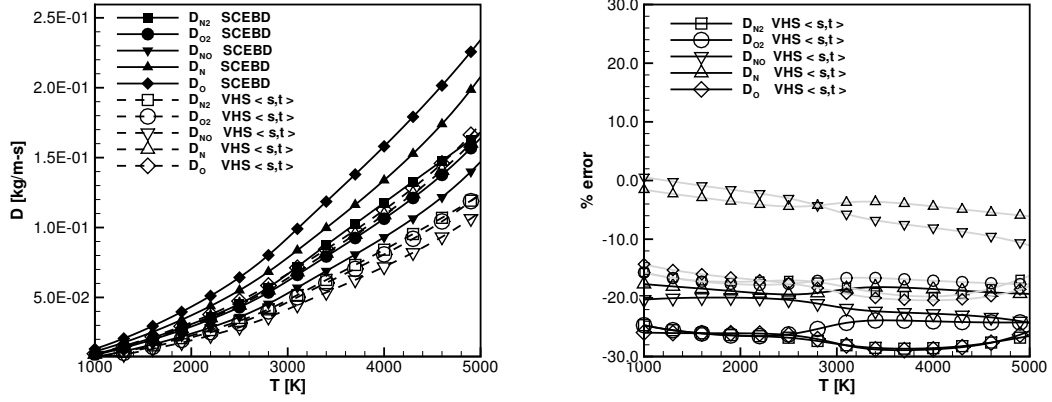
(d) Thermal conductivity coefficients.

Figure 4.1: (a) Five-species air mixture composition by mole fraction χ_s as a function of temperature, ranging from $1000K$ to $5000K$, at $2300Pa$. (b) Effective diffusion coefficients for five-species air gas mixture as a function of temperature. (c) Viscosity coefficient for five-species air gas mixture as a function of temperature. (d) Translational, rotational and vibrational thermal conductivity coefficients for five-species air gas mixture as a function of temperature.

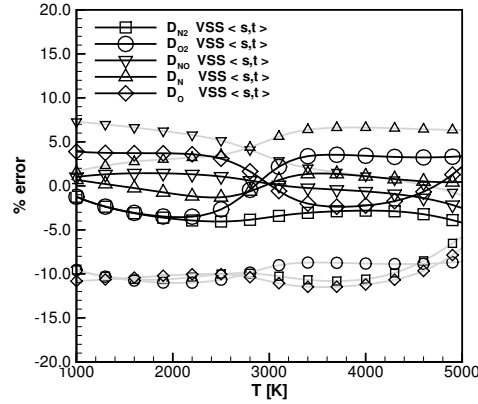
4.4.2 Collision-Averaged Best-Fit Parameters: VHS/VSS Collision Models

The transport coefficients predicted by the SCEBD and Gupta *et al.*-Yos transport models are presented in Figures 4.2(a)-4.4(a). The corresponding transport coefficients generated from the best-fit VHS collision-averaged parameter set are plotted in these figures for comparison. The error presented in Figures 4.2(b)-4.4(b) and Figures 4.2(c)-4.4(c) represents the difference in the VHS/VSS transport coefficients and the SCEBD/Gupta *et al.*-Yos transport coefficients, normalized by the SCEBD/Gupta *et al.*-Yos transport coefficient value and presented as a percentage. Regarding error figures throughout the paper, the error in the VHS/VSS transport coefficients relative to the SCEBD/Gupta *et al.*-Yos values shown in the black line plots represent the error resulting from the transport coefficient fitting approach, while the gray line plots represent the error resulting from the collision integral fitting approach. In this first set, the effective binary diffusion, viscosity and thermal conductivities are computed according to the best-fit parameters from the VHS/VSS *collision-averaged* pairing approach (denoted as VHS $\langle s, t \rangle$ and VSS $\langle s, t \rangle$), in which the parameters considered in the fit include five reference diameters, d_{ref} , five temperature exponents, ω and, for VSS, five scattering exponents α .

The recommended best-fit parameters generated from transport coefficient fits are provided in Table 4.1. The number of significant figures reported in values are dictated by the sensitivity of these fitted values to the initial

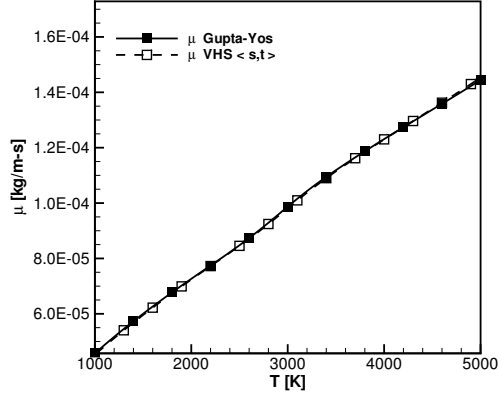


(a) Effective binary diffusion coefficients (b) Percent error VHS $\langle s, t \rangle$ relative to SCEBD

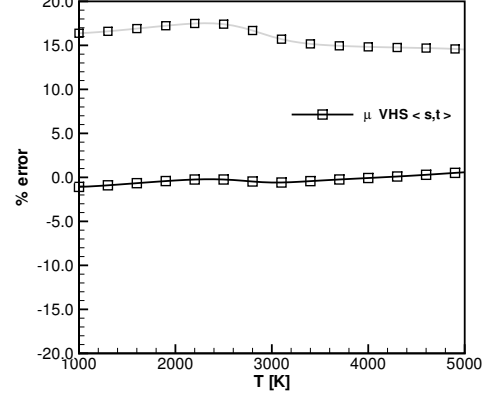


(c) Percent error VSS $\langle s, t \rangle$ relative to SCEBD

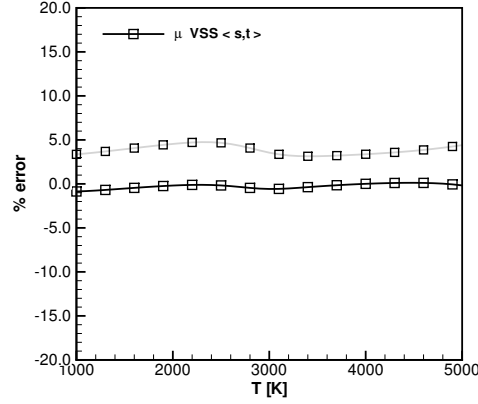
Figure 4.2: (a) Comparison of effective binary diffusion coefficients for five-species air, computed from fitted VHS collision-averaged pairing approach (dashed lines with open symbols) and SCEBD model (solid lines with closed symbols). Percent error of fitted VHS (b) and fitted VSS (c) collision-averaged effective diffusion coefficients relative to SCEBD model. In (b) and (c), black lines represent error using transport coefficient fits, while gray lines represent error using collision integral fits.



(a) Viscosity coefficient

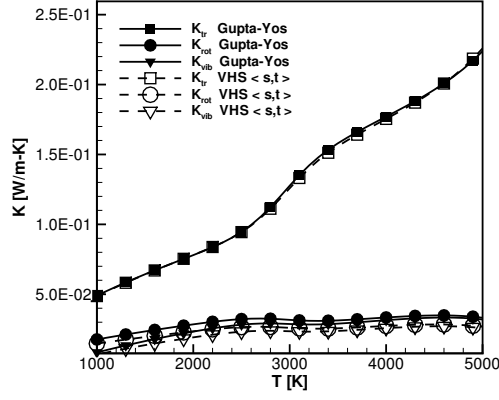


(b) Percent error VHS $< s, t >$ relative to Gupta *et al.*-Yos

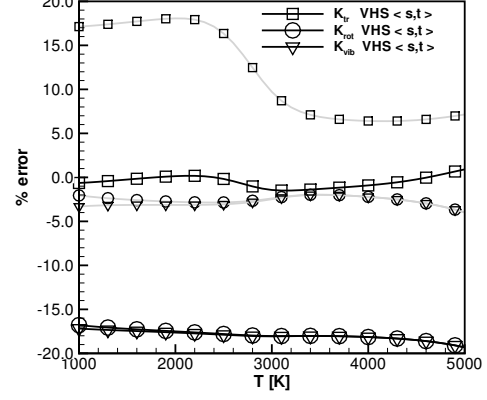


(c) Percent error VSS $< s, t >$ relative to Gupta *et al.*-Yos

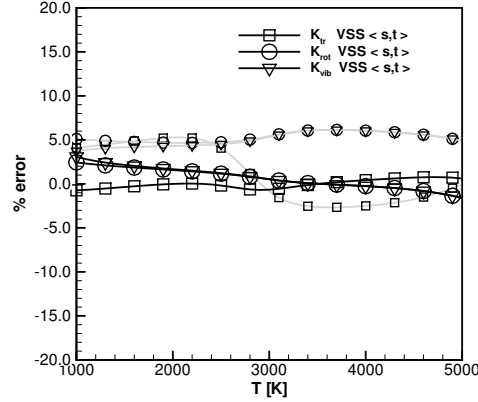
Figure 4.3: (a) Comparison of viscosity coefficient for five-species air, computed from fitted VHS collision-averaged pairing approach (dashed line with open symbols) and Gupta *et al.*-Yos model (solid line with closed symbols). Percent error of fitted VHS (b) and fitted VSS (c) collision-averaged viscosity coefficient relative to Gupta *et al.*-Yos model. In (b) and (c), black lines represent error using transport coefficient fits, while gray lines represent error using collision integral fits.



(a) Thermal conductivity coefficients



(b) Percent error VHS $< s, t >$ relative to Gupta *et al.*-Yos



(c) Percent error VSS $< s, t >$ relative to Gupta *et al.*-Yos

Figure 4.4: (a) Comparison of thermal conductivity coefficients for five-species air, computed from fitted VHS collision-averaged pairing approach (dashed lines with open symbols) and Gupta *et al.*-Yos model (solid lines with closed symbols). Percent error of fitted VHS (b) and fitted VSS (c) collision-averaged thermal conductivity coefficients relative to Gupta *et al.*-Yos model. In (b) and (c), black lines represent error using transport coefficient fits, while gray lines represent error using collision integral fits.

Table 4.1: Collision-Averaged VHS/VSS Parameters (Fits to Transport Coefficients)

VHS	$d_{ref}[\text{\AA}]$	ω	VSS	$d_{ref}[\text{\AA}]$	ω	α
N_2	3.20	0.68	N_2	3.20	0.68	1.348
O_2	2.80	0.68	O_2	2.60	0.68	1.547
NO	3.30	0.76	NO	3.30	0.76	1.62
N	2.60	0.70	N	2.70	0.70	1.608
O	2.32	0.76	O	2.20	0.76	1.90

parameter guesses used in the search algorithm (Appendix D). Note that the VSS reference diameter values for N and O were relaxed slightly from the VHS values.

The effective binary diffusion coefficients are presented in Figure 4.2(a) as a function of temperature, and the corresponding error of the fitted VHS and VSS effective diffusion coefficients relative to the SCEBD model are also provided (Figure 4.2(b) and Figure 4.2(c), respectively). The error in the diffusion coefficients from the VHS model approach nearly 30% using the transport coefficient fits. Keep in mind that the VHS parameters are only calibrated for coefficients of viscosity and translational thermal conductivity, while the calibration of the VSS parameters includes the diffusion-driven coefficients. The VSS model shows a substantial improvement in the modeling of the diffusivities over the VHS model, as evident by the overall decrease in percent error shown in Figure 4.2(c) relative to Figure 4.2(b). The effective binary diffusion coefficients match the SCEBD values to within 5% over the entire range of temperatures considered.

The mixture viscosity (Figure 4.3(a)) and thermal conductivities (Figure 4.4(a)) are also plotted as a function of temperature. Again, the error corresponding to the fitted VHS and VSS collision models are presented in Figures 4.3(b)-4.4(b) and Figures 4.3(c)-4.4(c), respectively. The viscosity and translational thermal conductivity computed by the best-fit VHS parameters (Figures 4.3(b), 4.4(b)) provide excellent agreement to the first principles calculations. The internal thermal conductivities, however, are in error of nearly 20%. The viscosity and thermal conductivity coefficients computed by the best-fit VSS collision-averaged parameters lie within 3-4% of the Gupta *et al.*-Yos values (Figures 4.3(c), 4.4(c)), including the internal thermal conductivities. Note that the VSS transport coefficient fits provides significant improvement over the collision integral fits (shown by gray lines in Figures 4.2(c)-4.4(c)).

In all of the cases presented here, the best-fit VHS/VSS collision model parameters were determined by assuming that all transport coefficients are weighted equally over the range of temperatures. It should also be noted that each effective binary diffusion coefficient (D_{N_2} , D_{O_2} , etc.) and each thermal conductivity coefficient (K_{tr} , K_{rot} , etc.) is considered as an individual transport coefficient, and these are weighted equally. Thus, the fitting process effectively involves determining the collision model parameters which yield the best fit across a total of nine transport coefficients (five effective diffusion coefficients, one viscosity coefficient and three thermal conductivity coefficients). Note that alternative weighting approaches could easily be applied in order to

produce a balance across the fitting of all types or classes of transport (mass, momentum and energy); alternatively, one could produce a bias on the fitting of a particular transport property. To achieve the former for the cases presented here, it would be necessary to specify a weight of one-fifth on each of the diffusion coefficients, a weight of unity on the coefficient of viscosity, and a weight of one-third on each of the thermal conductivity coefficients. In a similar way, a bias would be achieved by assigning a larger weight to the desired transport coefficient(s) such that more importance is placed on the fitting of the particular quantity.

4.4.3 Collision-Specific Best-Fit Parameters: VHS/VSS Collision Models

In the next set of cases presented, the VHS/VSS transport coefficients are fit to the SCEBD/Gupta *et al.*-Yos transport coefficients using the *collision-specific* pairing approach for determination of the VHS/VSS collision model parameters (denoted as VHS s, t and VSS s, t). The transport coefficients predicted by the SCEBD and Gupta *et al.*-Yos transport models are again presented as a function of temperature in Figures 4.5(a)-4.7(a). The corresponding transport coefficients generated from the best-fit VHS collision-specific parameter set are plotted in these figures for comparison.

The errors in the transport coefficients generated from the best-fit VHS/VSS parameters relative to the SCEBD/Gupta *et al.*-Yos coefficients are presented in Figures 4.5(b)-4.7(b) and Figures 4.5(c)-4.7(c), respectively.

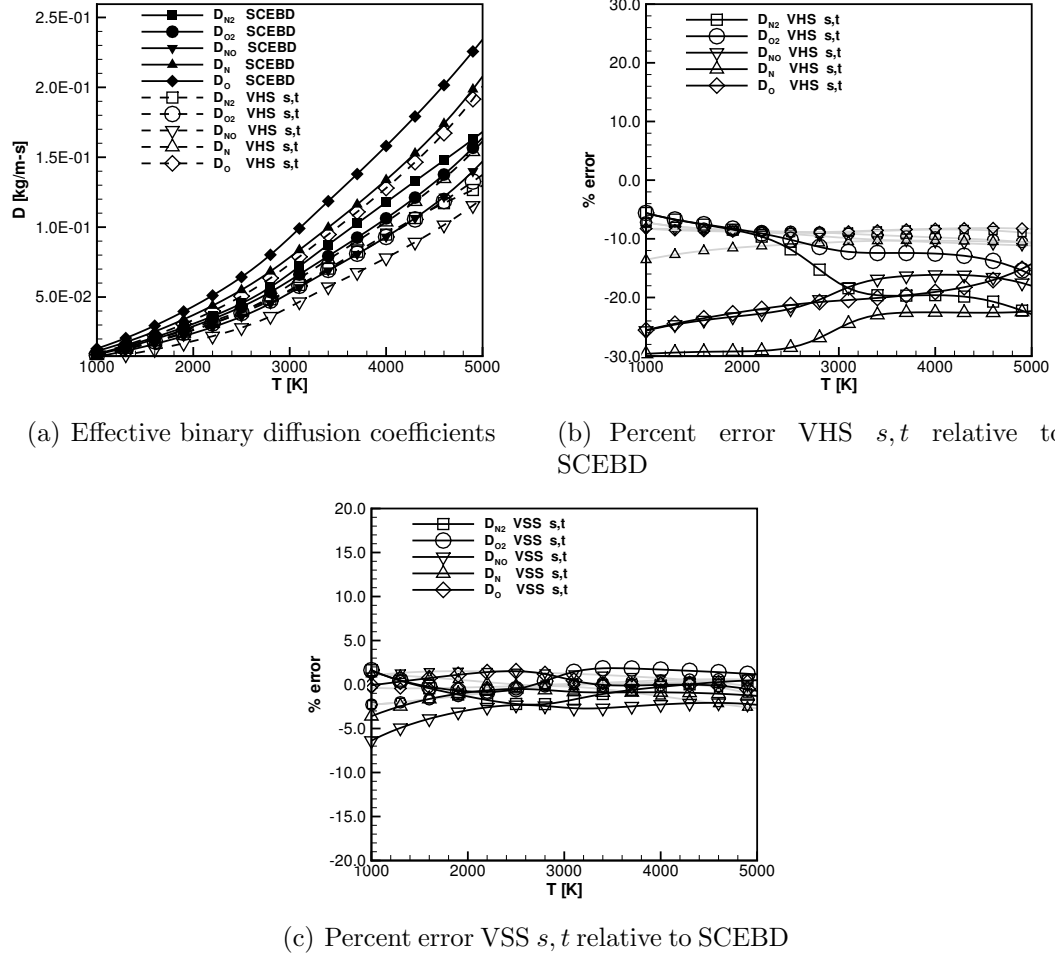
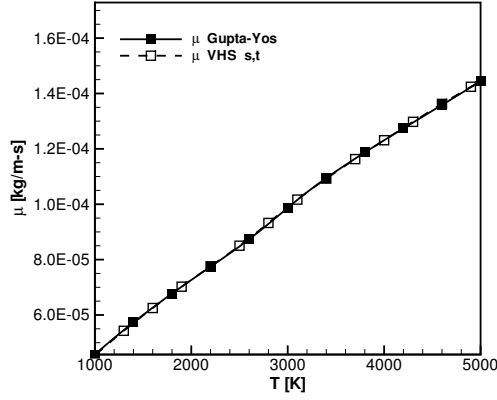
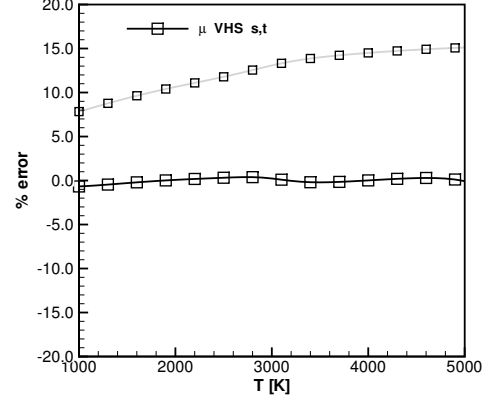


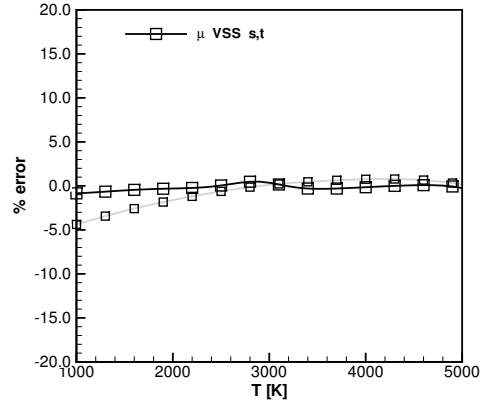
Figure 4.5: (a) Comparison of effective binary diffusion coefficients for five-species air, computed from fitted VHS collision-specific pairing approach (dashed lines with open symbols) and SCEBD model (solid lines with closed symbols). Percent error of fitted VHS (b) and fitted VSS (c) collision-specific effective diffusion coefficients relative to SCEBD model. In (b) and (c), black lines represent error using transport coefficient fits, while gray lines represent error using collision integral fits.



(a) Viscosity coefficient

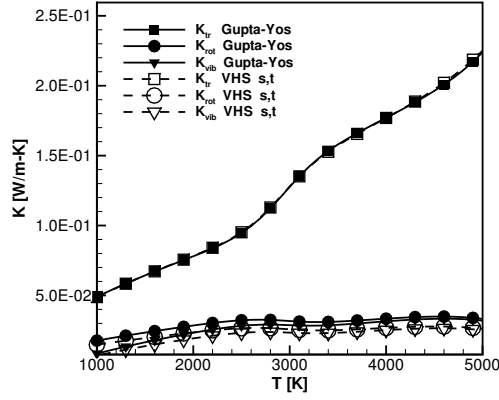


(b) Percent error VHS s, t relative to Gupta *et al.*-Yos

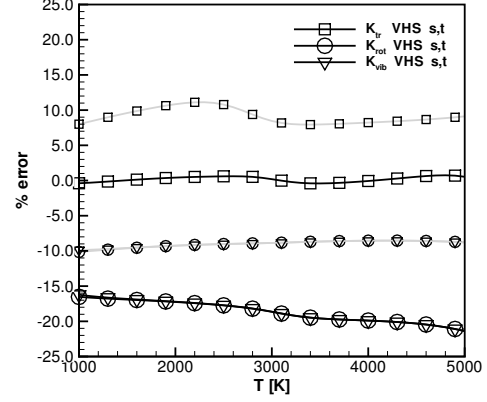


(c) Percent error VSS s, t relative to Gupta *et al.*-Yos

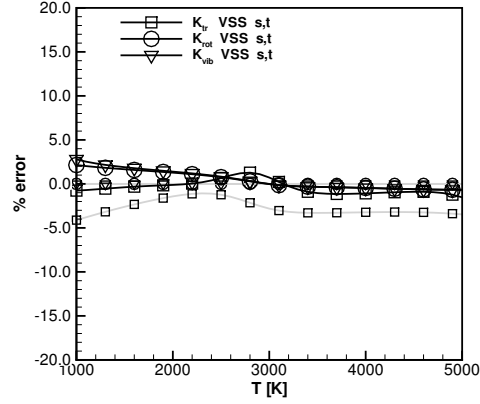
Figure 4.6: (a) Comparison of viscosity coefficient for five-species air, computed from fitted VHS collision-specific pairing approach (dashed line with open symbols) and Gupta *et al.*-Yos model (solid line with closed symbols). Percent error of fitted VHS (b) and fitted VSS (c) collision-specific viscosity coefficients relative to Gupta *et al.*-Yos model. In (b) and (c), black lines represent error using transport coefficient fits, while gray lines represent error using collision integral fits.



(a) Thermal conductivity coefficients



(b) Percent error VHS s, t relative to Gupta *et al.*-Yos



(c) Percent error VSS s, t relative to Gupta *et al.*-Yos

Figure 4.7: (a) Comparison of thermal conductivity coefficients for five-species air, computed from fitted VHS collision-specific pairing approach (dashed lines with open symbols) and Gupta *et al.*-Yos model (solid lines with closed symbols). Percent error of fitted VHS (b) and fitted VSS (c) collision-specific thermal conductivity coefficients relative to Gupta *et al.*-Yos model. In (b) and (c), black lines represent error using transport coefficient fits, while gray lines represent error using collision integral fits.

The parameters considered in this fit include fifteen reference diameters, d_{ref} , fifteen temperature exponents, ω , and, for VSS, fifteen scattering exponents, α . A direct comparison of these fits to those obtained using the *collision-averaged* pairing approach in Figures 4.2-4.4 indicates that the collision-specific pairing has only a small influence on the quality of agreement between the transport coefficients computed from the VHS/VSS models and the first principles calculations. The most significant improvement in the results are obtained when using the appropriate model (VSS) in the fitting, rather than simply using more adjustable parameters with an insufficient model (e.g., VHS with collision-specific pairing).

The recommended best-fit VHS/VSS parameters corresponding to this collision pairing are given in Table 4.2. Again, the number of significant figures reported in values are dictated by the sensitivity of these fitted values to the initial parameter guesses used in the search algorithm (see example in Appendix D). Also note that several of the VSS reference diameters and temperature exponent values were relaxed from the VHS values to provide the best fit across the transport coefficients. The VHS effective diffusion coefficients again show errors of up to 30% using the collision-specific pairing (Figure 4.5(b)). The VSS collision-specific pairing produce errors of approximately 5% at the lower temperature range (Figure 4.5(c)), but the error is measurably reduced at higher temperatures relative to the collision-averaged pairing. The error of the VHS/VSS mixture viscosity coefficients relative to the Gupta *et al.*-Yos values are shown in Figure 4.6(b) and Figure 4.6(c), re-

Table 4.2: Collision-Specific VHS/VSS Parameters (Fits to Transport Coefficients)

VHS						VSS					
$d_{ref}[\text{\AA}]$	N_2	O_2	NO	N	O	$d_{ref}[\text{\AA}]$	N_2	O_2	NO	N	O
N_2	3.31	2.68	3.24	3.10	2.66	N_2	3.25	2.77	3.64	2.90	2.50
O_2		3.41	3.46	2.95	2.72	O_2		2.90	3.01	2.60	2.36
NO			3.12	3.02	2.61	NO			2.80	2.82	2.70
N				3.20	2.31	N				3.00	2.70
O					2.61	O					2.75
ω	N_2	O_2	NO	N	O	ω	N_2	O_2	NO	N	O
N_2	0.68	0.68	0.78	0.72	0.78	N_2	0.68	0.68	0.78	0.76	0.73
O_2		0.70	0.70	0.72	0.78	O_2		0.70	0.70	0.72	0.78
NO			0.72	0.75	0.77	NO			0.72	0.75	0.77
N				0.76	0.75	N				0.76	0.75
O					0.74	O					0.74
α	N_2	O_2	NO	N	O	α	N_2	O_2	NO	N	O
N_2						N_2	1.4	1.30	1.9	1.4	1.29
O_2						O_2		1.8	1.8	1.3	1.1
NO						NO			1.3	1.4	1.6
N						N				1.2	1.5
O						O					1.2

spectively. The errors from the VHS and VSS collision-averaged and collision-specific fits of the viscosity are nearly equivalent, although the values predicted from the collision integral fits (in gray lines) show improvement by using the collision-specific pairing. The thermal conductivity coefficients from the VHS collision-specific pairing and the Gupta *et al.*-Yos values are plotted in Figure 4.7(a) as a function of temperature, and the corresponding errors of the VHS/VSS collision-specific values relative to the Gupta *et al.*-Yos coefficients are also shown in Figure 4.7(b) and Figure 4.7(c). The errors in the fit of the

translational and internal thermal conductivities are equivalent to the VHS and VSS collision-averaged errors.

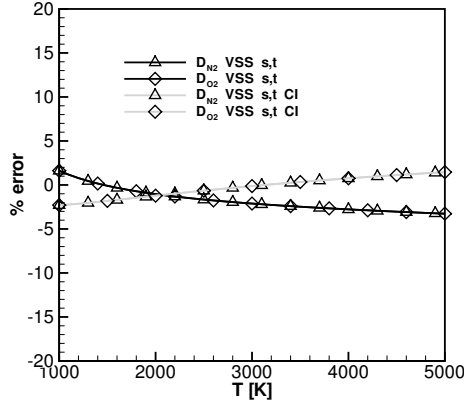
This pairing approach provides forty-five total parameters in the Nelder-Mead algorithm, fifteen of which are free parameters, and thirty which are bounded. By comparison of the fits in the effective diffusion, viscosity and thermal conductivity coefficients obtained using the previous VHS/VSS collision pairing approaches, it can be concluded that the VSS collision-specific pairing approach achieves the best overall match to the SCEBD and Gupta *et al.*-Yos transport models. The errors in the effective diffusion coefficients, mixture viscosity and thermal conductivities in Figures 4.2(c)-4.7(c) are all less than $\pm 5\%$ over the range of temperatures considered.

4.4.4 Extension to Chemical Non-equilibrium

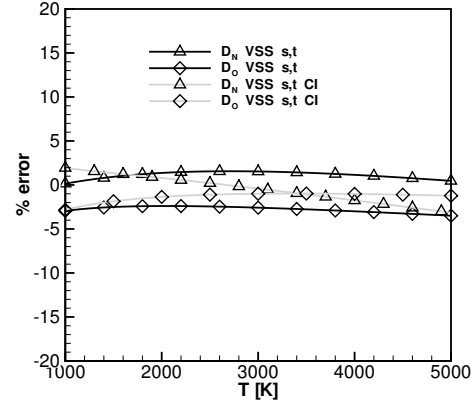
The cases presented above provide a comparison of the VHS and VSS collision models in their representation of the transport coefficients for an equilibrium five species air mixture over a temperature range of $1000K$ to $5000K$. The fitted parameter values were determined as the parameters which minimize the difference in the transport coefficients over a range of temperatures, and are referred to as transport coefficient fits. It should be emphasized that since the transport coefficients were used as the fitting metric, this approach required knowledge of the (equilibrium) mixture composition. In order to examine the applicability of these recommended parameter values in non-equilibrium cases, we use the fitted values determined from the transport coefficient fits to com-

pute the transport coefficients in three non-equilibrium compositions. These cases correspond to fully dissociated (79% N and 21% O by mole fraction) air mixture, fully recombined (79% N_2 and 21% O_2 by mole fraction) air mixture, and an intermediate (70% N_2 , 15% O_2 , 10% NO and 5% N by mole fraction) non-equilibrium air mixture over the temperature range examined. For brevity, only the results from the VSS model with *collision-specific* pairing are presented in these non-equilibrium cases, as the fits from the VHS model were found to be relatively poor. The transport coefficients determined from the collision integral fitting approach (outlined in Section 4.3.2), are also presented for comparison.

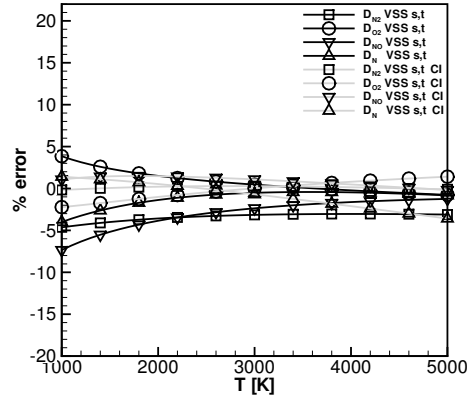
The first coefficients presented are the effective binary diffusion coefficients for the fully recombined, fully dissociated and intermediate cases. The percent error of these diffusion coefficients relative to the corresponding SCEBD values is presented in Figure 4.8(a-c), represented by black lines with symbols. The percent error of the diffusion coefficients computed from the best fit *collision integral* approach relative to the corresponding SCEBD values are also shown for comparison (gray lines with symbols). In the fully recombined case, the diffusion coefficients from the transport coefficient fits (black lines) and the collision integral fits (gray lines) provide agreement to the SCEBD model to within 3% across the range of temperatures considered, respectively. When these fitted parameter values are used in the fully dissociated gas mixture, it is observed (Figure 4.8(b)) that the error in the diffusion coefficients from both fitting approaches remains less than 4% over the temper-



(a) fully recombined air (N_2, O_2)

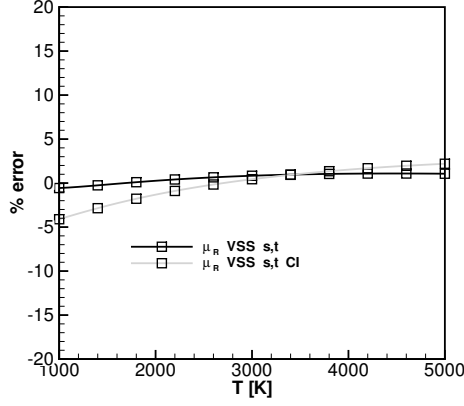


(b) fully dissociated air (N, O)

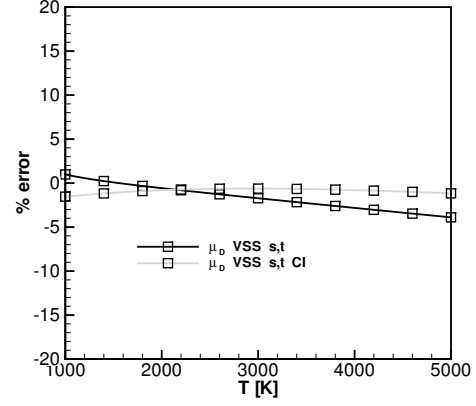


(c) intermediate non-equilibrium air
(N_2, O_2, NO, N)

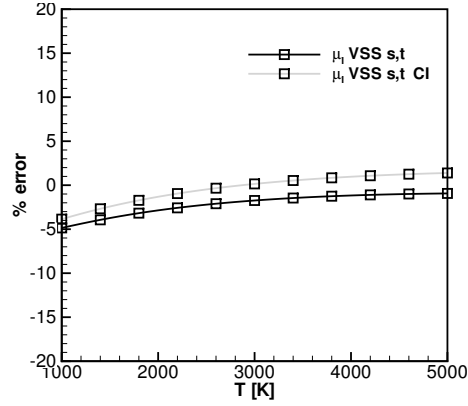
Figure 4.8: Percent error of fitted VSS collision-specific effective binary diffusion coefficients relative to SCEBD model for (a) fully recombined air, (b) fully dissociated air and (c) intermediate chemical non-equilibrium conditions. Black lines represent error using transport coefficient fitted parameters (from equilibrium composition), while gray lines represent error using collision integral fits.



(a) fully recombined air (N_2, O_2)



(b) fully dissociated air (N, O)



(c) intermediate non-equilibrium air
(N_2, O_2, NO, N)

Figure 4.9: Percent error of fitted VSS collision-specific viscosity coefficients relative to Gupta *et al.*-Yos model for (a) fully recombined air, (b) fully dissociated air and (c) intermediate chemical non-equilibrium conditions. Black lines represent error using transport coefficient fitted parameters (from equilibrium composition), while gray lines represent error using collision integral fits.

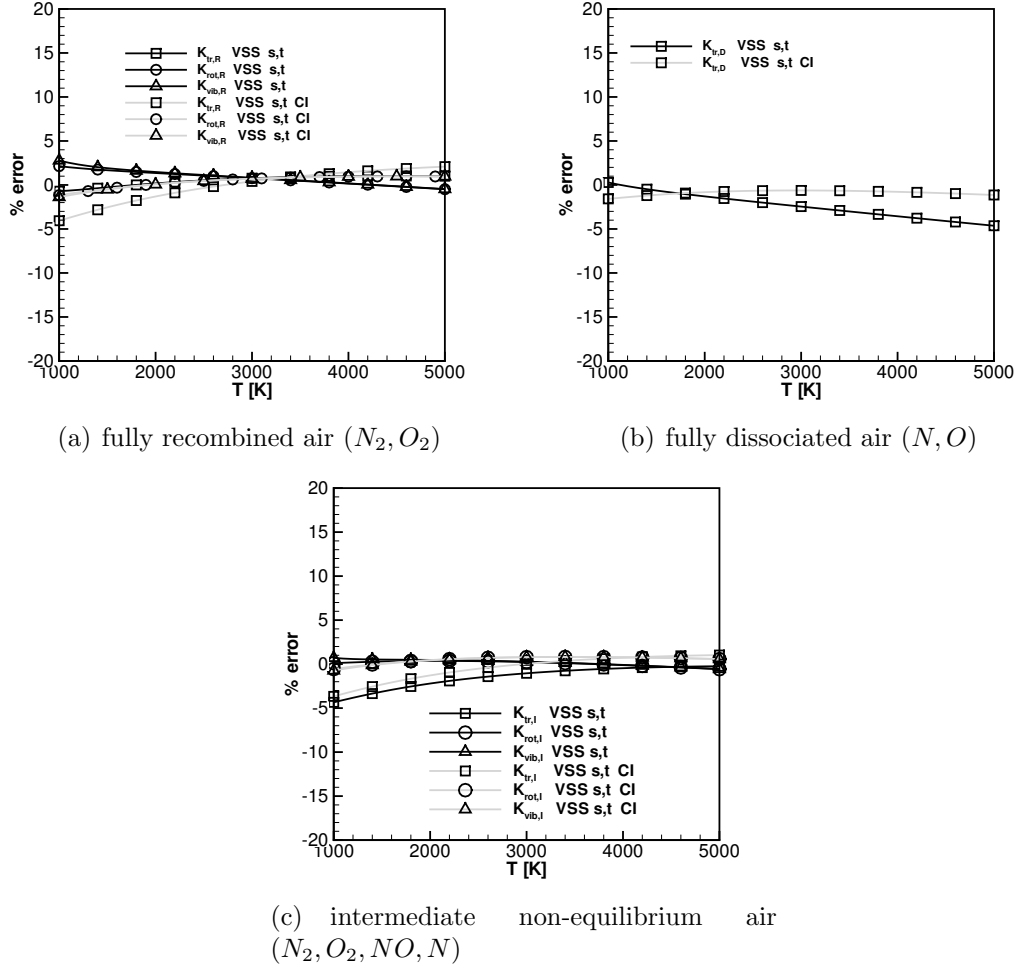


Figure 4.10: Percent error of fitted VSS collision-specific thermal conductivity coefficients relative to Gupta *et al.*-Yos model for (a) fully recombined air, (b) fully dissociated air and (c) intermediate chemical non-equilibrium conditions. Black lines represent error using transport coefficient fitted parameters (from equilibrium composition), while gray lines represent error using collision integral fits.

Table 4.3: Collision-Averaged/Collision-Specific VSS Parameters (Fits to Collision Integrals)

VSS				VSS					
	$d_{ref}[\text{\AA}]$	ω	α	$d_{ref}[\text{\AA}]$	N_2	O_2	NO	N	O
N_2	3.02	0.68	1.33	N_2	3.26	2.84	3.19	2.88	2.54
O_2	2.94	0.70	1.43	O_2		3.17	3.15	2.69	2.71
NO	3.10	0.71	1.46	NO			3.19	2.75	2.76
N	2.61	0.78	1.50	N				2.53	2.59
O	2.46	0.78	1.54	O					2.41
				ω	N_2	O_2	NO	N	O
				N_2	0.69	0.73	0.72	0.69	0.71
				O_2		0.76	0.74	0.75	0.74
				NO			0.74	0.73	0.75
				N				0.73	0.72
				O					0.70
				α	N_2	O_2	NO	N	O
				N_2	1.42	1.39	1.48	1.45	1.41
				O_2		1.53	1.51	1.42	1.48
				NO			1.55	1.46	1.62
				N				1.38	1.51
				O					1.36

ature range. The error from the transport coefficient fits in the intermediate non-equilibrium air mixture becomes measurably worse at lower temperatures, with errors up to 8% (Figure 4.8(c)). In comparison, the collision integrals fits in this case provide excellent agreement to the Gupta *et al.*-Yos values, with errors of less than 4% over the temperature range.

Figures 4.9 and 4.10 show the percent error of the mixture viscosity and the thermal conductivities, respectively, relative to the Gupta *et al.*-Yos model for the non-equilibrium cases considered. Again, black lines and sym-

bols represent the errors in transport coefficients computed using parameters from transport coefficient fits, while gray lines and symbols represent the errors in coefficients using parameters from collision integral fits. The mixture viscosity fits using both transport coefficient fits and collision integral fits are very good for the fully recombined case (Figure 4.9(a)), fully dissociated case (Figure 4.9(b)), as well as for the intermediate case (Figure 4.9(c)). Similar results are found for the thermal conductivity fits using both transport coefficient fits and collision integral fits shown in Figures 4.10(a-c), with errors less than 5% over the range of temperatures examined. In all of the cases examined in this work, it is found that the collision integral fits using the VSS collision model with *collision-specific* parameter pairing consistently provides the best fits to the SCEBD and Gupta *et al.*-Yos coefficients. This is true regardless of the state of the gas mixture composition, i.e. chemical equilibrium (Figures 4.5(c)-4.7(c)) vs. non-equilibrium (Figures 4.8(c)-4.10(c)), as the errors from the collision integral fits in all conditions examined are less than 5%. The values for the VSS *collision-specific* parameters determined from the collision-integral fits are provided in Table 4.3, and are recommended for use in any non-ionized gas mixture.

The collision integral fits using the VSS collision model with *collision-averaged* parameter pairing (also tabulated in Table 4.3) achieve reasonable agreement with the SCEBD and Gupta *et al.*-Yos coefficients (presented for the chemical equilibrium gas mixture in Section 4.4.2), but the error in the diffusion coefficients increases to nearly 10%. While this error may be ac-

ceptable for certain applications, it was found in Section 4.4.2 that the results produced from the transport coefficient fitted parameters demonstrated better overall agreement with the SCEBD and Gupta *et al.*-Yos coefficients. This is due to the fact that the composition ‘informs’ the fitting process through the expressions for the transport coefficients. Thus, in cases where the composition is close to chemical equilibrium and *collision-averaged* pairing is required, the VSS parameters provided in Table 4.1 may be used. However, in cases where the composition is far from equilibrium, the best fit VSS *collision-specific* parameters (based on collision integral fits) provided in Table 4.3 should be used.

4.5 Summary

A general approach for achieving consistency in the species diffusion, viscosity and thermal conductivity coefficients between the phenomenological VHS/VSS collision cross section models and the SCEBD/Gupta *et al.*-Yos models was presented for five-species air. The DSMC transport coefficients were approximated from the SCEBD model (diffusion), Chapman-Enskog theory (viscosity and translational thermal conductivity) and Eucken’s relation (internal thermal conductivities), and the corresponding collision integrals were determined according to the VHS or VSS collision cross section model. The transport coefficients from the SCEBD and Gupta *et al.*-Yos models were generated using collision integrals computed from more realistic intermolecular potentials. These transport coefficients were considered as the ‘standard’

values to which the DSMC transport coefficients were fitted by selectively adjusting the VHS/VSS parameters using the Nelder-Mead Simplex Method. The temperatures considered in this work ranged from 1000 K - 5000 K at a pressure of 2300 Pa , and chemical equilibrium and non-equilibrium cases were examined. These results were also compared to fits generated using the collision integral fitting approach.

The transport coefficients generated from the best-fit VHS model parameters were found to be in relatively poor agreement with the SCEBD and Gupta *et al.*-Yos values compared to the VSS model, regardless of the collision pairing approach used. This underscores the importance of using the VSS model for flows involving gas mixtures, as the scattering exponent α allows for a consistent representation of both the viscosity and diffusion cross sections. In cases where diffusion is not expected to dominate the flow and the use of the VHS model is desired, the VHS model parameters can be calibrated to give excellent agreement to the viscosity and translational thermal conductivities for this gas mixture. In this situation, quantities such as shear stress or Fourier-type heat flux would be of interest. However, the VSS model should be used for conditions in which species diffusion is important, such as flows involving strong normal shocks or chemical reactions/reacting surfaces.

The best fit parameters generated from the transport coefficient fits in a chemical equilibrium mixture were extended to examine the quality of agreement in transport coefficients for three non-equilibrium cases. It was found that the parameters obtained from the collision integral fits using the

VSS *collision-specific* pairing approach provide best agreement to the SCEBD and Gupta *et al.*-Yos coefficients for the mixtures examined (both equilibrium and non-equilibrium compositions), compared to the transport coefficient fitted parameters. The VSS *collision-averaged* fitted parameters obtained from collision integral fits were shown in the equilibrium composition case to provide reasonable agreement (within 10%) to SCEBD and Gupta *et al.*-Yos, but better results are obtained using the fitted parameters from the transport coefficient fits. Again, this is due to the fact that the transport coefficient fits make use of the mixture composition to inform the fitting process.

Chapter 5

Application to Hypersonic Boundary Layer Flow Over Discrete Surface Roughness

5.1 Overview

In this chapter, the concepts of the hybrid framework and techniques discussed in Chapters 2-4 are brought together and applied to model hypersonic boundary layer flow over discrete surface roughness. In particular, the hybrid approach is used to provide a detailed non-equilibrium solution in the region surrounding the roughness as well as in the near wake region. The flow conditions examined in this work are presented first, and the convergence requirements of both the CFD and DSMC solvers are discussed for the cases presented. The three-dimensional flowfield results are divided into two parts. The asymmetric geometry configuration is presented first, and results from low and high altitude conditions are examined and compared among the CFD no-slip, slip and hybrid DSMC solutions. The symmetric geometry configuration is presented next, and results from the high altitude condition are compared among the CFD no-slip, slip and hybrid DSMC solutions. This chapter concludes with an assessment of the computational performance of the hybrid DSMC and CFD solvers and a summary of the key findings from these investigations.

5.2 Hybrid and CFD Solutions

5.2.1 Flow Conditions and Roughness Geometries

The flow conditions that are used in this hybrid analysis are representative of the hypersonic boundary layer flow conditions for an ISS return trajectory of the shuttle Orbiter. The ISS descent trajectory (represented by the green trajectory in Figure 5.1) indicates a maximum Mach number of approximately $M_\infty = 28$ early in the trajectory, and the freestream Mach number has decreased to approximately $M_\infty = 13$ at an altitude of 50 *km*. The post-flight analysis from the STS-119 BLT flight experiment indicated transition onset due to the protuberance at $M_\infty = 15$ and an altitude of approximately 54 *km*. The protuberance in this experiment had a roughness height of $k = 6.35 \times 10^{-3}$ *m*, which was approximately one-quarter of the boundary layer thickness at transition. From CFD analysis, the molecular mean free path at the boundary layer edge was $O(10^{-5})$, and the Knudsen number based on roughness height Kn_k was $O(10^{-3})$.

Due to the considerable computational expense of a fully resolved hybrid solution for this particular trajectory point, the results presented in this work examine two conditions at higher altitudes along the trajectory. The first set of conditions examined correspond to a freestream Mach number of $M_\infty = 20$ at an altitude of approximately 60 *km*, which is referred to as the low altitude case. The second set of conditions correspond to a freestream Mach number of $M_\infty = 25$ at an altitude of approximately 80 *km* (herein referred to as the high altitude case). The location of these points on the trajectory

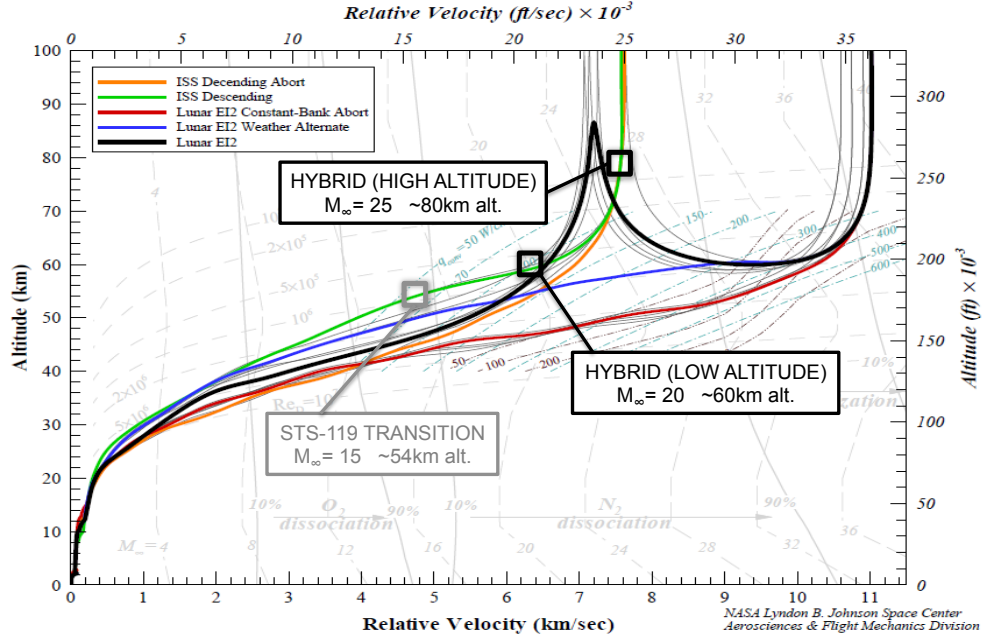


Figure 5.1: ISS/lunar descent trajectories. The conditions examined in this work correspond to freestream Mach numbers of $M_\infty = 20$ (60 km low altitude case) and $M_\infty = 25$ (80 km high altitude case). Transition onset due to the protuberance in the STS-119 flight experiment occurred at approximately $M_\infty = 15$.

relative to the STS-119 transition location are represented schematically in Figure 5.1.

The protuberance in the STS-119 BLT flight experiments was positioned on the shuttle Orbiter belly at a location approximately 25 m downstream of the Orbiter nose and 6 m off of the centerline. This location was used as the reference point to extract the boundary layer edge conditions for the high and low altitude conditions presented here. The set-up of the

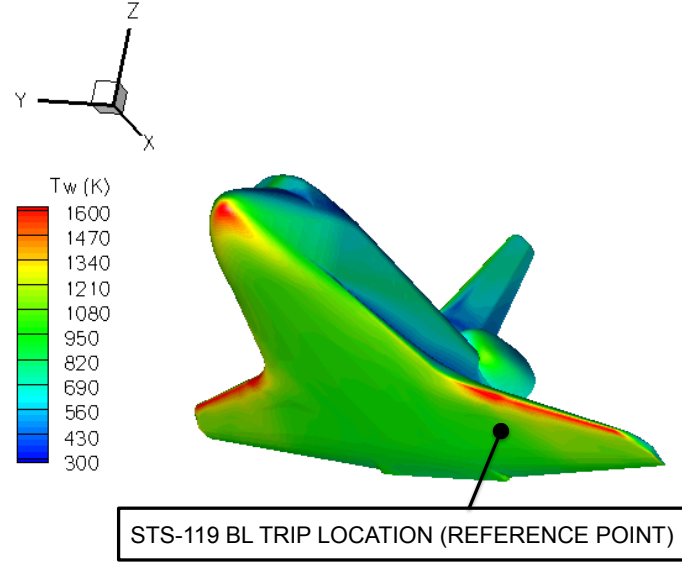


Figure 5.2: Shuttle Orbiter with reference point of STS-119 BLT boundary layer trip location. Contours represent local wall temperature [K] for smooth OML solution generated with DPLR (obtained from NASA Ames [64]).

three-dimensional flowfields examined in this work is a simple flat plate with a discrete surface roughness element located at a fixed distance x_k downstream of the leading edge. The CFD solutions were generated first in multiple stages. The boundary layer edge conditions pertaining to the 60 *km* and 80 *km* cases were first obtained from full CFD flowfield solutions generated for a smooth outer mold line (OML) of the shuttle Orbiter at the corresponding freestream conditions (Figure 5.2). These solutions were computed with DPLR and were provided by NASA Ames [64].

In the next step, a two-dimensional flat plate boundary layer solution is generated using DPLR in which the boundary layer edge conditions are

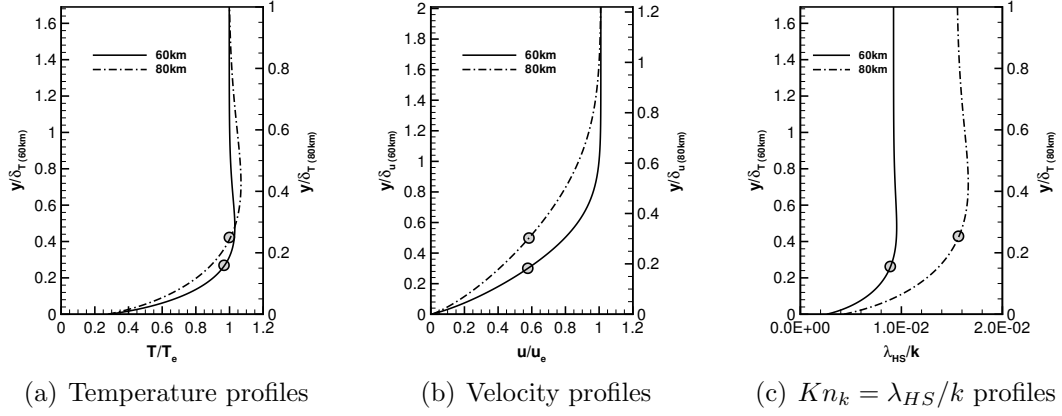


Figure 5.3: Two-dimensional flat plate boundary layer profiles generated from DPLR, based on edge conditions at STS-119 reference point (see Figure 5.2) at 60 km and 80 km. Profiles show (a) translational temperature, (b) streamwise velocity and (c) Knudsen number based on roughness height k . Circle symbols on each profile represent height of discrete roughness examined for each case.

specified according to the OML solutions at the STS-119 reference point. The boundary layer edge conditions corresponding to the low and high altitude cases examined are tabulated in Table E.1, and solutions are provided in Figure 5.3. The wall temperature in these cases was prescribed as $T_w = 1200\text{ K}$, which is equivalent to the radiative equilibrium wall temperature from the STS-119 solution. All profiles in Figures 5.3(a)-(c) were acquired at the location of the roughness center x_k in an *undisturbed* flat plate boundary layer. The profiles are provided up to $y = 0.05\text{ m}$ (where the wall is located at $y = 0\text{ m}$), which corresponds to the thermal boundary layer thickness of the high altitude case.

Profiles of the translational temperature for the low altitude (60 km) and high altitude (80 km) cases are presented in Figure 5.3(a). The profiles show the normalized translational temperature through the boundary

Table 5.1: Boundary layer edge conditions

	Low altitude (60km)	High altitude (80km)
M_e	2.96	3.0
p_e	2400 Pa	900 Pa
u_e	4400 m/s	5000 m/s
T_e	4500 K	5100 K
λ_e	4.2×10^{-5}	1.3×10^{-4}
Re_x	9.4×10^4	2.9×10^4
Re_k	3.42×10^2	1.80×10^2
χ_{N2}	6.072×10^{-1}	4.5838×10^{-1}
χ_{O2}	2.0×10^{-4}	2.0×10^{-5}
χ_{NO}	4.6×10^{-3}	1.6×10^{-3}
χ_N	4.8×10^{-2}	2.4×10^{-1}
χ_O	3.4×10^{-1}	3.0×10^{-1}

layer, and are plotted as a function of wall-normal distance normalized by the corresponding thermal boundary layer thickness. In the case of the thermal boundary layer, the temperature slightly overshoots the edge value, and so the boundary layer thickness δ_T is taken as the first wall-normal location where $T_{tr} = 1.01T_{tr,\infty}$ approaching the wall. The thermal boundary layer thickness in the low altitude case is approximately 60% of the high altitude case at the same x -location. Profiles of streamwise velocity normalized by the edge velocity are given in Figure 5.3(b). Regarding Figure 5.3(b), the boundary layer thickness based on velocity δ_u is taken as the location where $u = 0.99u_\infty$ as usual. The boundary layer thicknesses δ_u at both low and high altitudes are approximately 20% less than the thermal boundary layer thickness. In Figure 5.3(c), the molecular mean free path based on the hard sphere approximation is plotted through the boundary layer and is normalized by the roughness

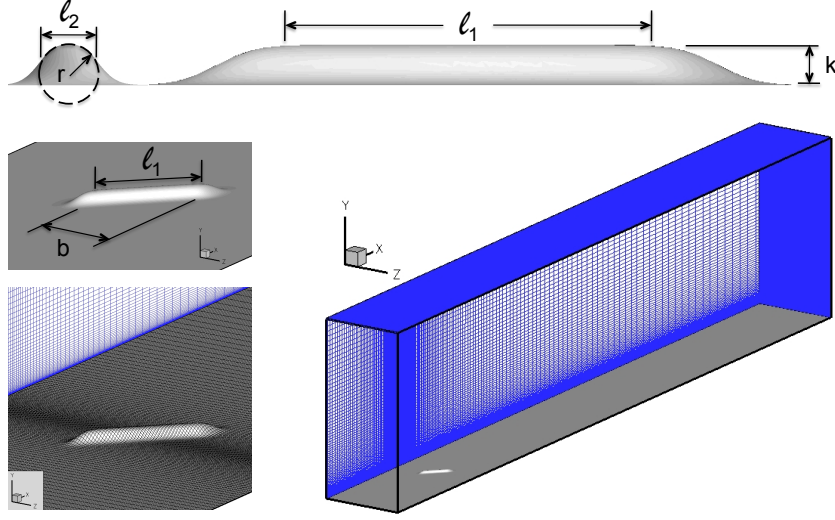


Figure 5.4: Characteristic lengths of asymmetric geometry and CFD mesh. Geometry is shown from end view (upper left) and side view (upper right) perspectives. The mesh is extruded in the wall-normal direction from the geometry surface.

height k for the respective cases. This quantity is a local Knudsen number which, for these undisturbed boundary layer flows, indicates the regime (rarefied/continuum) of the flow approaching the discrete surface roughness, as discussed in Chapter 1.

The height of the discrete surface roughness examined at each altitude are prescribed as

$$k = 0.25\delta_T. \quad (5.1)$$

These values are indicated by the filled circles at $y/\delta_T = 0.25$ on each profile in Figures 5.3(a),(c), or equivalently $y/\delta_u \approx 0.30$ in Figure 5.3(b).

In the final CFD step, the profiles from the two-dimensional flat plate boundary layer solutions are applied as inflow boundary conditions for the three-dimensional CFD solutions. The quantities of pressure, temperatures (translational and internal), velocities and species mass fractions are interpolated onto the boundaries, and DPLR is used to generate the CFD flowfield solution on a detailed volume mesh. The structured volume mesh for the discrete *asymmetric* roughness geometries is constructed as a rectangular computational domain (Figure 5.4) which includes the discrete surface roughness geometry on the solid flat plate wall (bottom), boundary layer inflow profiles specified by a pointwise boundary condition (front and top), supersonic exit condition (back) and zone boundary conditions (allowing for outflow) on the sides of the domain [87]. The roughness geometry is an elongated hump of height k , and is shown from sideview and endview perspectives in Figure 5.4. The geometry is characterized by height k , lengths ℓ_1 , ℓ_2 , radius of curvature r , and is oriented at an angle of 45° to the oncoming flow. The flat plate and surface roughness are specified as viscous, isothermal walls with either a slip- or no-slip condition enforced at the wall. In both the high altitude and low altitude cases, the computational domain is $300k$ in length and $33k$ in the spanwise direction.

The roughness center is located at approximately $x_k = 50k$ from the front of the computational domain. The roughness lies at the spanwise center of the domain ($z_k = 0$ m) and occupies one-third of the total span. The heights of the computational domains are $40k$ and $72k$ for the high and low altitude

cases, respectively. These heights were specified according to the location of the oblique shock generated from the flat plate leading edge, such that the oblique shock is not included in the three-dimensional flowfield solutions. The characteristic geometric length scales of the roughness and the computational domain for the asymmetric roughness are outlined in Table 5.2. These scales (with the exception of the domain height, which are listed separately) apply to both the high and low altitude cases, and are presented based on the roughness heights k .

Table 5.2: Computational length scales (Geometry and CFD/hybrid domains)

	Asymmetric ($k = 0.012\ m, 0.007\ m$)	Symmetric ($k = 0.012\ m$)
ℓ_1	$8k$	$4k$
ℓ_2	k	$4k$
b	$5.6k$	$5.6k$
r	$0.72k$	$0.06k$
CFD		
L_x	$300k$	—
L_y	$40k, 72k$	$40k$
L_z	$33k$	—
x_k	$50k$	—
L_d	—	$52k$
R_k	—	$26k$
Hybrid		
L_x	$26k, 25k$	$26k$
L_y	$4k, 6k$	$4k$
L_z	$16k$	$8k$ (half domain)
x_k	$9k$	$9k$

The structured volume mesh for the *symmetric* roughness geometries is constructed as an extruded ‘lilypad’ computational domain (Figure 5.5)

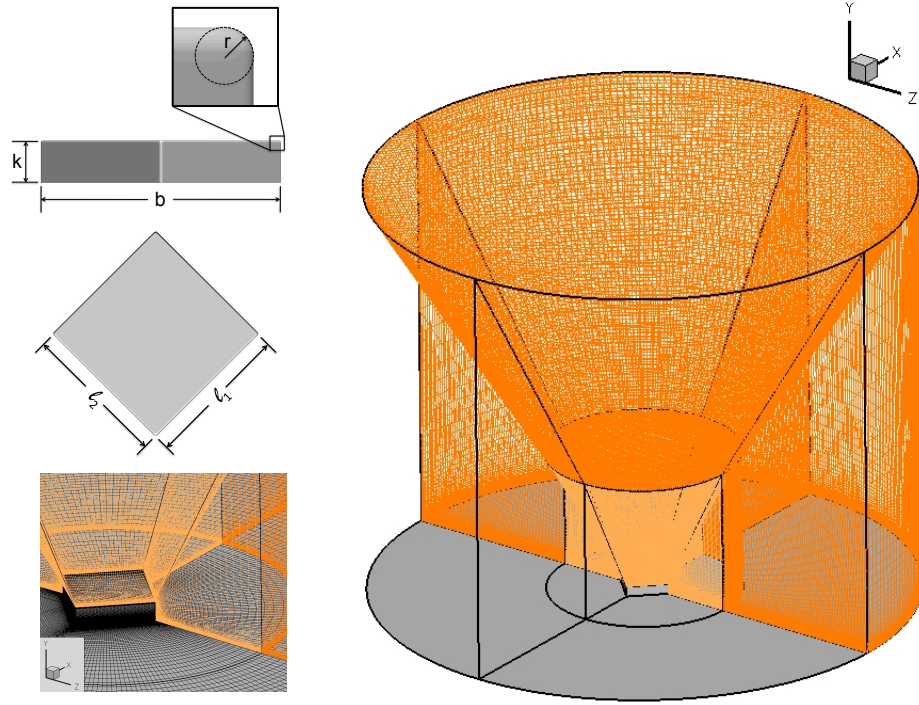


Figure 5.5: Characteristic lengths of symmetric geometry and CFD mesh. Geometry is shown from front view (upper left) and planview (middle left) perspectives. The mesh is extruded outward from the geometry surface.

which includes the discrete surface roughness geometry on the solid flat wall (bottom), boundary layer inflow profiles specified by a pointwise boundary condition on the third and fourth quadrant faces (these are removed in the figure to show the roughness), supersonic exit condition on the top face and first and second quadrant faces (back faces in figure) and zone boundary conditions for the shared faces on the interior domain [87].

The roughness geometry is a ‘pizzabox’ shape with height k , and is

shown from frontview and planview perspectives in Figure 5.5. The geometry is characterized by height k , lengths ℓ_1 , ℓ_2 , radius of curvature r , and is oriented with the diagonals parallel and perpendicular to the oncoming flow. The flat wall and surface roughness are again specified as viscous, isothermal walls with either a slip- or no-slip condition enforced at the wall. The computational domain has a diameter of $L_d = 52k$ and height $L_y = 40k$. The roughness is located in the center of the lilypad, with the front of the computational domain at a radial distance of $R_k = 26k$ from the roughness. The characteristic geometric length scales of the roughness and the computational domain for the symmetric roughness are outlined in Table 5.2. These scales are presented based on the roughness height k .

After the CFD solutions are obtained, the flowfield quantities are interpolated onto the computational boundaries of the hybrid domain, and the DSMC solver is used to model the detailed, non-equilibrium flowfield in the region surrounding the roughness and in the near wake. The solid surface defining the flat plate and roughness geometry in the CFD solution is transformed into an unstructured grid using the same surface node points. This is to ensure that the same geometry is represented in both flow solvers.

The computational boundary conditions and boundary locations in terms of the breakdown parameters presented in Chapter 3 are presented in detail later on in Section 5.3, but an overview of the domain length scales is presented here. A rectangular computational domain is used for both the asymmetric and symmetric geometries. The bottom of the domain consists of

the solid surface with the roughness, and the side and top walls are specified as pointwise inflow boundaries. The solutions for the asymmetric geometry cases must be solved on full domains, and the length scales of the computational domains are provided in Table 5.2. In each case, the roughness is positioned at the spanwise center of the domain, and the roughness center is approximately $x_k = 9k$ from the front of the computational domain. The flowfield for the symmetric geometry is obtained through use of a symmetry plane along the centerline of the roughness, along which a specular wall boundary is specified. The length scales for this case are also reported in Table 5.2.

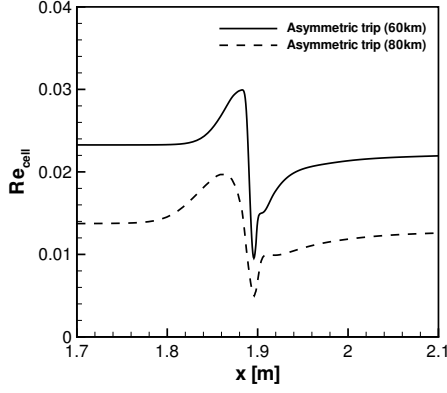
5.2.2 Convergence Requirements

A detailed comparison between the CFD and hybrid flowfield solutions, particularly surface heat flux and gradient-based flow quantities, requires fully resolved flowfield and surface grids. The CFD solutions were solved on computational domains with grid spacing of $O(10^{-6})$ m at the wall, and grid convergence studies were conducted to ensure that the solutions presented here are grid-independent. The boundary layer contained approximately 40 – 50 grid points, and grid stretching was applied in the wall-normal direction. Grid points in the streamwise and spanwise directions were clustered in the regions of high gradients surrounding the roughness and in the wake, to maintain cell Reynolds number of $Re_{cell} \leq 1$. This quantity is plotted in Figure 5.6(a) as a function of streamwise distance for the asymmetric geometries. The figure shows the cell Reynolds number at the surface of the roughness for both the

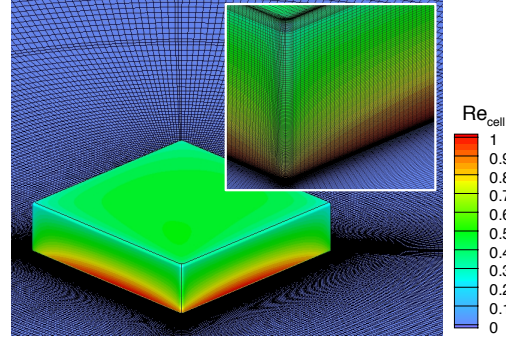
high and low altitude cases, and this quantity remains well below the desired limit. It should be noted that the cell Reynolds number varies over the roughness, but the values in Figure 5.6(a) represent the maximum values in each case.

The edges and corners of the pizzabox geometry are defined by a very small radius of curvature (Table 5.2), and grid points were clustered on these features to resolve the high flowfield gradients and surface heat flux in these regions. The top and side faces of the geometry are defined by (128×128) and (180×128) grid points respectively, and radius of curvature on the edges were represented by 22 grid points. This resulted in a local cell Reynolds number of $Re_{cell} = 0.3$ on the curved features, and $Re_{cell} = 0.5$ on the top of the geometry (Figure 5.6(b)). Regions of the flat surfaces on the windward side of the geometry approach values of $Re_{cell} = 1.0$, but these regions are not in the vicinity of the peak surface heating, which occurs at the top corner of the roughness. The cell Reynolds number on the surface surrounding the roughness remains well below a value of unity. It should also be noted that all of these results are solved as steady-state solutions, and the solutions were considered converged when the L_2 norm residual based on density fell below 10^{-6} .

Fully resolved DSMC solutions require convergence in the computational cell size, the number of simulated particles, as well as the computational time step used to advance the solution. In order to resolve gradients within the flowfield, the computational cells should be less than or equal to the local



(a) Asymmetric geometry (CFD)



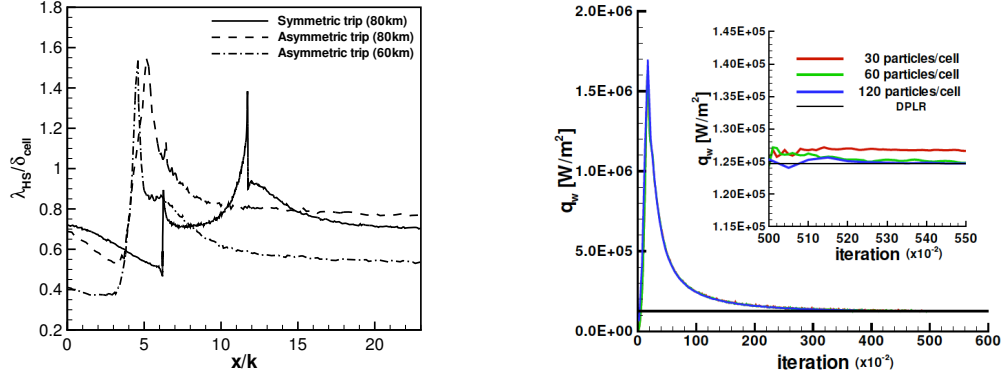
(b) Symmetric geometry (CFD)

Figure 5.6: Cell Reynolds numbers determined from near-wall cells for (a) asymmetric roughness and (b) symmetric roughness cases. Profiles in (a) are taken through the maximum cell Reynolds number location.

molecular mean free path, such that $\delta_{cell} \leq \lambda$. Within the DAC solver, this is achieved by specifying that the Level-II cells achieve mean-free-path resolution throughout the computational domain. The ratio of local mean free path to the cell size (where δ_{cell} represents the average dimension of a Level-II cell) is shown in Figure 5.7(a) as a function of streamwise distance for each of the cases examined. The values were extracted from the computational cells nearest the solid wall where gradients are largest, and were taken at the spanwise location of peak surface heating on each of the geometries. The computational cells used in the DSMC simulations achieve mean free path resolution upstream and downstream of the roughness, and nearly resolve the mean free path over the roughness.

Since the macroscopic flowfield quantities in DSMC are determined by

sampling the particles within each cell, it is important that each cell contains a sufficient number of simulated particles for a statistically significant measure of flow quantities. The surface heat flux predicted by DAC was found to be especially sensitive to the number of particles per cell specified in near wall cells. DAC populates each cell with ten simulation particles everywhere in the domain. However, this results in a heat flux that overpredicts the CFD (DPLR) flat plate boundary layer flow value by approximately 10%, for the conditions considered here. The agreement in wall heating was found to improve by increasing the number of particles per cell in the near-wall cells, while specifying ten particles per cell in the flowfield cells away from the wall. Figure 5.7(b) shows the total wall heat flux per unit area as a function of iteration in time for 30, 60 and 120 particles per near-wall cell. The CFD (DPLR) value is indicated by the black line. In the inset figure, the solution has reached steady state, and time-averaging is started at iteration 50,000 for each of the cases. Using 30 particles per cell shows very good agreement with the CFD heat flux, with a difference of only 1.4% in the predicted values. Increasing to 60 particles per cell reduces the difference in wall heating to less than 0.2%. Using 30 particles per cell provides reasonable agreement in the flat plate heat flux values while allowing the simulation to remain computationally tractable, so this criterion is adopted in the hybrid simulations presented in this work. A summary of the computational cost of the three-dimensional CFD/hybrid solutions are provided in Appendix E.



(a) Mean-free-path resolution in near-wall (Level-II) DSMC cells. (b) DSMC wall heat flux dependence on number of particles per cell (near-wall).

Figure 5.7: DSMC convergence criteria in (a) molecular mean free path resolution and (b) number of particles per cell (near-wall).

5.3 3D Flowfield Solutions: Flow Features, Breakdown Surfaces and Hybrid Interface Location

The concepts introduced in Chapter 3 are now applied to analyze the breakdown of the CFD flowfield solution in the region surrounding the roughness geometry. Before doing this, the general flow features generated by the asymmetric versus symmetric roughness geometries are examined in detail. The discussion in the first portion of this section is limited to the high altitude cases, in which flows from both the asymmetric and symmetric roughness geometries are modeled. The hybrid interface locations and corresponding breakdown parameters are examined for the three cases outlined in this work.

The flow features of the asymmetric and symmetric geometries are highlighted in Figures 5.8-5.11. The disturbance field generated by boundary layer flow over the asymmetric roughness is visualized by the streamtrace ‘ribbons’

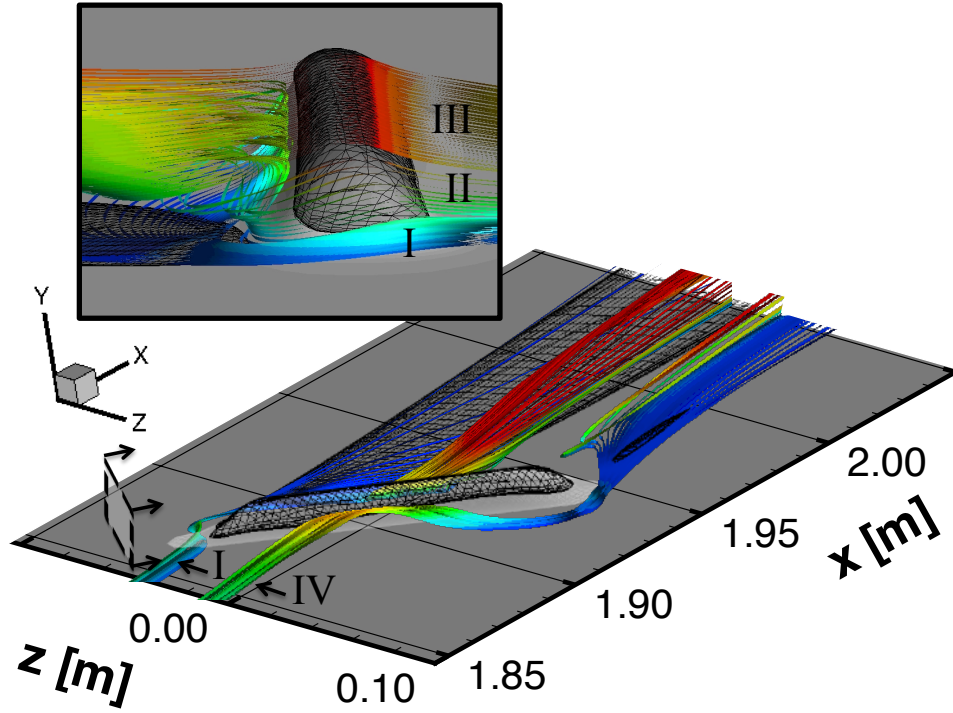


Figure 5.8: Disturbance flowfield (visualized by streamtrace groups $I - IV$ colored by wall-normal height) generated by asymmetric roughness. Black mesh isosurfaces (on roughness and in wake) indicate regions of strong non-equilibrium ($B > 0.15$). Roughness (shown in light gray) is centered over $x = 1.91 \text{ m}$. Enlarged inset figure shows details of disturbance field from an end view perspective near the leading edge (shown schematically by viewing ‘window’ with arrows in main figure).

shown in Figure 5.8 and magnified in the enlarged inset figure. Note that the inset figure shows an end view perspective of the leading edge according to the viewing ‘window’ with arrows in the main figure, and so the general flow direction in the inset figure is from right to left. The streamtraces represent the local velocity vector, and are colored according to wall-normal distance where blue indicates a position at the wall, red indicates a position at the height of the roughness. Breakdown surfaces are shown in the black mesh isocontours; these surfaces highlights regions where the breakdown parameters introduced in Chapter 3 exceed a value of 1.5. Four distinct groups of streamtraces (labeled I-IV) are shown for clarity of discussion.

Flow approaching the leading edge of the roughness near the wall (Figure 5.8, Group I) is immediately swept towards the centerline of the roughness in the wake, and up the backside of the roughness in a recirculation region where it is lifted nearly one roughness height. This flow continues downstream in the wake with a slight rotation in a lifting vortex (shown by the red streamtraces in the wake originating from Group (I)), which will be quantified later in this chapter using the Q -criterion. Flow following this path exhibits relatively strong non-equilibrium immediately downstream of the leading edge, as indicated by the breakdown surface.

The second group of streamtraces (Group II, shown only in enlarged image of Figure 5.8) highlights flow that passes over the shoulder of the roughness. This flow is also swept immediately towards the centerline of the roughness, and comprises the central portion of the recirculation region, making a cou-

ple of rotations behind the roughness before passing downstream in the wake. The third group (Group III, again shown only in enlarged figure) represents flow that passes over the crest of the asymmetric roughness. Flow from both Group II and Group III exhibits strong non-equilibrium as it passes over the shoulder and crest, as gradients become very large in these regions. In fact, breakdown of the Navier-Stokes solution according to the breakdown criterion discussed in Chapter 3 occurs over the majority of the roughness geometry, as indicated by the breakdown surface.

The fourth group of streamtraces (Figure 5.8 Group IV) highlights flow that originates upstream of the roughness at a height in the boundary layer that is approximately one-third of the roughness height. This flow impinges on the windward side of the roughness and is swept downward toward the wall, away from the roughness centerline. As it pass over the trailing edge of the roughness, it is swept toward the roughness centerline. Some of the streamtraces are swept into the recirculation region and are lifted upward in the wake. A very small region of non-equilibrium is found downstream of the trailing edge, but the non-equilibrium induced by the flow over the leading edge is more prevalent.

The breakdown surfaces shown in Figure 5.8 are presented again in Figure 5.9, with a mapping of the surface heating. A detailed, quantitative comparison of the predicted surface heating by the CFD and hybrid solvers will be presented later in the chapter, but here it is noted that streaks of increased heating (relative to the comparatively undisturbed flow in front of

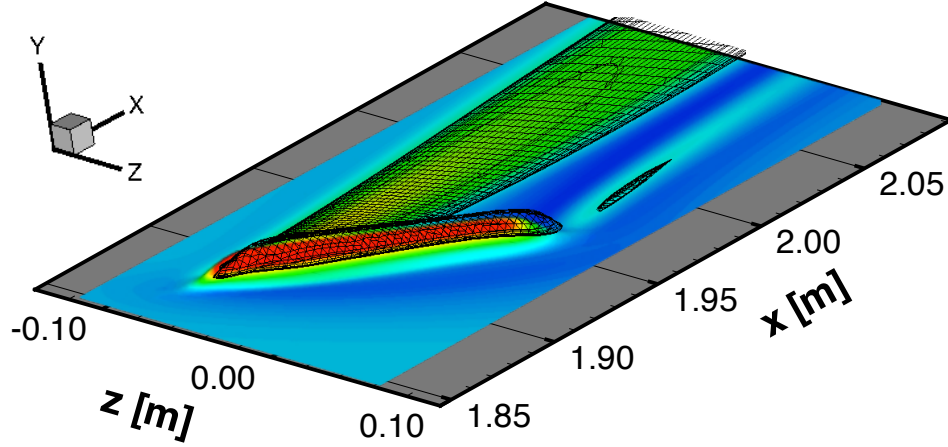


Figure 5.9: Surface heating in regions surrounding asymmetric roughness. Black mesh isosurfaces (on roughness and in wake) indicate regions of strong non-equilibrium ($B > 0.15$). Roughness is centered over $x = 1.91$ m.

the roughness) are found downstream of the leading and trailing edges of the roughness. These streaks coincide with near-wall streamwise-oriented vortices, which generate local regions of high gradients at the wall. The highest heating indicated by the red contour levels is found on the windward side of the roughness near the leading edge, and each of these regions correspond to breakdown of the Navier-Stokes solution.

The disturbance field generated by boundary layer flow over the symmetric roughness is presented in Figure 5.10 and magnified in the enlarged inset figure. This flowfield is also visualized by the streamtrace ‘ribbons’ which are colored according to wall-normal distance, where blue again indicates a position at the wall, red indicates a position at the height of the roughness.

Breakdown surfaces are shown in the black mesh isocontours where the breakdown parameters exceed a value of 1.5. Three distinct groups of streamtraces (labeled I-III) are shown for this roughness geometry.

The first and third group of streamtraces (Groups I and III, with Group I shown in enlarged image of Figure 5.10) represent flow that originates upstream of the roughness from a wall-normal location equivalent to one-third of the roughness height. This flow impinges on the windward side of the roughness, and is swept downward toward the wall, away from the roughness centerline. As the flow passes the corner of the roughness, it is swept back toward the roughness centerline, and becomes entrained in a recirculation region. The recirculating flow impinges the leeward side of the roughness and is lifted nearly one roughness height as it is pushed away from the roughness centerline. The flow is then turned downstream into the wake, forming a counter-rotating vortex pair that is symmetric across the roughness centerline. The flow highlighted by each of these groups exhibits strong nonequilibrium near the flat wall on either side of the roughness. This non-equilibrium is found in portions of the recirculation region near the wall, and persists downstream in the wake.

The second group (Group II, shown only in enlarged image of Figure 5.10) represents flow that passes over the top of the symmetric roughness. Flow from this group exhibits strong non-equilibrium as it passes over the roughness, which can be attributed to the large gradients that form on the top of the roughness. It is interesting to note that in the case of the symmetric roughness, the breakdown surface is mostly restricted to the top surface of

the roughness, whereas the asymmetric roughness surface was almost entirely dominated by non-equilibrium flow.

The breakdown surfaces shown in Figure 5.10 are presented again in Figure 5.11, with a mapping of the surface heating. In this roughness geometry configuration, the streaks of increased heating (relative to the comparatively undisturbed flow in front of the roughness) are symmetric in the wake of the roughness as expected. These streaks again coincide with near-wall streamwise-oriented vortices, which generate local regions of high gradients at the wall. The highest heating indicated by the red contour levels is found on the windward side of the roughness near the leading edge corner and along the top edges. These regions correspond to breakdown of the Navier-Stokes solution, as indicated by the overlapping breakdown surface.

In both the asymmetric and symmetric geometry configurations, it is found that the breakdown of the Navier-Stokes equations occurs both on and downstream of the roughness. Although the formation of a weak bow shock just upstream of the roughness geometries is apparent in both cases (discussed later in Sections 5.4.1 and 5.5.1), the flow gradients through the weak shock remain sufficiently small that the flow may still be adequately represented by the CFD solution. It is emphasized that the surface roughness is one-quarter of the boundary layer thickness, and the sonic line in an *undisturbed* boundary layer is located at distance above the wall equivalent to one-half of the roughness height. A taller roughness would certainly generate a stronger bow shock, and regions of non-equilibrium flow would possibly be found upstream

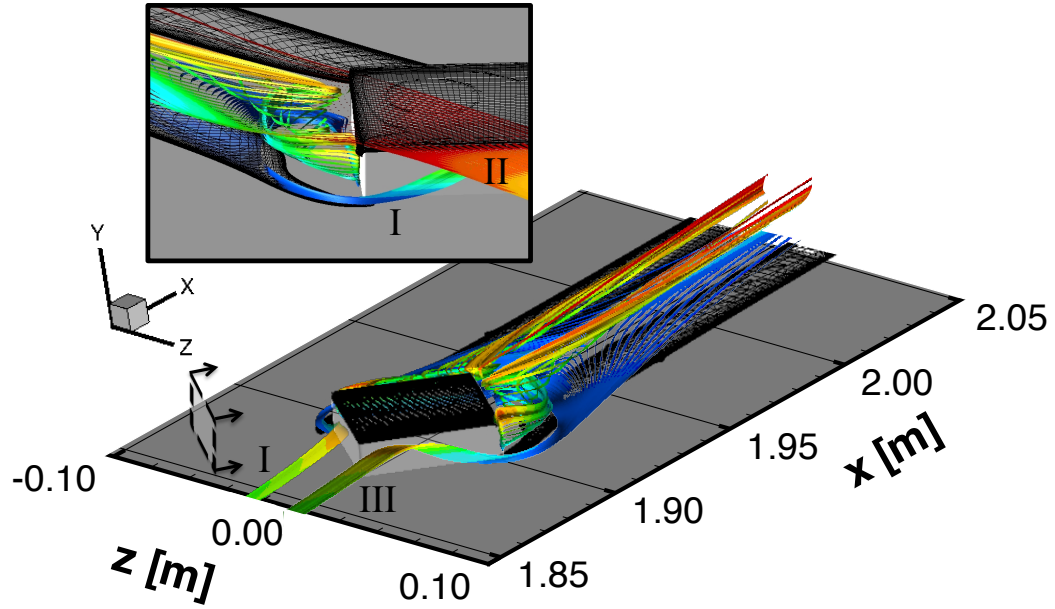


Figure 5.10: Disturbance flowfield (visualized by streamtrace groups *I – III* colored by wall-normal height) generated by asymmetric roughness. Black mesh isosurfaces (on roughness and in wake) indicate regions of strong non-equilibrium ($B > 0.15$). Roughness (shown in light gray) is centered over $x = 1.91$ m. Enlarged inset figure shows details of disturbance field from an end view perspective near the leading edge (shown schematically by viewing ‘window’ with arrows in main figure).

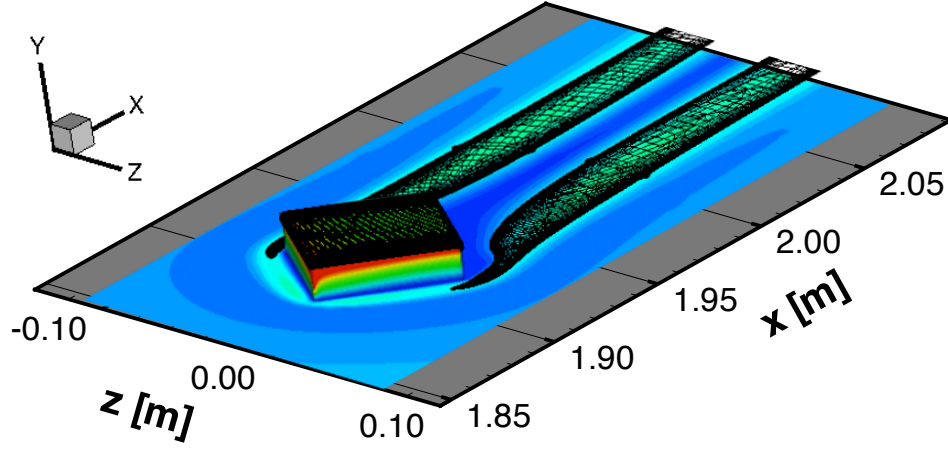


Figure 5.11: Surface heating in regions surrounding symmetric roughness. Black mesh isosurfaces (on roughness and in wake) indicate regions of strong non-equilibrium ($B > 0.15$). Roughness is centered over $x = 1.91$ m.

of the roughness due to the strong shock formation.

The hybrid interface boundaries used in this work may now be examined in terms of the breakdown analysis presented in Chapter 3. The breakdown criterion adopted for this work follows from the work of Garcia and Alder [23], in which the DSMC particles are generated at an interface where $B \leq 0.1$. For the CFD flowfields presented in Figures 5.8-5.11, the breakdown surface in the wake extends hundreds of roughness heights downstream. To keep the DSMC solutions computationally tractable, the downstream interface in this work cuts across the breakdown surface in the wake. This does not appear to have an adverse impact on the flowfield solution further upstream in the hybrid computational domain, since the bulk boundary layer flow is in the

general streamwise direction out of the downstream interface.

The asymmetric roughness geometry from the high altitude case is outlined here, but the same discussion applies to the symmetric geometry and low altitude asymmetric geometry cases presented in this work. The hybrid domain is shown schematically in Figure 5.12. Recall that since this is an asymmetric geometry, the entire flowfield is modeled in the hybrid solver. The computational domain is comprised of five pointwise inflow boundaries (Figure 5.12), whose properties are determined from the CFD three-dimensional flowfield solution. The local number density contours are shown on each of the inflow boundaries, which include the front and back interfaces (faces of constant x -value), left and right interfaces (faces of constant z -value) and the top interface (face of maximum constant y -value). The bottom boundary is a solid surface consisting of the flat plate and the discrete surface roughness, shown as the shaded gray surface. The bottom surface is prescribed a uniform temperature of $T_w = 1200\text{ K}$, and DSMC particles colliding with the surface are reflected assuming full thermal accommodation. The interpolated CFD boundary condition includes the weak bow shock and expansion regions on the top interface, as well as the flow features in the wake.

Profiles of the breakdown parameters presented in Chapter 3 are shown for the front, back and top boundary faces of Figure 5.12 in Figure 5.13(a,b). Only breakdown parameters which exceed values of $B \geq 10^{-2}$ on any of the hybrid interfaces are shown. In this example case, the diffusion breakdown parameters were all less than $O(10^{-3})$ and are not presented, as well as several

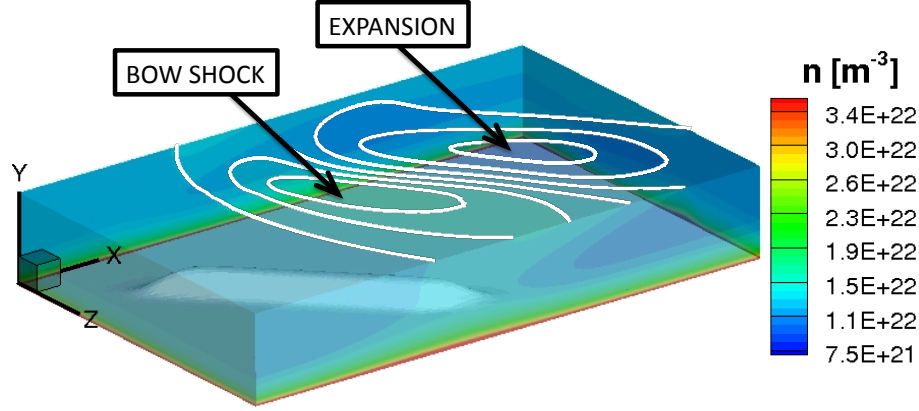


Figure 5.12: Hybrid domain interface boundaries for the asymmetric geometry (high altitude case). The domain is comprised of five pointwise inflow boundaries (front, back, left, right and top faces) and a solid bottom wall comprising a flat plate with the roughness.

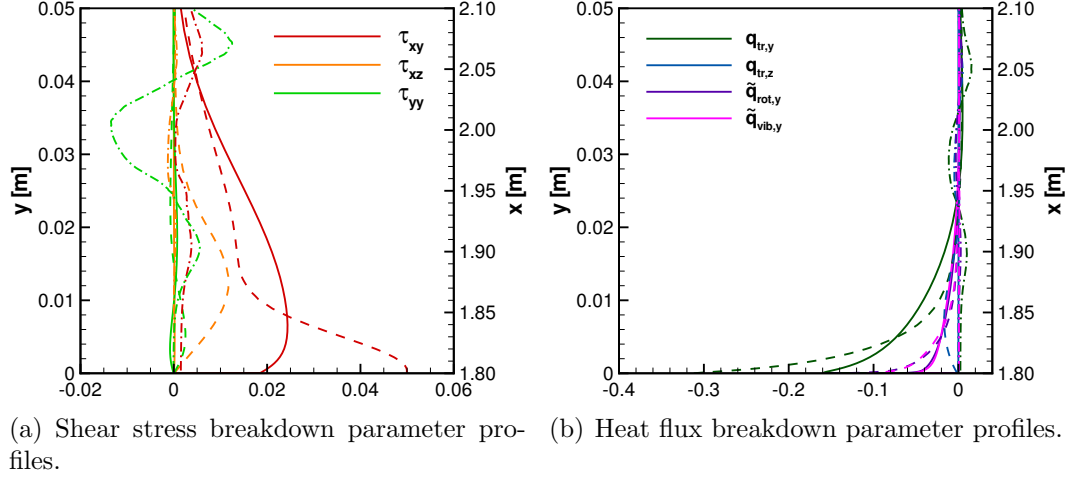


Figure 5.13: Breakdown parameter profiles taken from hybrid interface boundaries of asymmetric roughness geometry (Figure 5.12). Only breakdown parameters which exceed $B \geq 10^{-2}$ are shown. Profiles are extracted from front (solid lines), back (dashed lines) and top (dash-dotted lines) interfaces shown in Figure 5.12.

components of the shear stress tensor and heat flux vectors. The profiles are extracted through the extremum of each breakdown parameter along the respective boundary interface. The solid lines in Figure 5.13(a,b) indicate profiles extracted from the front interface, dashed lines are profiles from the back interface, and dash-dotted lines are profiles from the top face. The front and back profiles are presented as a function of wall-normal distance y , while the top profiles are a function of streamwise distance x . From these profiles it is observed that the local flow gradients along the top interface due to the compression (bow shock) and expansion regions are relatively minor, as the magnitude of the parameters all remain within the breakdown criterion.

On the front interface, the values of $\tilde{q}_{rot,y}$ and $\tilde{q}_{vib,y}$ approach a value of -0.05 at the wall, while the parameter $q_{tr,y}$ slightly exceeds this value. The breakdown criterion is exceeded on the back interface by the parameter $q_{tr,y}$, and the values from the internal heat fluxes approach -0.1 . As discussed earlier, these values are exceeded due to the large wall-normal gradients downstream of the roughness leading edge (indicated by the breakdown surface in Figure 5.8). By examining these breakdown parameter profiles, it is found that the breakdown of the Navier-Stokes equations in these regions is due to the wall-normal gradients in temperature, as the shear stress parameters remain relatively small (Figure 5.13(a)).

As a further examination of these non-equilibrium flowfields, a detailed comparison among the CFD (no-slip and slip wall conditions) and hybrid solutions is presented in the following sections. While comparisons could be made

among an overwhelming number of flow quantities, the results presented in these sections focus on the velocity field (and corresponding vortex structures determined from the Q -criterion[42]), translational/vibrational thermal non-equilibrium, and local surface heating. The comparisons among the CFD and hybrid solutions are restricted (spatially) to within the boundaries of the corresponding hybrid domain.

5.4 Asymmetric Geometry Configuration

5.4.1 Flowfield comparisons at 80 km

The first set of results presents a comparison of the CFD and hybrid solutions for the asymmetric roughness geometry at 80 *km*. The flowfield results from the CFD no-slip and slip wall conditions are nearly indistinguishable, so in the following discussion, only results from the analysis of the CFD slip wall and hybrid solutions are presented. Comparisons of the velocity field are presented in Figure 5.14 for the wake flow at a location approximately $10k$ downstream of the roughness center. The figures are oriented looking downstream in the $+x$ direction. The streamwise velocity contours are shown in Figure 5.14(a). The field contours represent the hybrid solution, and the CFD values are shown by the contour lines. In both solutions, the wake flow produced by the roughness indicates high-speed flow which penetrates toward the wall behind the leading edge ($z \approx -0.04$ *m*), and to a lesser extent in the flow behind the trailing edge ($z \approx 0.05$ *m*). In between these regions, low speed flow is pushed upward away from the wall forming a streak of low speed

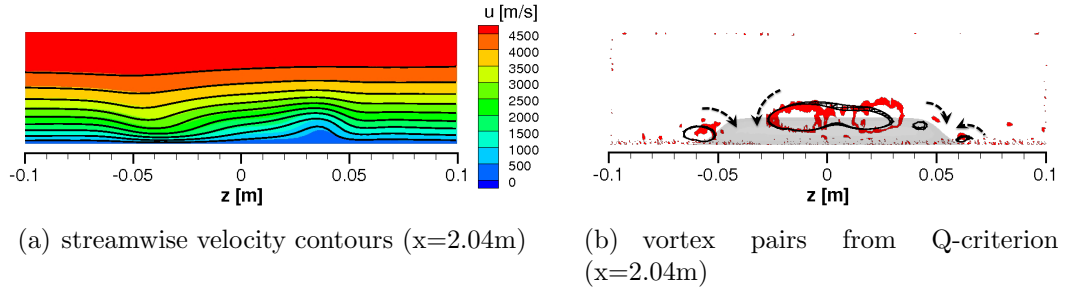


Figure 5.14: Flow features in wake of asymmetric roughness (80 km altitude) at $x = 2.04 \text{ m}$. (a) Streamwise velocity contours from hybrid solution (contour flood) and CFD slip-wall solution (contour lines). (b) Vortex pairs determined from Q-criterion. Vortices are shown as isocontours of $Q = 1.5 \times 10^6$ for CFD (black) and $Q = 6.0 \times 10^6$ for hybrid (red) solutions, and the roughness (gray) is shown for reference. Note that the positions of vortex cores are similar, but the hybrid vorticity (relative to the strain rate) is stronger.

flow, centered over $z = 0.04 \text{ m}$. The CFD solution (line contours) predicts a slightly wider low speed streak compared to the hybrid solution.

The high- and low-speed streaks that are generated by the roughness correspond to a pair of counter-rotating vortices that originate from the leading and trailing edges of the roughness. These vortex pairs are visualized by isocontours of Q in Figure 5.14(b), which picks out flow regions where the norm of the vorticity tensor is greater than the norm of the rate of strain tensor [35]. The CFD vortex pairs are shown by the black isocontours, and the hybrid vortices are shown in red. The vorticity strength increases on the region inside of the vortex rings formed by the iscontours, and reaches a peak at the center of the vortex core. The sense of rotation of these vortices is indicated by the sets of arrows, and the roughness geometry is shown in gray at this downstream location for reference. Due to statistical noise in the DSMC

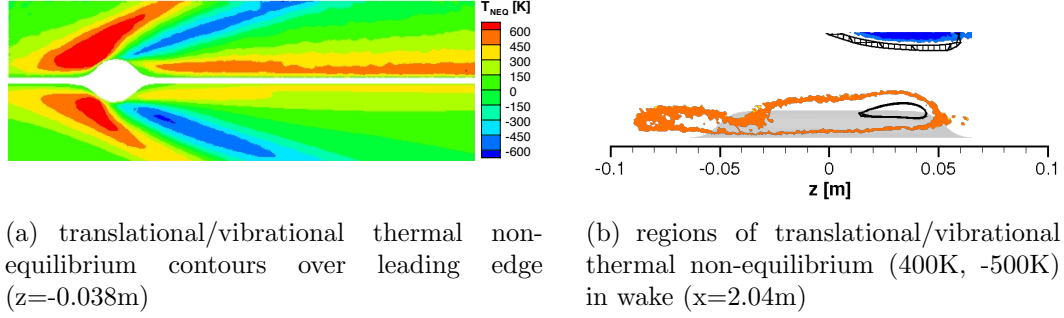


Figure 5.15: Translational/vibrational thermal non-equilibrium in flow surrounding asymmetric roughness at 80 *km*. (a) Thermal non-equilibrium contours from hybrid solution (top) and CFD slip-wall solution (bottom) taken at the roughness leading edge $z = -0.038$ *m*. Contours indicate the difference between translational and vibrational temperatures, where $T_{NEQ} = T_{tr} - T_{vib}$. (b) Isocontours of thermal non-equilibrium in the wake, taken at a location 10*k* downstream of roughness. Colored isocontours (following levels in (a)) represent hybrid solution, black represent corresponding CFD solution.

solution, there are additional isolated regions of vorticity that are seen in the domain, particularly near the wall and boundaries of the hybrid domain.

The analysis of the CFD and hybrid solutions using the Q-criterion indicates that the vortices generated by the roughness leading edge are stronger compared to the trailing edge vortices due to the asymmetry of the geometry, although the trailing edge vortices become difficult to detect in the DSMC solution. The vorticity in the wake predicted by the hybrid solution is observed to be slightly stronger compared to the vorticity predicted by the CFD solution, as indicated by the relative strength of the vortex pairs. It is also interesting to note that the span of the counter-clockwise (CCW) leading edge vortex in the hybrid solution is greater than the corresponding CCW vortex

in the CFD solution, i.e., both the strength and size of this vortex are greater in the hybrid solution. As will be discussed later, this is found to have a measurable impact on the surface heating in the wake of the roughness.

The translational/vibrational thermal non-equilibrium in the flow predicted by the hybrid and CFD slip wall solutions are presented next in Figure 5.15(a) and (b). The contours in Figure 5.15(a) show the difference in $[K]$ in the translational and vibrational temperatures in the flow, where a positive temperature difference indicates areas of the flow where $T_{tr} > T_{vib}$. The hybrid solution is shown on top, and the CFD solution is mirrored on the bottom for comparison. This slice is taken at a spanwise location at the leading edge of the roughness, ($z = -0.038 \text{ m}$). Toward the front of the domains, the CFD and hybrid solutions are in excellent agreement. Just upstream of the roughness, a bow shock forms, and the hybrid solution predicts higher vibrational non-equilibrium in this region compared to the CFD solution. In the expansion region that forms aft of the roughness (indicated by the blue contours), the CFD solution predicts slightly greater vibrational non-equilibrium. In the wake region, the flow is processed by another compression region/shear layer as the flow passes over the top of the roughness and is brought parallel to the wall. The vibrational non-equilibrium in the hybrid solution is again greater than the CFD solution in this region.

A comparison of the thermal non-equilibrium in the wake at a location $10k$ downstream of the roughness center is provided in Figure 5.15 (b). The colored isocontours represent the hybrid solution, and follow the contour

levels in Figure 5.15 (a). The corresponding CFD isocontours are shown in black. The hybrid solution shows a greater spanwise extent of thermal non-equilibrium near the wall (orange contour) compared to the CFD solution. It should be emphasized that the extent of thermal non-equilibrium found in this case is at most $T_{NEQ} = 700\text{ K}$, which is approximately 20% of the gas temperature within the boundary layer. The *differences* between the CFD and hybrid solutions in terms of predicted thermal non-equilibrium are on the order of 5%, and so the effects of thermal non-equilibrium on the overall flowfields are relatively subtle.

5.4.2 Local surface heating at 80 km

The surface heat flux predicted by the CFD and hybrid solutions are presented in Figure 5.16(a)-(c). The flow in these figures is in the general x -direction (bottom to top), and the contours represent the local surface heating on the roughness and in the wake. The heating on the flat surface upstream of the roughness (referred to as the ‘baseline’ surface heating) was approximately $Q_0 = 9.1 \times 10^4\text{ [W/m}^2\text{]}$. The windward side of the roughness experiences the highest surface heating, particularly the leading edge region, and the heating drops off gradually along the crest of the roughness toward the trailing edge. The CFD contours indicate that the presence of the roughness has a more pronounced impact on the surface heating upstream of the roughness, relative to the hybrid solution. The surface heating in the wake of the roughness is qualitatively similar among the CFD and hybrid solutions. All of the solutions

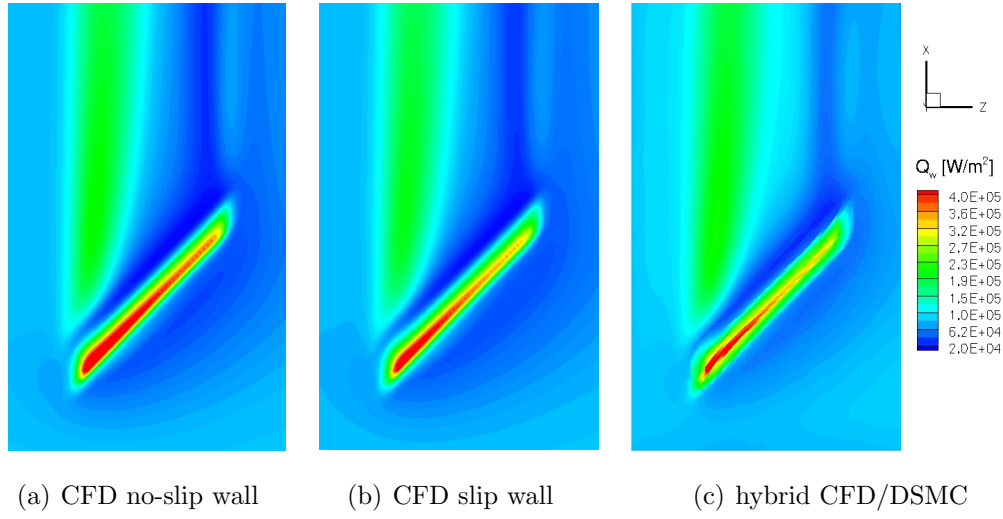


Figure 5.16: Surface heating contours generated by asymmetric roughness at 80 *km* from (a) CFD no-slip wall (b) CFD slip wall and (c) hybrid solutions. General flow direction is from bottom to top.

predict increased heating in the wake due to the leading edge vortex, while the heating downstream of the trailing edge is relatively weak. The hybrid solution, however, indicates a wider heating footprint due to the leading edge vortex.

To quantify these differences, the total surface heating is extracted at several streamwise locations from the CFD and hybrid solutions, both over the roughness and in the wake, as indicated schematically in Figure 5.17. In particular, the spanwise surface heating profiles are compared at locations of peak heating on the roughness, the center of the roughness, the peak heating in the wake and at a location 10*k* downstream of the roughness center (Figure 5.17, red, orange, yellow and purple profiles).

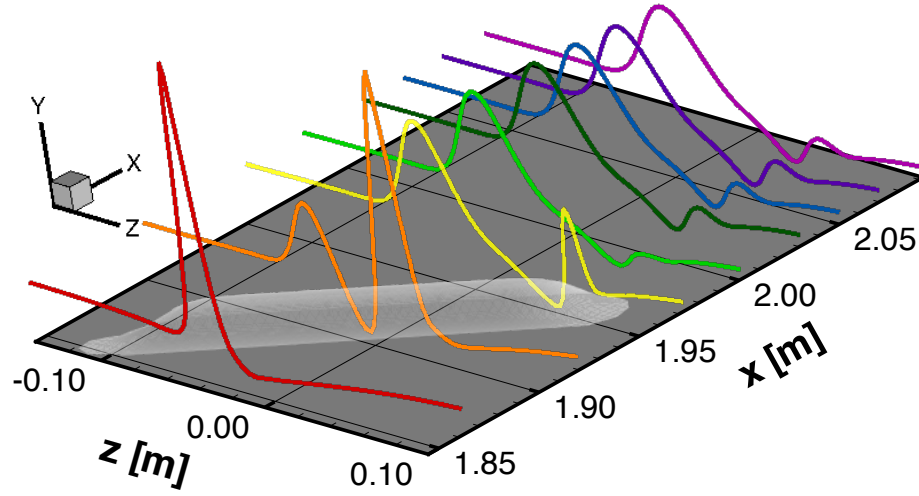


Figure 5.17: Spanwise profiles of surface heating acquired at various streamwise locations for asymmetric roughness. Profiles highlight peak heating on roughness (first spanwise profile in red) as well as vortex heating in wake in the profiles downstream of the roughness (shown schematically in gray).

The corresponding spanwise profiles are presented in Figure 5.18 (a)-(d) (note that the yellow profile from Figure 5.17 is shown here in black). CFD no-slip surface heating is represented by the solid line, the slip surface heating is shown by the dashed line, and the hybrid solution is shown as the dash-dotted line. The first set of profiles (Figure 5.18(a)) are extracted at the streamwise location of peak surface heating predicted by the *hybrid* solution. Note that the predicted magnitude and location of peak heating varies among the solutions, and peak roughness and vortex heating values corresponding to each solution are presented in Table 5.3. At this location, the spanwise location of the local peak heating is nearly identical among the three solutions. Towards the centerline of the roughness (at $z = 0 \text{ m}$), the surface heating reaches a

local minimum, which corresponds to the region immediately upstream of the roughness. The CFD solutions predict relatively lower heating on the flat surface surrounding the roughness. This corresponds to the earlier observation that the CFD solution predicts a more pronounced impact of the disturbance field generated by the roughness on the upstream surface heating. Note that at the very edges of these profiles (indicating the edge of the hybrid domain), the hybrid solution converges to the CFD solution which, recalling the discussion of Chapter 3, is used to specify the hybrid boundary condition.

The spanwise surface heating profiles taken at the center of the roughness are shown in Figure 5.18(b). The spanwise location of the local maximum in the surface heating profiles is nearly identical among the solutions, and the maximum heating occurs just to right of the roughness centerline at $z = 0$ m. This indicates that the streak of maximum heating along the top of the roughness predicted by the solutions is located forward of the crest on the windward side. The profile to the left of the centerline ($-z$ direction) indicates a local minimum, corresponding to the recirculation region discussed in Section 5.3, and a local maximum corresponding to the leading edge vortex.

The peak heating caused by this leading edge vortex is shown in the profile of Figure 5.18(c), where the vortex heating is centered over $z = -0.04$ m. Again, this location corresponds to the peak vortex heating predicted by the *hybrid* solution. It is interesting to note that the heating profiles predicted by the CFD no-slip solution and hybrid solution are very similar within this region. In fact, the peak vortex heating from the CFD no-slip solution occurs

slightly farther downstream, but is within 2% of the value predicted by DSMC (Table 5.3, highlighted in red), while the CFD slip solution is in better agreement to the DSMC peak heating on the roughness (Table 5.3, highlighted in blue). The heating profiles at this streamwise location show a second local maximum near $z = 0.05 \text{ m}$. This corresponds to the heating over the trailing edge of the roughness.

The final heating profiles are acquired at a location $10k$ downstream of the roughness center (Figure 5.18(d)). The maximum in the heating profiles is due to the leading edge vortex, where the CFD and hybrid solutions predict nearly the same magnitude of surface heating. Towards the centerline, the hybrid solution indicates comparatively high heating in the wake, which is evident in the surface contours from Figure 5.16. The heating downstream of the trailing edge vortex (centered over $z = 0.05 \text{ m}$) is more pronounced in the CFD solutions, while the trailing edge streak in the hybrid solution is somewhat masked by the surrounding surface heating in the wake.

The results obtained from this analysis are quantified in Table 5.3. The first group of data indicate the peak heating on the roughness (referred to as ‘Roughness Peak’) and downstream of the leading edge due to the vortex heating (referred to as ‘Vortex Peak (LE)’). The peak heating values are reported for each solution method (CFD no-slip/slip and hybrid) and are reported in units of $[W/m^2]$. The relative difference between the CFD slip and no-slip peak heating values (roughness and vortex) are also reported in parentheses behind the CFD slip absolute surface heating value. The CFD slip wall condition

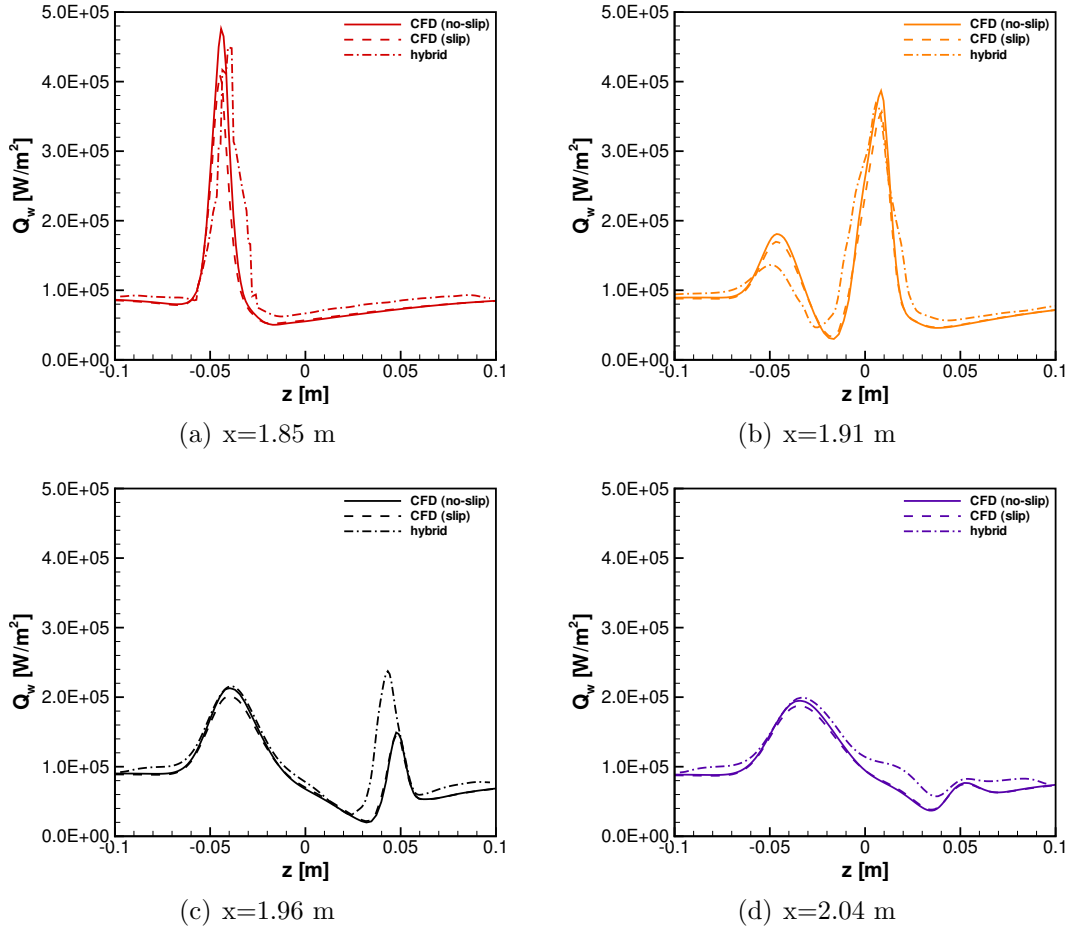


Figure 5.18: Spanwise profiles of surface heating taken at various streamwise locations for asymmetric roughness at 80 km , generated from CFD (no-slip and slip wall) and hybrid solutions. Profiles highlight (a) peak heating on roughness, (b) heating profile at roughness center, (c) peak vortex heating in wake and (d) heating profile in wake. Profile colors correspond to schematic of Figure 5.17 (yellow is replaced by black).

consistently predicts lower surface heating, both in the peak heating regions (first data group) and at the streamwise locations of the heating profiles shown in the lower portion of the table.

The relative differences between the CFD no-slip and slip peak heating values (roughness and vortex) are reported in parentheses (respectively) behind the hybrid absolute surface heating value. It is observed that the CFD slip solution is in better agreement with the peak roughness heating predicted by the hybrid solution, but the CFD no-slip solution provides a closer prediction in heating due to the leading edge vortex. The *peak* heating of the trailing edge vortex is not reported due to the limited downstream distance of the hybrid solution, but the local heating value due to the trailing edge vortex is reported in Table 5.3 at the location $10k$ downstream of the roughness.

5.4.3 Flowfield comparisons at 60 km

The next set of results presents a comparison of the CFD and hybrid solutions for the asymmetric roughness geometry at 60 km . Recall from Section 5.2.1 that the asymmetric roughness geometry in the high and low altitude cases are scaled uniformly such that the roughness heights are one-quarter of the thermal boundary layer thickness, while all other geometric ratios remain the same. Again, only results from the analysis of the CFD slip wall and hybrid solutions are presented.

Comparisons of the velocity field are presented in Figure 5.19 for the wake flow at a location approximately $7k$ downstream of the roughness cen-

Table 5.3: Total surface heating (asymmetric geometry (80 km))

	Roughness Peak [W/m^2]	Vortex Peak (LE) [W/m^2]
CFD (no-slip)	5.38×10^5	2.13×10^5
CFD (slip)	4.79×10^5 (−11.0%)	2.02×10^5 (−5.2%)
Hybrid	4.50×10^5 (−16.4%, −6.1%)	2.17×10^5 (+1.9%, +7.4%)
$x = 1.85 \text{ m}$	Roughness [W/m^2]	Vortex (LE) [W/m^2]
CFD (no-slip)	4.76×10^5	—
CFD (slip)	4.10×10^5	—
Hybrid	4.49×10^5	—
$x = 1.91 \text{ m}$	Roughness [W/m^2]	Vortex (LE) [W/m^2]
CFD (no-slip)	3.86×10^5	1.81×10^5
CFD (slip)	3.54×10^5	1.69×10^5
Hybrid	3.75×10^5	1.37×10^5
$x = 1.96 \text{ m}$	Roughness [W/m^2]	Vortex (LE) [W/m^2]
CFD (no-slip)	1.48×10^5	2.12×10^5
CFD (slip)	1.44×10^5	2.01×10^5
Hybrid	2.41×10^5	2.17×10^5
$x = 2.04 \text{ m}$	Roughness [W/m^2]	Vortex (LE/TE) [W/m^2]
CFD (no-slip)	—	1.95×10^5 / 7.66×10^4
CFD (slip)	—	1.87×10^5 / 7.52×10^4
Hybrid	—	1.99×10^5 / 8.25×10^4

ter. The figures are oriented looking downstream in the $+x$ direction. The streamwise velocity contours are shown in Figure 5.19 (a). The field contours represent the hybrid solution, and the CFD values are shown by the contour lines. The general structure in the wake is similar to the 80 km case presented earlier at a location 10k downstream, but the high and low speed regions centered over $z = \pm 0.02m$ appear more pronounced at this lower altitude. In both solutions, the wake flow produced by the roughness indicates high-speed flow which penetrates toward the wall behind the leading edge ($z \approx -0.02 \text{ m}$),

and to a lesser extent in the flow behind the trailing edge ($z \approx 0.03 \text{ m}$). In between these regions, low speed flow is being pushed upward away from the wall forming a streak of low speed flow in the wake centered over $z = 0.02 \text{ m}$. The CFD solution (line contours) again predicts a slightly wider low speed streak compared to the hybrid solution.

The counter-rotating vortices that originate from the leading and trailing edges of the roughness are visualized by isocontours of Q in Figure 5.19 (b). The CFD vortex pairs are shown by the black isocontours, and the hybrid vortices are shown in red. The sense of rotation of these vortices is indicated by the sets of arrows, and the roughness geometry is shown in gray at this downstream location for reference. The vortex pairs from both CFD and DSMC are represented by isocontours of $Q = 6.0 \times 10^6$, and the vortices generated by the roughness are generally stronger at this low altitude condition.

The relative strength of the vorticity in the wake predicted by the hybrid and CFD solutions are similar in this case, but the span of the CCW leading edge vortex in the wake of the roughness is significantly greater than the CFD solution. The trailing edge vortices predicted by both solutions are considerably stronger at this altitude. The position of the CFD and hybrid vortex pairs are very similar, but the CFD trailing edge vortices are observed to be stronger than the hybrid vortices. Although the trailing edge vortices are weak in comparison to the leading edge vortex pair, the difference in the relative strength of these trailing edge vortices predicted by CFD and DSMC are found to have a measurable impact on the surface heating in the wake.

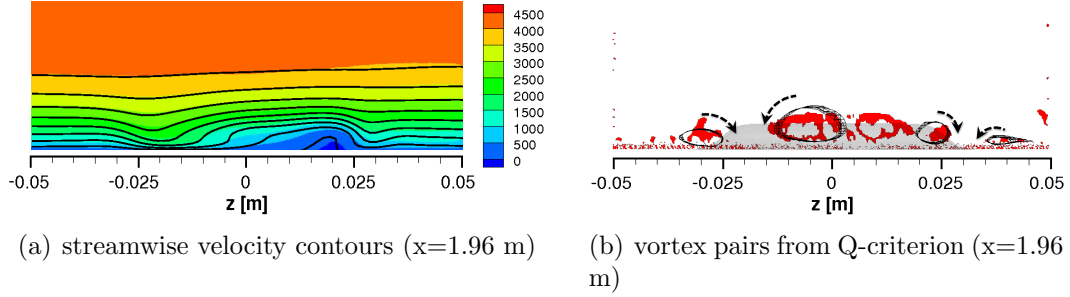


Figure 5.19: Flow features in wake of asymmetric roughness (60 km altitude) at $x = 1.96$ m. (a) Streamwise velocity contours from hybrid solution (contour flood) and CFD slip-wall solution (contour lines). (b) Vortex pairs determined from Q-criterion. Vortices are shown as isocontours of $Q = 6.0 \times 10^6$ for both CFD (black) and for hybrid (red) solutions, and the roughness (gray) is shown for reference. Note that the span of the CCW leading edge vortex is greater in the hybrid solution.

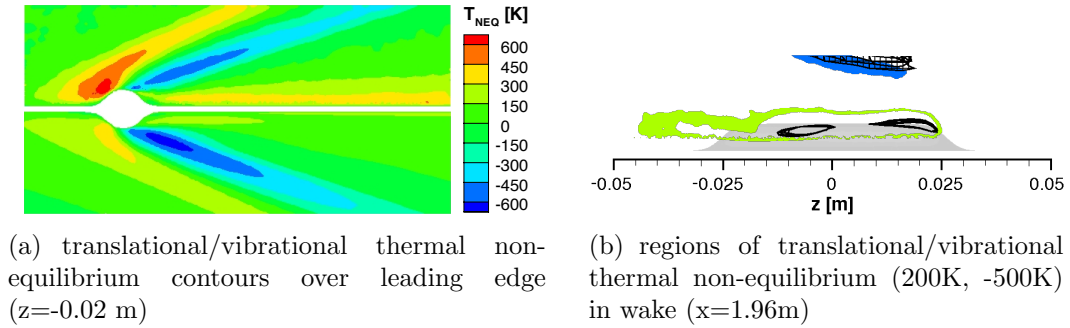


Figure 5.20: Translational/vibrational thermal non-equilibrium in flow surrounding roughness at 60 km. (a) Thermal non-equilibrium contours from hybrid solution (top) and CFD slip-wall solution (bottom) taken at the roughness leading edge $z = -0.02$ m. Contours indicate the difference between translational and vibrational temperatures, where $T_{NEQ} = T_{tr} - T_{vib}$. (b) Isocontours of thermal non-equilibrium in the wake, taken at a location $7k$ downstream of roughness. Colored isocontours (levels in (a)) represent hybrid solution, black represent corresponding CFD solution.

The translational/vibrational thermal non-equilibrium in the flow predicted by the hybrid and CFD slip wall solutions are presented next in Figure 5.20(a) and (b). The contours in Figure 5.20 (a) show the difference in $[K]$ in the translational and vibrational temperatures in the flow. The hybrid solution is again shown on top, and the CFD solution is mirrored on the bottom for comparison. This slice is taken at a spanwise location at the leading edge of the roughness, ($z = -0.02\text{ m}$). At this lower altitude, the translational/vibrational non-equilibrium found in the bow shock region is generally weaker than in the 80 km case, but the non-equilibrium in the expansion region is slightly stronger here. The hybrid solution again predicts higher vibrational non-equilibrium in the bow shock region and in the wake of the roughness compared to the CFD solution. In the expansion region that forms aft of the roughness (indicated by the blue contours), the CFD solution predicts slightly greater vibrational non-equilibrium. A comparison of the thermal non-equilibrium in the wake at a location $7k$ downstream of the roughness center is provided in Figure 5.20 (b). The hybrid solution shows a greater spanwise extent of thermal non-equilibrium near the wall compared to the CFD solution, although the non-equilibrium here is quite weak. The expansion region above (blue contours) is shown above.

5.4.4 Local surface heating at 60 km

The surface heat flux predicted by the CFD and hybrid solutions are presented in Figure 5.21(a)-(c). The flow in these figures is again in the gen-

eral x -direction, and the contours represent the local surface heating on the roughness and in the wake. The baseline heating for this lower altitude case was approximately $Q_0 = 1.1 \times 10^5$ $[W/m^2]$, or 17% greater than the baseline heating in the high altitude case. The windward side of the roughness again experiences the highest surface heating, particularly the leading edge region, and the heating drops off gradually along the crest of the roughness toward the trailing edge. The presence of the roughness has a more pronounced impact on the surface heating upstream of the roughness in the CFD solutions. The surface heating in the wake of the roughness is again qualitatively similar among the CFD and hybrid solutions. All of the solutions indicate that the most substantial heating in the wake is due to the leading edge vortex, but the hybrid solution indicates a wider heating footprint due to the leading edge vortex. The heating due to the trailing edge vortex is more prominent in the CFD solutions; the same observation was made in the high altitude cases, but the heating augmentation in the trailing edge wake region is enhanced at this lower altitude.

The total surface heating is again extracted at several streamwise locations from the CFD and hybrid solutions, both over the roughness and in the wake, as indicated schematically in Figure 5.17. Note that the roughness is still centered over $x = 1.91$ m and $z = 0$ m , but the spanwise and streamwise axes shown in this figure correspond to the high altitude case. The spanwise surface heating profiles are compared at locations of peak heating on the roughness, the center of the roughness, the peak heating in the wake and at a location

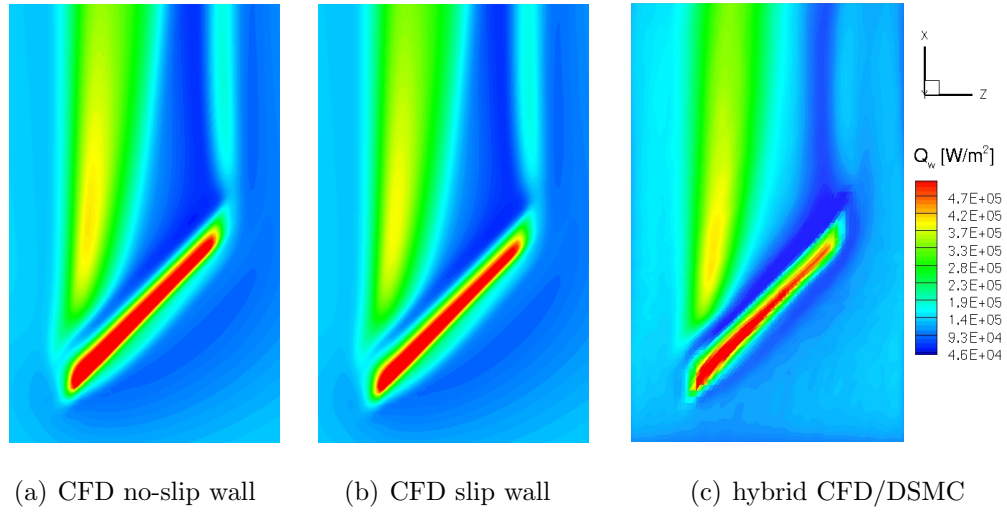


Figure 5.21: Surface heating contours generated by asymmetric roughness at 60 *km* from (a) CFD no-slip wall (b) CFD slip wall and (c) hybrid solutions. General flow direction is from bottom to top.

10*k* downstream of the roughness center (Figure 5.17, red, orange, yellow and purple profiles).

The corresponding spanwise profiles are presented in Figure 5.22 (a)-(d). To facilitate comparison between these results and the high altitude results, the low altitude profiles have been normalized by the baseline heating value $Q_0 = 1.1 \times 10^5 [W/m^2]$ and are shown by the dark lineplots as the ratio Q_w/Q_0 . The high altitude profiles from Section 5.4.2 have been normalized by the corresponding baseline heating value $Q_0 = 9.1 \times 10^4 [W/m^2]$ and are presented as the faded lineplots. CFD no-slip surface heating is represented by the solid line, the slip surface heating is shown by the dashed line, and the hybrid solution is shown as the dash-dotted line, and all profiles are provided over the spanwise distance normalized by the corresponding roughness height,

z/k .

The first set of profiles in Figure 5.22(a) are extracted at the streamwise location of peak surface heating predicted by the *hybrid* solution. The heating profiles from the low altitude case are qualitatively very similar to the high altitude profiles, but the heating augmentation is nearly seven times the baseline heating, whereas the high altitude case shows a heating augmentation on the roughness of approximately five times the baseline value. The peak roughness and vortex heating values corresponding to each low altitude solution are presented in Table 5.4. The maximum peak heating occurring on the roughness predicted by the hybrid solution is 18% less than the CFD no-slip value, and 11% less than the CFD slip value. The CFD slip solution again provides a better approximation to the peak heating on the roughness, similar to the findings in Section 5.4.2, although the overall difference in heating between the hybrid/CFD solutions has increased slightly.

The surface heating profiles in Figure 5.22(b) show the spanwise heating profile through the roughness center. Similar to the high altitude case, the low altitude profiles indicate that the maximum heating on the roughness occurs slightly forward of the crest of the roughness, as indicated by the local maximum which occurs to the right of the roughness centerline. The low altitude CFD solutions show a small bump in the heating profile at $z/k \approx 2.5$, which indicates the presence of a weak vortex near the wall just upstream of the roughness. This feature is not observed in the low altitude hybrid solution.

The peak heating in the wake caused by the leading edge vortex is

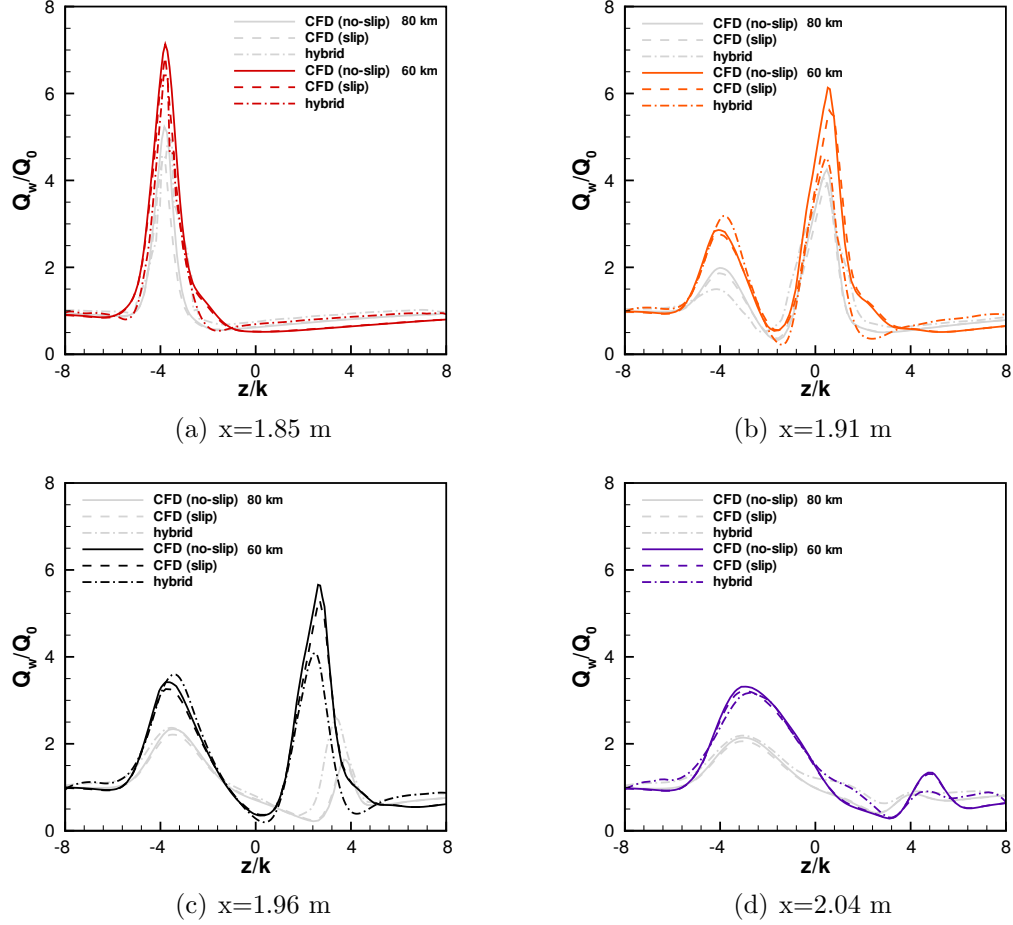


Figure 5.22: Spanwise profiles of surface heating taken at various streamwise locations for asymmetric roughness at 60 km, generated from CFD (no-slip and slip wall) and hybrid solutions. Profiles from 80 km case are presented for comparison, and all profiles are normalized by the corresponding baseline heating values. Profiles highlight (a) peak heating on roughness, (b) heating profile at roughness center, (c) peak vortex heating in wake and (d) heating profile in wake. Profile colors correspond to schematic of Figure 5.17 (yellow is replaced by black).

Table 5.4: Total surface heating (asymmetric geometry (60 km))

	Roughness Peak [W/m^2]	Vortex Peak (LE) [W/m^2]
CFD (no-slip)	8.56×10^5	3.92×10^5
CFD (slip)	7.86×10^5 (−8.2%)	3.76×10^5 (−4.1%)
Hybrid	6.95×10^5 (−18.8%, −11.58%)	4.01×10^5 (+2.3%, +6.6%)
$x = 1.88 \text{ m}$	Roughness [W/m^2]	Vortex (LE) [W/m^2]
CFD (no-slip)	7.79×10^5	—
CFD (slip)	7.47×10^5	—
Hybrid	6.95×10^5	—
$x = 1.91 \text{ m}$	Roughness [W/m^2]	Vortex (LE) [W/m^2]
CFD (no-slip)	6.73×10^5	3.14×10^5
CFD (slip)	6.14×10^5	3.04×10^5
Hybrid	4.91×10^5	3.57×10^5
$x = 1.92 \text{ m}$	Roughness [W/m^2]	Vortex (LE) [W/m^2]
CFD (no-slip)	6.21×10^5	3.76×10^5
CFD (slip)	5.80×10^5	3.58×10^5
Hybrid	4.49×10^5	3.99×10^5
$x = 1.98 \text{ m}$	Roughness [W/m^2]	Vortex (LE/TE) [W/m^2]
CFD (no-slip)	—	3.64×10^5 / 1.47×10^5
CFD (slip)	—	3.53×10^5 / 1.43×10^5
Hybrid	—	3.56×10^5 / 1.25×10^5

shown in the profile of Figure 5.22(c), where the vortex heating is centered over $z/k \approx -4$. Again, this location corresponds to the peak leading edge vortex heating predicted by the *hybrid* solution. Comparison of this value to the CFD no-slip and slip solutions in Table 5.4 shows that again, the hybrid solution predicts slightly higher heating due to the leading edge vortex.

The final heating profiles are acquired at a location $10k$ downstream of the roughness center (Figure 5.22(d)). The maximum in the heating profiles at $z/k \approx -4$ is due to the leading edge vortex. Towards the centerline, the

hybrid solution indicates comparatively high heating in the wake, which was also observed in the high altitude case. The heating downstream of the trailing edge vortex (centered over $z/k \approx 4.5$) is significantly more pronounced in the CFD solutions, while the trailing edge streak in the hybrid solution appears to blend in with the surrounding surface heating in the wake. However, in comparison to the leading edge vortex heating, the trailing edge vortex is relatively weak.

5.5 Symmetric Geometry Configuration

5.5.1 Flowfield comparisons at 80 km

This final set of results presents a comparison of the CFD and hybrid solutions for the symmetric roughness geometry at 80 *km*. Recall from Section 5.2.1 that the hybrid solution of the symmetric roughness is obtained on a half-span domain and utilizes a specular (symmetry) boundary condition along the roughness centerline.

Comparisons of the velocity field are presented in Figure 5.23 for the wake flow at a location $5k$ downstream of the roughness center. The figures are oriented looking downstream in the $+x$ direction. The streamwise velocity contours are shown in Figure 5.23(a). The field contours represent the hybrid solution, and the CFD values are shown by the contour lines. The velocity deficit in the wake flow is positioned over the roughness centerline at $z = 0$ *m*, with high-speed flow penetrating toward the wall on either side at $z = \pm 0.03$ *m*. The CFD solution (line contours) again predicts a slightly wider low

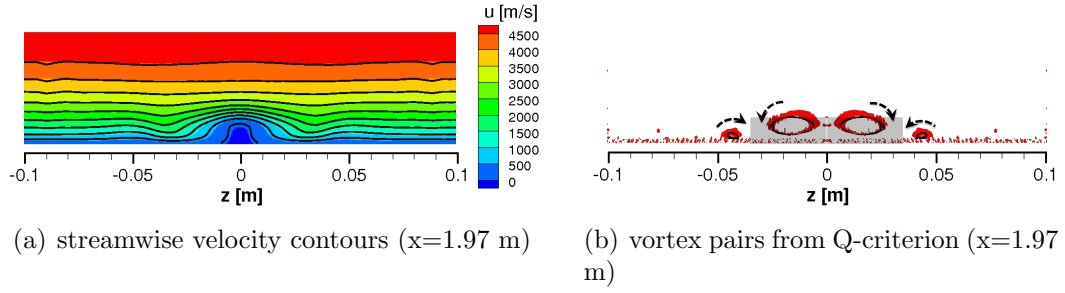


Figure 5.23: Flow features in wake of symmetric roughness (80 km) at $x = 1.97\text{ m}$. (a) Streamwise velocity contours from hybrid solution (contour flood) and CFD slip-wall solution (contour lines). (b) Vortex pairs determined from Q-criterion. Vortices are shown as isocontours of $Q = 7.0 \times 10^7$ for CFD (black) and $Q = 1.0 \times 10^8$ for hybrid (red) solutions, and the roughness (gray) is shown for reference. Note that the positions of vortex cores are similar, but the hybrid vorticity (relative to the strain rate) is stronger.

speed streak compared to the hybrid solution, but this difference is observed to be more pronounced in the asymmetric roughness cases presented in Sections 5.4.1 and 5.4.3.

The high- and low-speed streaks that are generated by the symmetric roughness correspond to a pair of counter-rotating vortices that form off of the spanwise corners of the roughness. These vortex pairs are visualized by isocontours of Q in Figure 5.23(b). The CFD vortex pairs are shown by the black isocontours, and the hybrid vortices are shown in red. The sense of rotation of these vortices is indicated by the sets of arrows, and the roughness geometry is shown in gray at this downstream location for reference. The positions of these vortex pairs in the wake of the roughness are nearly identical, and in particular it is noted that the stronger vortices located nearest to the roughness centerline have nearly the same spanwise extent. The difference in

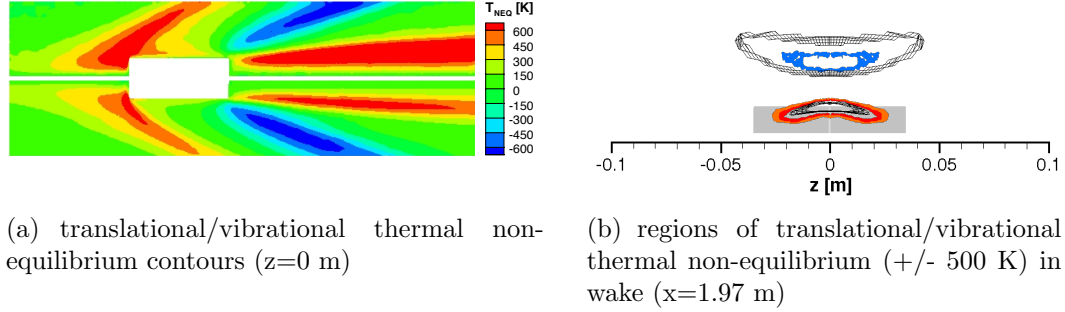


Figure 5.24: Translational/vibrational thermal non-equilibrium in flow surrounding symmetric roughness at 80 km . (a) Thermal non-equilibrium contours from hybrid solution (top) and CFD slip-wall solution (bottom) taken at the roughness leading edge $z = 0$ m . Contours indicate the difference between translational and vibrational temperatures, where $T_{NEQ} = T_{tr} - T_{vib}$. (b) Isocontours of thermal non-equilibrium in the wake, taken at a location $5k$ downstream of roughness. Colored isocontours (following levels in (a)) represent hybrid solution, black represent corresponding CFD solution.

the spanwise extent of the CCW leading edge vortices that was observed in the asymmetric roughness case is not found here. The analysis of the CFD and hybrid solutions using the Q-criterion indicates that the vortices (near the centerline and closer to the wall) generated by the hybrid solution are observed to be stronger.

The translational/vibrational thermal non-equilibrium in the flow predicted by the hybrid and CFD slip wall solutions are presented next in Figure 5.24(a) and (b). The contours in Figure 5.24(a) show the difference ($[K]$) in the translational and vibrational temperatures in the flow for the hybrid solution (top), and the CFD solution (bottom). This slice is taken at a spanwise location at the leading edge of the roughness, ($z = 0$ m). The degree of vibrational non-equilibrium in the bow shock region is similar to the asymmetric

roughness presented in Section 5.4.1. However, the non-equilibrium in the expansion region and in the wake of the symmetric roughness near the wall is noticeably stronger in this case (Figure 5.24(a) compared to Figure 5.15(a)).

A comparison of the thermal non-equilibrium in the wake at a location $5k$ downstream of the roughness center is provided in Figure 5.24(b). The spanwise extent of thermal non-equilibrium predicted by the hybrid solution near the wall (red contour) is slightly greater than the CFD solution, in contrast to the asymmetric geometry (Figure 5.15(b)). However, the overall *differences* between the CFD and hybrid solutions in terms of predicted thermal non-equilibrium are again on the order of 5%, and so the effects of thermal non-equilibrium on the overall flowfields are quite subtle.

5.5.2 Local surface heating at 80 km

The surface heat flux predicted by the CFD and hybrid solutions are presented in Figure 5.25(a)-(c). The flow in these figures is in the general x -direction, and the contours represent the local surface heating on the roughness and in the wake. The baseline surface heating is the same as the high altitude asymmetric value, $Q_0 = 9.1 \times 10^5 [W/m^2]$. The windward edge of the roughness experiences the highest surface heating (particularly the leading corner) and the heating drops off gradually along the crest of the roughness toward the spanwise corners. Similar to the asymmetric geometry, the CFD contours indicate that the roughness has a more widespread impact on the surface heating upstream of the roughness, relative to the hybrid solution.

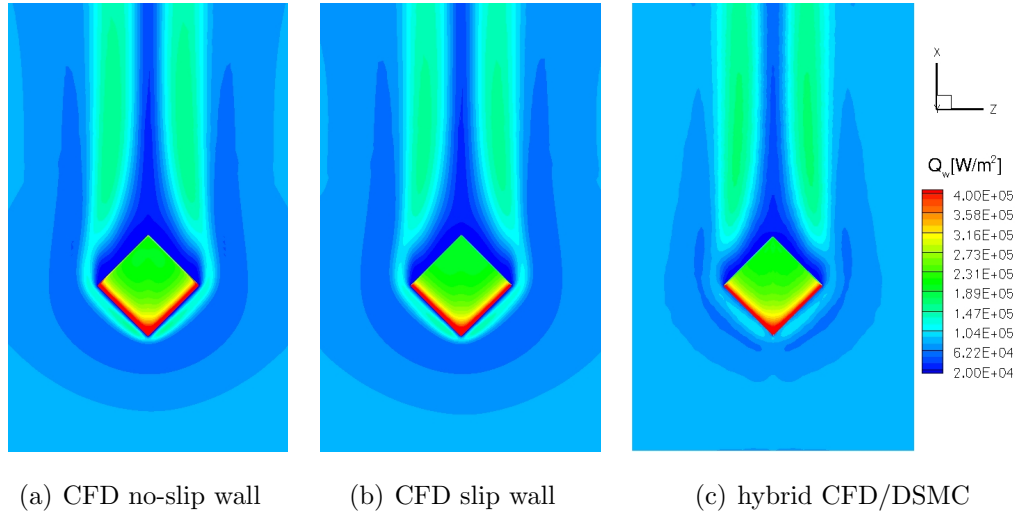


Figure 5.25: Surface heating contours generated by symmetric roughness at 80 km from (a) CFD no-slip wall (b) CFD slip wall and (c) hybrid solutions. General flow direction is from bottom to top.

Immediately upstream of the roughness, the CFD solutions indicate relatively strong vortex heating on either side of the roughness centerline. This vortex pair appears comparatively weak in the hybrid solution, as indicated by the streaks of relatively low heating in front of the roughness. In contrast, the surface heating in the wake of the roughness is generally slightly higher in the hybrid solution.

To quantify these differences, the total surface heating is extracted at several streamwise locations from the CFD and hybrid solutions, both over the roughness and in the wake, as indicated schematically in Figure 5.26. In particular, the spanwise surface heating profiles are compared at locations of peak heating on the roughness, the center of the roughness, at a location $5k$ downstream of the roughness center and the peak heating in the wake (Figure

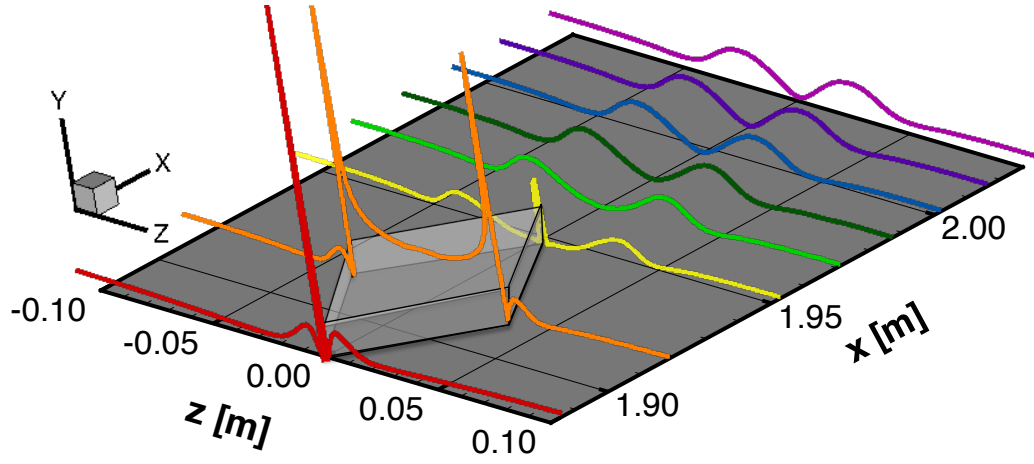


Figure 5.26: Spanwise profiles of surface heating acquired at various stream-wise locations for symmetric roughness. Profiles highlight peak heating on roughness (first spanwise profile in red) as well as vortex heating in wake in the profiles downstream of the roughness (shown schematically in gray).

5.17, red, orange, green and blue profiles).

These spanwise profiles are presented in Figure 5.27 (a)-(d). CFD no-slip surface heating is represented by the solid line, the slip surface heating is shown by the dashed line, and the hybrid solution is shown as the dash-dotted line. The first set of profiles (Figure 5.27(a)) are extracted at the streamwise location of peak surface heating predicted by the *hybrid* solution, although the location of peak heating on this roughness geometry was very similar among the solutions. The heating profile is extremely peaked due to the small radius of curvature on the leading edge rounded corner, which has a profound effect on the peak heating values reported by each of the solutions in Table 5.5. The CFD no-slip solution predicts the highest peak heating on the rounded corner,

while the CFD slip wall peak heating is nearly 40% less than the no-slip value. In comparison to the hybrid solution, it is observed that the DSMC peak heating is approximately 14% lower than the slip wall value. Throughout each of the cases examined, it is found that the CFD slip wall solution provides the closest agreement to the hybrid solution peak surface heating on the roughness.

Table 5.5: Total surface heating (symmetric geometry (80 km))

	Roughness Peak [W/m^2]	Vortex Peak [W/m^2]
CFD (no-slip)	2.70×10^6	1.58×10^5
CFD (slip)	1.66×10^6 (−38.5%)	1.53×10^5 (−3.2%)
Hybrid	1.43×10^6 (−47.0%, −13.8%)	1.69×10^5 (+7.0%, +10.5%)
$x = 1.88 \text{ m}$	Roughness centerline [W/m^2]	Vortex [W/m^2]
CFD (no-slip)	2.70×10^6	1.36×10^5
CFD (slip)	1.66×10^6	1.23×10^5
Hybrid	1.43×10^6	1.21×10^5
$x = 1.91 \text{ m}$	Roughness centerline [W/m^2]	Vortex [W/m^2]
CFD (no-slip)	2.27×10^5	1.26×10^5
CFD (slip)	2.19×10^5	1.19×10^5
Hybrid	2.37×10^5	9.88×10^4
$x = 1.97 \text{ m}$	Wake centerline [W/m^2]	Vortex [W/m^2]
CFD (no-slip)	2.09×10^4	1.42×10^5
CFD (slip)	2.31×10^4	1.38×10^5
Hybrid	2.96×10^4	1.54×10^5
$x = 2.00 \text{ m}$	Wake centerline [W/m^2]	Vortex [W/m^2]
CFD (no-slip)	2.10×10^4	1.43×10^5
CFD (slip)	2.77×10^4	1.52×10^5
Hybrid	3.60×10^4	1.69×10^5

To either side of the roughness centerline in Figure 5.27(a), a second local maximum in the peak heating occurs in the heating profiles. This is due to the vortex heating found just upstream of the roughness at the wall.

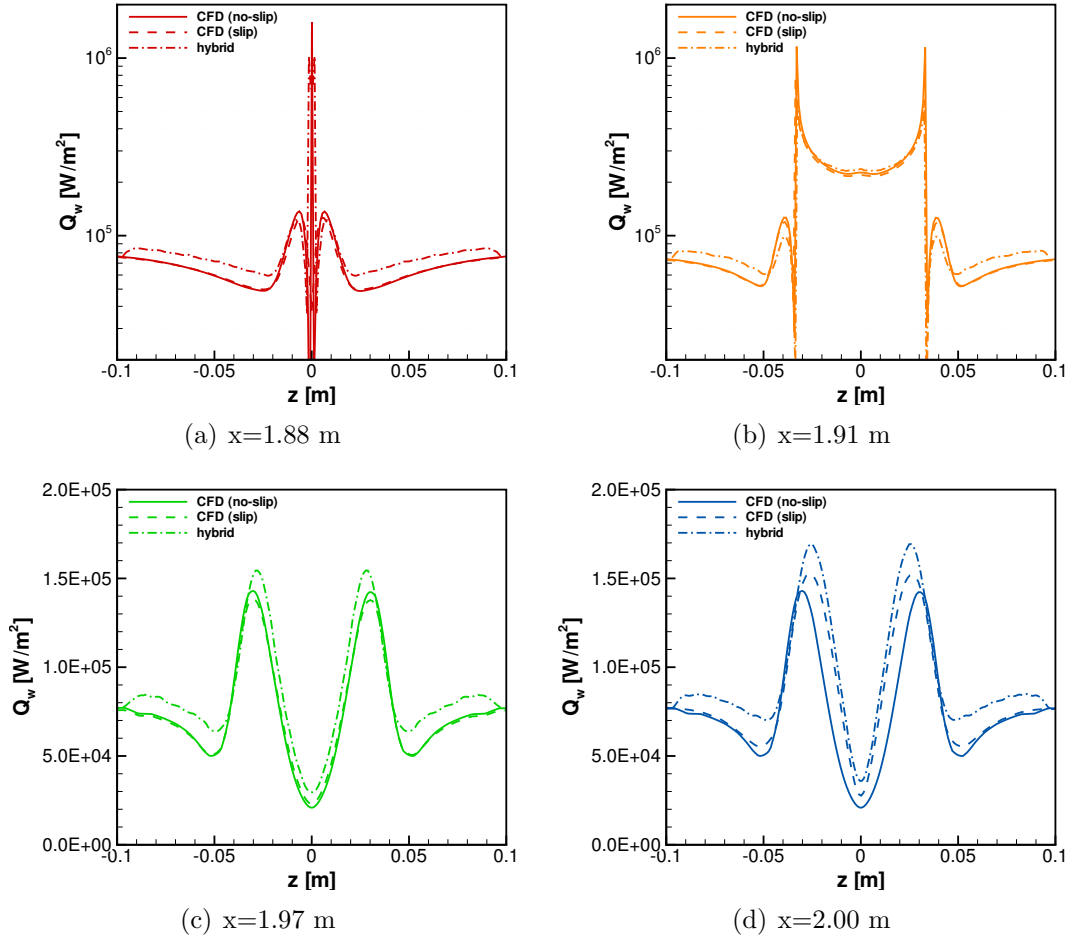


Figure 5.27: Spanwise profiles of surface heating taken at various streamwise locations for symmetric roughness at 80 km, generated from CFD (no-slip and slip wall) and hybrid solutions. Profiles highlight (a) peak heating on roughness, (b) heating profile at roughness center, (c) peak vortex heating in wake and (d) heating profile in wake. Profile colors correspond to schematic of Figure 5.17.

These peak vortex heating values corresponding to each solution are presented in Table 5.5. The local maximum heating values (on the roughness/wake centerline and on the vortex heating streaks) at each streamwise location are also provided.

The second set of profiles show the heating taken at the streamwise location corresponding to the roughness center (Figure 5.27(b)). The peaks in the heating profiles (centered over $z \approx \pm 0.03 \text{ m}$) correspond to the heating over the rounded corners of the roughness; these values have dropped nearly an order of magnitude from the surface heating on the leading corner of the roughness, as seen from the values reported in Table 5.5, at stations $x = 1.88 \text{ m}$ and $x = 1.91 \text{ m}$. The vortex heating along the side of the roughness at the wall is found to decrease slightly in each of the solutions, with the hybrid solution predicting the lowest vortex heating in both locations ($x = 1.88 \text{ m}$ and $x = 1.91 \text{ m}$).

The next set of profiles are taken at a streamwise location corresponding to $5k$ downstream of the roughness center, and includes portions of the recirculating wake region between $z = \pm 0.02 \text{ m}$. At this streamwise location ($x = 1.97 \text{ m}$), the peak heating predicted by the hybrid solution already exceeds the CFD no-slip heating value, both at the wake centerline and within the peak vortex heating region. This trend continues through the remainder of the hybrid domain. At the downstream location of $x = 2.00 \text{ m}$, the hybrid solution reaches a peak value in the vortex heating of $1.69 \times 10^5 \text{ [W/m}^2\text{]}$. The hybrid solution again predicts a higher surface heating in the wake due to

vortex heating, 7% higher than the CFD no-slip value and almost 11% higher than the CFD slip value. It is interesting to note that in all cases examined, the CFD no-slip solution provides better agreement to the hybrid solution in the vortex heating regions, which is contrary to the finding that the CFD slip solution provides better agreement for peak heating on the roughness.

5.6 Summary

The purpose of this chapter was to examine in detail the importance of non-equilibrium processes when modeling hypersonic boundary layer flow over discrete surface roughness. These studies has two principal objectives. The first was to identify and quantify the effects of rarefaction through comparison of several macroscopic quantities (flowfield and surface) from CFD and hybrid solutions. The quantities examined in this work included the disturbance velocity field through the Q -criterion, the translational/vibrational thermal non-equilibrium in the flow surrounding the roughness, and the total heating to the surface. The second objective was to gain insight regarding the mechanism by which the non-equilibrium effects are manifested. This was accomplished through detailed comparison of the CFD (no-slip and slip wall conditions) with the hybrid solutions. The surface roughness geometries and flow conditions examined in this work were selected to allow examination of a variety of characteristic geometric and flow length scales, including roughness radius of curvature and molecular mean free path.

Several important observations were made from these investigations.

The disturbance velocity field generated by the CFD solutions (using either no-slip or slip wall conditions) produced a more prominent velocity deficit region in the wake flow compared to the hybrid solution. This observation was most apparent for the asymmetric roughness geometries (either at high or low altitudes), but was more subtle in the case of the symmetric roughness. Recirculation regions developed immediately downstream of the roughness, after which the disturbed flow organized into streamwise-oriented vortices in the wake. The comparison of these vortices, identified in both CFD and hybrid solutions through the Q -criterion, provides insight regarding the non-equilibrium mechanisms involved in these problems. The streamwise vortices that form in the wake of the asymmetric roughness are found to be slightly stronger in the hybrid solution compared to the CFD solutions. Moreover, the counter-clockwise (CCW) vortex generated from the leading edge has a larger spanwise extent in the hybrid solution, for both high and low altitude cases. The streamwise vortices in the wake of the symmetric roughness are also slightly stronger in the hybrid solution. The strength and span of these vortices in the wake of the roughness have a direct impact on the near-wall gradients and surface heating in the wake. In fact, the hybrid peak surface heating downstream of the roughness is found to be higher than the predicted CFD (both no-slip and slip) values as a result.

The translational/vibrational thermal non-equilibrium was also examined and compared among the solutions, with particular emphasis on the non-equilibrium in the bow shock, expansion and in the wake. Although the hybrid

solution predicted slightly higher vibrational non-equilibrium in the bow shock and in the wake compared to CFD, the differences are quite small. From these investigations, the impact of vibrational non-equilibrium is considered negligible, and it is not possible to identify a distinct mechanism by which vibrational non-equilibrium affects the flowfield solution.

The surface heating predicted by the CFD (no-slip and slip) and hybrid solutions were examined in detail, and the results from these comparisons were tabulated in Tables 5.3-5.5. The hybrid solution consistently predicted a lower peak heating on the surface of the roughness compared to the CFD values, and higher peak heating in the wake of the roughness due to vortex heating. Since several geometric parameters and flow conditions were examined in this chapter, the behavior of the surface heating on the roughness and in the wake in relation to the degree of rarefaction of the flow are summarized in Figures 5.28 and 5.29 below.

The first figure (Figure 5.28) presents the peak heating on the surface of the roughness, normalized by the respective baseline heating value (Q_w/Q_o) for the three cases examined. These heating values are plotted as a function of the local Knudsen number, defined as the hard sphere molecular mean-free-path in the shock layer, denoted as $\lambda'_{k,HS}$, divided by the roughness radius of curvature, r . The CFD no-slip wall, CFD slip wall and hybrid solutions are shown with the solid lines, and the relative difference (%) between the *hybrid* and *CFD slip wall* solutions as a function of local Knudsen number is shown in the dashed line. The hybrid solution consistently predicts a lower peak surface heating on

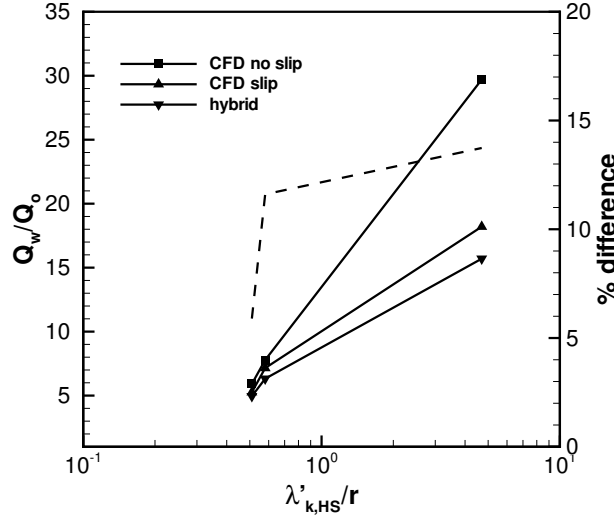


Figure 5.28: Roughness peak heating as a function of local Knudsen number. Dashed line indicates the relative difference (expressed as a percentage) between CFD slip and hybrid solutions.

the roughness for the three Knudsen numbers examined. The general trend indicates that the relative difference between the peak heating predicted by the CFD slip and hybrid solutions increases with increasing Knudsen number, although more points would be necessary to establish a stronger relationship.

The second figure (Figure 5.29) presents the peak heating in the wake of the roughness due to vortex heating, normalized by the respective baseline heating value (Q_w/Q_o) for the three cases examined. These heating values are plotted as a function of Knudsen number. The Knudsen number used here is defined as the hard sphere molecular mean-free-path based on flow conditions at the roughness height of an undisturbed boundary layer, $\lambda_{k,HS}$, divided by the roughness radius of curvature, r . The CFD no-slip wall, CFD slip wall

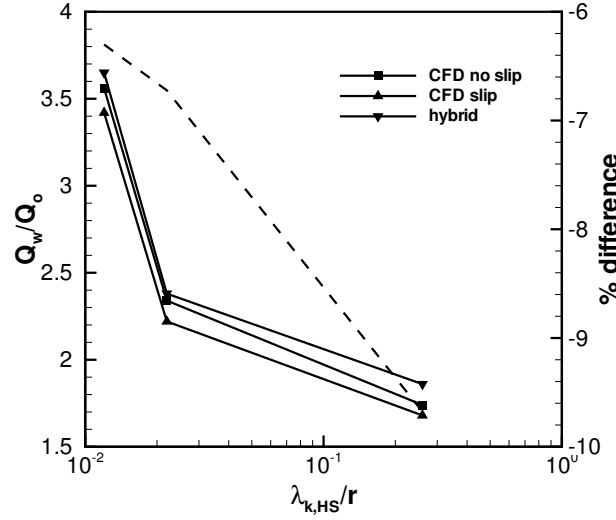


Figure 5.29: Peak heating in the wake as a function of Knudsen number. Dashed line indicates the relative difference (expressed as a percentage) between CFD slip and hybrid solutions.

and hybrid solutions are shown with the solid lines, and the relative difference (%) between the *hybrid* and *CFD slip wall* solutions as a function of Knudsen number is shown by the dashed line. The hybrid solution consistently predicts a higher peak surface heating in the wake for the three Knudsen numbers examined. The general trend indicates that the difference (indicated as a negative percentage since the CFD value is less than hybrid) between the peak heating predicted by the CFD slip and hybrid solutions again increases with increasing Knudsen number.

From the analysis of the cases examined in this work, it is concluded that the non-equilibrium mechanisms at work in the complex flowfield generated by the roughness can not be captured through a slip surface model

alone. While the peak heating on the roughness from the DSMC solution is best approximated using the slip wall condition, the same is not true for the peak heating in the wake. The details by which the disturbance field develops in the non-equilibrium region of the roughness are found to have a measurable impact on the strength and span of the streamwise vortices in the wake as well as the surface heating downstream.

Chapter 6

Conclusions

A summary of this work is presented below, with emphasis on the key principles, methods and observations that were established throughout this work. The major contributions of the research efforts are outlined next, with focus on the two novel hybrid methods that are formulated for general use within the hybrid community. This chapter closes with considerations for future research directions.

6.1 Summary

This work is focused on the development of a hybrid DSMC/CFD solver to examine hypersonic boundary layer flow over discrete surface roughness. The purpose of these investigations is to identify and quantify the non-equilibrium effects that influence the roughness-induced disturbance field and surface quantities of interest for engineering applications. The surface roughness height k considered in this work is comparable to the boundary layer thickness, such that k is up to several hundred mean free paths. In this regime, rarefaction effects are expected to have an impact on the details of the predicted surface flux quantities (shear stress, heat flux), as well as the

disturbance field generated by the surface roughness. To examine this hypothesis, direct simulation Monte Carlo (DSMC) is used to model hypersonic boundary layer flow in the vicinity of a discrete roughness element, while a CFD solver is used to provide the mean-flow solution at the boundary of the DSMC region, in a loosely-coupled hybrid approach. To this end, a new hybrid framework is developed for high-fidelity hybrid solutions involving five-species air hypersonic boundary layer flow applications.

The construction of a consistent hybrid DSMC/CFD framework relies on the fundamental principles established through (Generalized) Chapman-Enskog Theory. This theory establishes the relationship between the DSMC and CFD methods, which provide the molecular and continuum representations of the flowfield. The CFD method, which involves solution of the Navier-Stokes equations, is limited to flows which are near equilibrium, as the Navier-Stokes equations are formulated assuming (*a priori*) that the flow follows a Chapman-Enskog distribution. The DSMC method makes no underlying assumption of the probability distribution function describing the flow, and can therefore be used to accurately model strong non-equilibrium flows. The collision-integrals and the expression for the perturbation are two important principles that are established from Chapman-Enskog theory, and their significance for this hybrid work is discussed in detail. The perturbation formulated from Generalized Chapman-Enskog Theory (discussed in Chapter 3), provides a link between the non-equilibrium macroscopic fluxes determined from CFD, and the non-equilibrium distribution function describing particle

thermal velocities and internal energies in DSMC. The collision-integrals provide a link between the microscopic collision dynamics and the definition of the transport coefficients, as well as the macroscopic transport fluxes.

A novel approach for the generation of particles at a hybrid CFD/DSMC interface is presented for simple gases and gas mixtures with internal degrees of freedom. DSMC particles generated at a hybrid boundary are assigned thermal velocities using a non-equilibrium surface reservoir approach, in which the fluxes of mass, momentum and energy determined from the CFD solution are used to prescribe the appropriate velocity distribution function used in the DSMC particle generation. The non-equilibrium surface reservoir approach is first outlined for a simple (single-species, monatomic) gas, and is then extended to gas mixtures with internal degrees of freedom, in which additional diffusion and internal heat flux terms are included through a rigorous formulation of the perturbation using Generalized Chapman-Enskog Theory. This formulation introduces new breakdown parameters for use in hybrid DSMC/CFD applications, and the new sampling algorithm allows for the generation of DSMC internal energies from the appropriate non-equilibrium distribution for the first time in the literature. The significance of the diffusion, shear stress and heat flux parameters in the perturbation are examined at a hybrid interface for five-species air flows common to engineering applications. The validity of the Chapman-Enskog perturbation at each of these hybrid interfaces is assessed by comparison with the Generalized Chapman-Enskog perturbations. The contribution of the internal heat fluxes to the overall perturbation is found

to be of the same order as the stress tensor components, underscoring the importance of DSMC particle generation from the Generalized Chapman-Enskog distribution.

This work also addressed the consistency of the transport properties achieved through the DSMC collision cross-section models and the transport models employed in CFD. A general approach for achieving consistency in the species diffusion, viscosity and thermal conductivity coefficients between phenomenological VHS/VSS collision cross section models and the SCEBD/Gupta *et al.*-Yos models is outlined for five-species air. The DSMC transport coefficients were approximated from the SCEBD model (diffusion), Chapman-Enskog theory (viscosity and translational thermal conductivity) and Eucken's relation (internal thermal conductivities), and the corresponding collision integrals were determined according to the VHS or VSS collision cross section model. The transport coefficients from the SCEBD and Gupta *et al.*-Yos models were generated using collision integrals computed from more realistic intermolecular potentials. These transport coefficients were considered as the 'standard' values to which the DSMC transport coefficients were fitted by selectively adjusting the VHS/VSS parameters using the Nelder-Mead Simplex Method. Five species air mixtures in chemical equilibrium were examined, and several (prescribed) non-equilibrium conditions were examined.

The transport coefficients generated from the best-fit VHS model parameters were found to be in relatively poor agreement with the SCEBD and Gupta *et al.*-Yos values compared to the VSS model, regardless of the collision

pairing approach used. This underscores the importance of using the VSS model for flows involving gas mixtures, as the scattering exponent α allows for a consistent representation of both the viscosity and diffusion cross sections. In general, the VSS model should be used for conditions in which species diffusion is important, such as flows involving strong normal shocks or chemical reactions/reacting surfaces.

The concepts of the hybrid framework and techniques discussed in Chapters 2-4 are brought together and applied to model hypersonic boundary layer flow over discrete surface roughness. In particular, the hybrid approach is used to provide a detailed non-equilibrium solution in the region surrounding the roughness as well as in the near wake region. The three-dimensional flow-field results are presented for an asymmetric geometry configuration at high and low altitude conditions, and a symmetric geometry configuration which is examined at high altitude conditions. The CFD and hybrid DSMC flowfield solutions from these cases are compared and analyzed, and the importance of non-equilibrium effects are assessed from these results.

Detailed comparisons among the hybrid solution and the CFD no-slip and slip wall solutions were made to examine the differences in surface heating, translational/vibrational non-equilibrium in the flow near the roughness, and the vortex structures in the wake through the Q-criterion. In all cases examined, the hybrid solution predicts a *lower* peak surface heating to the roughness compared to either CFD solution, and a *higher* peak surface heating in the wake due to vortex heating. The observed differences in vortex heating is a

result of the predicted vortex structures which are highlighted using the Q-criterion. The disturbance field modeled by the hybrid solution organizes into a system of streamwise-oriented vortices which are slightly stronger and have a greater spanwise extent compared to the CFD solutions. As a general trend, it was observed that these *differences* in the predicted heating by the hybrid and CFD solutions *increase* with increasing Knudsen number. This trend is found for both peak heating values on the roughness and in the wake.

6.2 Contributions

The objective of this work is to develop a general, consistent hybrid DSMC/CFD approach, with application to hypersonic boundary layer flow over discrete surface roughness. The hybrid approach allows for an efficient yet detailed solution of the nonequilibrium disturbance field generated by the roughness, which is necessary in order to understand and quantify the influence of rarefaction in the multiscale flow application examined in this work. The flow conditions examined are representative of typical laminar boundary layer edge conditions on the shuttle orbiter belly during early stages of a reentry trajectory. Therefore, the hybrid approach presented here has been extended to include effects of species diffusion and heat flux from internal energy modes for application in a five species air mixture. Ionized or chemically reacting flows are not considered in the present work.

Hybrid methods require a careful treatment of the physical models employed in the CFD and DSMC solvers. Although significant modification of the

DSMC solver was required for this hybrid application, this work utilized the existing models available within the DSMC and CFD solvers (where possible). This work introduces an approach for achieving consistency in the transport properties of mass diffusion, viscosity and thermal conductivity between the two solvers, and a consistent approach for vibrational thermal relaxation is also employed. A novel approach for hybrid particle generation is also presented for the five species air mixture, but can be applied for general gas mixtures with internal energy. Additional modifications were made to the DSMC solver to allow for the large scale simulations necessary for the three-dimensional boundary layer flow simulations. The major efforts and contributions of this dissertation are summarized below.

- Devised an approach for achieving consistency in transport properties between DSMC and CFD solvers, including species diffusion, mixture viscosity, and translational and internal thermal conductivities.
- Formulated a novel approach for hybrid particle generation in nonequilibrium flows involving gas mixtures with internal energy, based on Generalized Chapman-Enskog Theory.
- Implemented Millikan and White thermal relaxation rates (with Gimelshein correction factor) and Park's high temperature correction in DSMC solver and libraries.
- Modified DSMC solver to examine influence of near-wall cell population on the predicted surface heat flux.

- Implemented new hybrid particle generation algorithm in DSMC libraries, preprocessors and solvers.
- Modified DSMC libraries, preprocessors and solvers to enable simulations with unprecedented number of simulated particles.
- Generated and compared continuum and hybrid flowfield solutions for various roughness geometries and conditions relevant to aerospace applications.

6.3 Future Considerations

6.3.1 Transport properties: extension to weakly ionized flows

The transport properties in these studies are restricted to the 5-species air gas model. Many re-entry applications however, require consideration of thermochemical non-equilibrium flows at higher enthalpy involving weak ionization. Under these conditions, the 11-species air model would be necessary to account for physical processes due to ion/ion and heavy/ion interactions. The current fitting method (Nelder-Mead) operates on the premise that the transport coefficients are expressed in terms of the collision integrals, which, for neutral gas mixtures (e.g., 5-species air), are strictly a function of temperature. The extension of the approach outlined in Chapter 4 to a weakly ionized 11-species air model would require several modifications to the current fitting method:

- (a) It would be necessary to reformulate the underlying expressions

used in the calculation of the transport coefficients to include ion-neutral, electron-neutral and charged particle (electron-ion, electron-electron and ion-ion) interactions in a way that is consistent with the representation of these interactions in DSMC. Expressions for the transport coefficients/collision integrals involving these interactions are available in the literature [34].

(b) The transport coefficients involving charged particle interactions are expressed in terms of shielded Coulomb collision integrals, which are a function of temperature as well as the electron number density. This dual-dependence introduces an additional challenge in the fitting process, as the fitting must now be conducted over variable temperature and electron number density, in the n -parameter space, where n is the number of collision model parameters. It *may* be possible to reduce this dual-dependence if the collision integrals show a strong dependence on temperature and only a weak dependence on electron number density [53, 75], but this would certainly need to be examined in detail. It may also be possible to conduct the Nelder-Mead fit over both dependencies, but this has not been tested within the Nelder-Mead algorithm.

6.3.2 Finite-rate chemistry

Application of this hybrid approach is currently limited to chemically frozen hypersonic flows, in which it is assumed that all reactions occur on a timescale which is much longer than a characteristic flow time. Future research could extend this hybrid approach to include contributions from chemical reactions. The general issues encountered by including chemistry in a hybrid

solution are conceptually similar to the issues concerning the transport properties: the chemistry models employed by the DSMC and CFD solvers are based on the use of rate coefficients, but the details in the model implementations are fundamentally different between the two solvers. The primary goal of this extension would be to achieve consistency in the chemistry models currently employed by the solvers, and to devise a general hybrid approach that incorporates the effects of chemical reactions in the hybrid boundary condition. After this consistency is established, the next step would be to explore the use of more accurate, high-fidelity thermo-chemical models in the hybrid DSMC/CFD framework that are currently being developed.

The DSMC method considered in this work uses the Total Collision Energy (TCE) model proposed by Bird to determine the probability of a chemical reaction event between colliding particles [2]. The TCE model requires that the reaction rate coefficients, both forward and backward, are specified by a modified Arrhenius form. However, this incorrectly implies that the equilibrium constant, which is given by the ratio of forward and backward rate coefficients from statistical mechanics, may also be expressed in modified Arrhenius form. To address this issue, the backward rate coefficients in TCE are usually fit to the modified Arrhenius form over a modest temperature range, but this approach only approximates the proper backward rate coefficient. Recent work by Boyd [5] presents a simple extension of the TCE model which correctly simulates the backward rates, without use of backward rate coefficient fits. This extension allows for a consistent representation of the forward and backward

reaction rate coefficients in DSMC and CFD solvers, and could be used as a preliminary approach to achieve consistency in the chemistry models.

The final task in the extension of this hybrid approach would be to include the contributions from chemical reactions in the Generalized Chapman-Enskog perturbation. This would allow for the complete description of the distribution function for hybrid particle generation in a non-equilibrium reacting gas mixture. The general form of this perturbation is given in Nagnibeda and Kustova [57], but a detailed formulation would be necessary to express the perturbation in terms of macroscopic quantities obtained from the CFD solution. This formulation would follow along a similar approach outlined in Garcia and Alder [23], and Stephani *et al.* [83], and is expected to produce an additional set of breakdown parameters for a reacting gas mixture.

6.3.3 Comparative Assessment of CFD/Hybrid Solutions through Bi-Global Stability Analysis of Base Flows

Preliminary research efforts have been made toward the investigation of the stability of roughness-induced disturbance fields [32, 33]. The near field of the roughness sets the stage for the downstream behavior and thus requires a careful investigation of numerical resolution of the base flow. The vortex patterns right behind the element form the dominant flow structures and, thus, the basis for the stability properties of the flow far downstream. Chemical and thermal non-equilibrium as well as the conditions at the wall influence the near field of the roughness, resulting in sharp gradients of the flow quantities.

Results from the current work indicate that rarefaction effects modify the vortex structure in the wake relative to the CFD solutions, leading to enhanced heating at the wall. These vortex structures are very relevant for determining the overall stability of the roughness-induced disturbance field. Additional efforts involving bi-global stability analysis of these base flows is an important step to interpreting these observations in the context of roughness-induced transition.

Regarding the high-enthalpy conditions examined here, previous work from the CTR Summer Program found that the temperature field significantly influences the stability behavior [33]. The crossflow-vortex-like leading-edge vortex downstream of an asymmetric roughness (similar to the present study), produces instability modes with growth rates almost as large as in the cold flow case, despite strong wall cooling. The instability of the trailing-edge vortex, however, is completely suppressed by a high-temperature spot that coincides with the region of large velocity gradients as a result of dissipation. Future work involving a careful stability analysis of the CFD and hybrid base flow solutions could provide an additional quantitative assessment of the non-equilibrium effects relevant to this problem.

Appendices

Appendix A

Sampling of the non-equilibrium surface reservoir distributions

The evaluation of the non-equilibrium distribution functions for the surface reservoir in a simple gas (3.6) and a gas mixture with internal energy (3.19) results in velocity distribution functions describing the tangential and normal thermal velocity components of particles entering the computational domain. The tangential components in both cases are described as usual by regular Maxwellian distributions, and velocity components $(\mathcal{C}_y, \mathcal{C}_z)$ may be sampled from this distribution using the Box-Muller method [2, 25].

To sample the distributions describing the normal thermal velocity components, we use an acceptance-rejection approach on the distributions shown in (3.10) and (3.22). For brevity, we present the approach for (3.10), but the same process is used to sample (3.22). An efficient acceptance-rejection sampling on (3.10) is formulated by normalizing this distribution by its maximum value $f_{SR}(C_{x,MAX})$, where $(C_{x,MAX})$ is determined by solving the following for C_x :

$$\begin{aligned}
\frac{d f_{SR}(C_x)}{d C_x} = & \frac{2\beta^2 \exp(-\beta^2 C_x^2) - 4\beta^4 C_x^2 \exp(-\beta^2 C_x^2) - 4\beta^4 C_x u \exp(-\beta^2 C_x^2)}{(u\sqrt{\pi}\beta) \left\{ 1 + \operatorname{erf}(\beta u) + \frac{1}{u\sqrt{\pi}\beta} \exp(-\beta^2 u^2) - \frac{q_x}{5\sqrt{\pi}} \exp(-\beta^2 u^2) \right.} \\
& - \left[\frac{1}{u\sqrt{\pi}\beta} \exp(-\beta^2 u^2) + \frac{1}{2}[1 + \operatorname{erf}(\beta u)] \right] \tau_{xx} \\
& - \frac{1}{2} \left[\frac{1}{u\sqrt{\pi}\beta} \exp(-\beta^2 u^2) + [1 + \operatorname{erf}(\beta u)] \right] \tau_{yy} \\
& \left. - \frac{1}{2} \left[\frac{1}{u\sqrt{\pi}\beta} \exp(-\beta^2 u^2) + [1 + \operatorname{erf}(\beta u)] \right] \tau_{zz} \right\} = 0, \quad (\text{A.1})
\end{aligned}$$

$$C_{x,MAX} = \frac{\sqrt{(\beta u)^2 + 2} - \beta u}{2\beta}. \quad (\text{A.2})$$

The resulting normalized distribution is thus:

$$\frac{f_{SR}(C_x)}{f_{SR}(C_{x,MAX})} = \frac{2\beta(C_x + u) \exp\left(\frac{1}{2} + \frac{\beta u}{2} (\beta u - \sqrt{(\beta u)^2 + 2}) - \beta^2 C_x^2\right)}{\sqrt{2 + (\beta u)^2} + \beta u}. \quad (\text{A.3})$$

Note that since the terms in the denominator of (A.1) are independent of C_x , they simply scale the distribution and cancel in the normalization, thus the result in (A.3) is the same distribution used in the well-established sampling process for the equilibrium normal velocity component [2].

Appendix B

Perturbation expressed by flux quantities

For a gas mixture comprising species $(s, t) \in \mathbb{S}$, the Generalized Chapman-Enskog (GCE) perturbation $\phi_{GCE,s}$ is of the form [21, 57]:

$$\phi_{GCE,s} = -\frac{1}{n} \sum_t \mathbf{D}_s^t \cdot \mathbf{d}_t - \frac{1}{n} \mathbf{A}_s \cdot \nabla \log T - \frac{1}{n} \mathbf{A}_s^{(1)} \cdot \nabla \log T_1 - \frac{1}{n} \mathbf{B}_s : \nabla \mathbf{v} \quad (\text{B.1})$$

The functions \mathbf{D}_s^t , \mathbf{A}_s , $\mathbf{A}_s^{(1)}$ and \mathbf{B}_s are expanded in Sonine ($\mathcal{S}_v^{(n)}(\mathcal{C}^2)$) and Waldmann-Trübenbacher ($\mathcal{P}^{(p)}(\mathcal{E})$) Polynomials [57], resulting in functions which are expressed in terms of the trial functions as:

$$\mathbf{D}_s^t = (m_s/2k_b T_{tr})^{1/2} \sum_{p=0}^{n-1} d_{s,0}^{t(n)} \mathcal{S}_{3/2}^{(p)}(\mathcal{C}_s^2) \mathcal{C}_s \quad (\text{B.2})$$

$$\mathbf{A}_s = - (m_s/2k_b T_{tr})^{1/2} \sum_{rpq}^n a_{s,rpq} \mathcal{S}_{3/2}^{(r)}(\mathcal{C}_s^2) \mathcal{P}^{(p)}(\mathcal{E}_{rot}) \mathcal{P}^{(q)}(\mathcal{E}_{rot} - \mathcal{E}_{vib}) \mathcal{C}_s \quad (\text{B.3})$$

$$\mathbf{A}_s^{(1)} = - (m_s/2k_b T_{tr})^{1/2} \sum_r^n a_{s,r}^{(1)} \mathcal{P}^{(r)}(\mathcal{E}_{vib}) \mathcal{C}_s \quad (\text{B.4})$$

$$\mathbf{B}_s = \left(\mathcal{C}_s \mathcal{C}_s - \frac{1}{3} \mathcal{C}_s^2 \mathbb{I} \right) \sum_r^n b_{s,r} \mathcal{S}_{5/2}^{(r)}(\mathcal{C}_s^2) \quad (\text{B.5})$$

It can be shown that, to the first ($n = 1$) approximation, the multicomponent diffusion, viscosity and thermal conductivity coefficients may be related to the trial functions according to [57]:

$$D_{st} = \frac{1}{2n} d_{s,0}^{t(1)} \quad (\text{B.6})$$

$$K_{tr,s} = \frac{5k_b}{4}a_{s,100} \quad (\text{B.7})$$

$$K_{rot,s} = \frac{m_s c_{rot}}{2}a_{s,010} \quad (\text{B.8})$$

$$K_{vib,s} = \frac{m_s c_{vib}}{2}a_{s,1}^{(1)} \quad (\text{B.9})$$

$$\mu_s = \frac{k_b T_{tr}}{2}b_{s,0} \quad (\text{B.10})$$

We substitute these relations (C.8) - (C.12) into (C.2) - (C.7). Note that the function \mathbf{A}_s specifies the coefficients of translational and rotational thermal conductivity (considered as rapid processes), while the function $\mathbf{A}_s^{(1)}$ specifies the coefficient of vibrational thermal conductivity (considered as a slow process) [57]. In substitution of these relations, we evaluate the polynomials and arrive at the following forms of $\mathcal{S}_v^{(n)}$ and $\mathcal{P}^{(p)}$:

$$d_{s,0}^{t(1)} : \quad \mathcal{S}_{3/2}^{(p=0)}(\mathcal{C}_s^2) = 1 \quad (\text{B.11})$$

$$a_{s,100} : \quad \mathcal{S}_{3/2}^{(r=1)}(\mathcal{C}_s^2) = \frac{5}{2} - \mathcal{C}_s^2 \quad \mathcal{P}^{(p=0)}(\mathcal{E}_{rot}) = 1 \quad \mathcal{P}^{(q=0)}(\mathcal{E}_{rot} - \mathcal{E}_{vib}) = 1 \quad (\text{B.12})$$

$$a_{s,010} : \quad \mathcal{S}_{3/2}^{(r=0)}(\mathcal{C}_s^2) = 1 \quad \mathcal{P}^{(p=1)}(\mathcal{E}_{rot}) = \bar{\mathcal{E}}_{rot} - \mathcal{E}_{rot} \quad \mathcal{P}^{(q=0)}(\mathcal{E}_{rot} - \mathcal{E}_{vib}) = 1 \quad (\text{B.13})$$

$$a_{s,1}^{(1)} : \quad \mathcal{P}^{(r=1)}(\mathcal{E}_{vib}) = \bar{\mathcal{E}}_{vib} - \mathcal{E}_{vib} \quad (\text{B.14})$$

$$b_{s,0} : \quad \mathcal{S}_{5/2}^{(r=0)}(\mathcal{C}_s^2) = 1 \quad (\text{B.15})$$

Thus, the final forms of (C.2) - (C.7) expressed in terms of the transport coefficients are:

$$\mathbf{D}_s^t = (m_s/2k_b T_{tr})^{1/2} 2n D_{st} \mathcal{C}_s \quad (\text{B.16})$$

$$\mathbf{A}_{s,tr} = - (m_s/2k_b T_{tr})^{1/2} \frac{4K_{tr,s}}{5k_b} \left(\frac{5}{2} - \mathcal{C}_s^2 \right) \mathcal{C}_s \quad (\text{B.17})$$

$$\mathbf{A}_{s,rot} = -(m_s/2k_b T_{tr})^{1/2} \frac{2K_{rot,s}}{m_s c_{rot}} (\bar{\mathcal{E}}_{rot} - \mathcal{E}_{rot}) \mathcal{C}_s \quad (\text{B.18})$$

$$\mathbf{A}_{s,vib} = \mathbf{A}_s^{(1)} = -(m_s/2k_b T_{tr})^{1/2} \frac{2K_{vib,s}}{m_s c_{vib}} (\bar{\mathcal{E}}_{vib} - \mathcal{E}_{vib}) \mathcal{C}_s \quad (\text{B.19})$$

$$\mathbf{B}_s = \frac{2\mu_s}{k_b T_{tr}} \left(\mathcal{C}_s \mathcal{C}_s - \frac{1}{3} \mathcal{C}_s^2 \mathbb{I} \right) \quad (\text{B.20})$$

The perturbation in (C.1) may now be expressed in terms of the transport coefficients:

$$\begin{aligned} \phi_{GCE,s} = & -\frac{1}{n} \sum_t (m_s/2k_b T_{tr})^{1/2} 2n D_{st} \mathcal{C}_s \cdot \mathbf{d}_t \\ & -\frac{1}{n} (m_s/2k_b T_{tr})^{1/2} \frac{4K_{tr,s}}{5k_b} \left(\mathcal{C}_s^2 - \frac{5}{2} \right) \mathcal{C}_s \cdot \nabla \log T_{tr} \\ & -\frac{1}{n} (m_s/2k_b T_{tr})^{1/2} \frac{2K_{rot,s}}{m_s c_{rot}} (\mathcal{E}_{rot} - \bar{\mathcal{E}}_{rot}) \mathcal{C}_s \cdot \nabla \log T_{rot} \\ & -\frac{1}{n} (m_s/2k_b T_{tr})^{1/2} \frac{2K_{vib,s}}{m_s c_{vib}} (\mathcal{E}_{vib} - \bar{\mathcal{E}}_{vib}) \mathcal{C}_s \cdot \nabla \log T_{vib} \\ & -\frac{1}{n} \frac{2\mu_s}{k_b T_{tr}} \left(\mathcal{C}_s \mathcal{C}_s - \frac{1}{3} \mathcal{C}_s^2 \mathbb{I} \right) : \nabla \mathbf{v} \end{aligned} \quad (\text{B.21})$$

We are now in position to express the perturbation, $\phi_{GCE,s}$, in terms of the species diffusion flux, shear stress and heat flux quantities that are determined from the Navier-Stokes solution. Before doing this, we note that the first term on the right hand side in (B.21) involves an inner product of the particle thermal velocity vector $\mathcal{C}_s = (\mathcal{C}_{s,x}, \mathcal{C}_{s,y}, \mathcal{C}_{s,z})$ and the vector \mathbf{d}_t , which is known as the diffusion driving force and is defined as:

$$\mathbf{d}_t = \nabla \left(\frac{n_t}{n} \right) + \left(\frac{n_t}{n} - \frac{\rho_t}{\rho} \right) \nabla \log p \quad (\text{B.22})$$

Additionally, we can simplify the first term in (B.21) by introducing a diffusion

velocity, \mathbf{V}_s , which takes the form:

$$\mathbf{V}_s = - \sum_t D_{st} \mathbf{d}_t - D_{T,s} \nabla \log T \quad (\text{B.23})$$

Note that the diffusion velocity has contributions from both species diffusion (driven by gradients in concentration and pressure) as well as thermal diffusion (driven by gradients in temperature), but thermal diffusion is not considered in this work. Using the definition of the inverse most probable thermal speed for species s , $\beta_s = \sqrt{m_s/2k_b T_{tr}}$, we have for the perturbation $\phi_{GCE,s}$:

$$\begin{aligned} \phi_{GCE,s} = & 2\beta_s \mathbf{V}_s \cdot \mathcal{C}_s - \frac{1}{n} \beta_s \frac{4K_{tr,s}}{5k_b} \left(\mathcal{C}_s^2 - \frac{5}{2} \right) \mathcal{C}_s \cdot \nabla \log T_{tr} \\ & - \frac{1}{n} \beta_s \frac{2K_{rot,s}}{m_s c_{rot}} (\mathcal{E}_{rot} - \bar{\mathcal{E}}_{rot}) \mathcal{C}_s \cdot \nabla \log T_{rot} \\ & - \frac{1}{n} \beta_s \frac{2K_{vib,s}}{m_s c_{vib}} (\mathcal{E}_{vib} - \bar{\mathcal{E}}_{vib}) \mathcal{C}_s \cdot \nabla \log T_{vib} \\ & - \frac{1}{n} \frac{2\mu_s}{k_b T_{tr}} \left(\mathcal{C}_s \mathcal{C}_s - \frac{1}{3} \mathcal{C}_s^2 \mathbb{I} \right) : \nabla \mathbf{v} \end{aligned} \quad (\text{B.24})$$

After some trivial algebra, we can write the perturbation $\phi_{GCE,s}$ in terms of the Navier-Stokes species diffusion, shear stress, and heat fluxes using the following definitions and normalizations:

$$\mathbb{D}_s = \frac{\beta_s \rho_s \mathbf{V}_s}{\rho_s} = \frac{\beta_s \mathbf{D}_s^{NS}}{\rho_s} \quad (\text{B.25})$$

$$\tau_{ij,s} = \frac{\mu_s}{p_s} \left(\partial_j v_i + \partial_i v_j - \frac{2}{3} \partial_k v_k \delta_{ij} \right) = \frac{\tau_{ij,s}^{NS}}{p_s} \quad (\text{B.26})$$

$$q_{i,s} = - \frac{2\beta_s}{p_s} K_s \partial_i T = \frac{2\beta q_{i,s}^{NS}}{p_s} \quad (\text{B.27})$$

$$\tilde{q}_{int,i,s} = - \frac{2\beta_s}{\rho_s c_{int} T_{int}} K_s \partial_i T_{int} = \frac{2\beta_s q_{int,i,s}^{NS}}{\rho_s c_{int} T_{int}} \quad (\text{B.28})$$

Thus we arrive at our final expression of the perturbation $\phi_{GCE,s}$:

$$\begin{aligned}
\phi_{GCE,s}(\mathcal{C}_s, \mathcal{E}_{int}) = & 2(\mathbb{D}_{x,s}\mathcal{C}_{x,s} + \mathbb{D}_{y,s}\mathcal{C}_{y,s} + \mathbb{D}_{z,s}\mathcal{C}_{z,s}) \\
& + (q_{x,s}\mathcal{C}_{x,s} + q_{y,s}\mathcal{C}_{y,s} + q_{z,s}\mathcal{C}_{z,s}) \left(\frac{2}{5}\mathcal{C}_s^2 - 1 \right) \\
& + (\tilde{q}_{int,x,s}\mathcal{C}_{x,s} + \tilde{q}_{int,y,s}\mathcal{C}_{y,s} + \tilde{q}_{int,z,s}\mathcal{C}_{z,s}) (\mathcal{E}_{int,s} - \bar{\mathcal{E}}_{int,s}) \\
& - 2(\mathcal{C}_{x,s}\mathcal{C}_{y,s}\tau_{xy,s} + \mathcal{C}_{x,s}\mathcal{C}_{z,s}\tau_{xz,s} + \mathcal{C}_{y,s}\mathcal{C}_{z,s}\tau_{yz,s}) \\
& - \mathcal{C}_{x,s}^2\tau_{xx,s} - \mathcal{C}_{y,s}^2\tau_{yy,s} - \mathcal{C}_{z,s}^2\tau_{zz,s}
\end{aligned} \tag{B.29}$$

Appendix C

Formulation of Collision Integrals with VHS/VSS Cross Sections

The collision integrals used in the calculation of the transport coefficients follow the form in Chapman and Cowling (Equation (9.33,5)) [12]. The general form is given as:

$$\Omega_{st}^l(r) = \left(\frac{k_b T}{2\pi m_{st}^*} \right)^{1/2} \int_0^\infty e^{-\left(\frac{m_{st}^*}{2k_b T} \right) g^2} \left[\left(\frac{m_{st}^*}{2k_b T} \right)^{1/2} g \right]^{2r+3} \phi_{st}^l \left(\frac{m_{st}^*}{2k_b T} \right)^{1/2} dg, \quad (\text{C.1})$$

where ϕ_{st}^l represents a total (or averaged) cross-section, and is defined as:

$$\phi_{st}^l = 2\pi \int (1 - \cos^l \chi) b db. \quad (\text{C.2})$$

For the collision integrals considered in this work, the cross-sections are found by letting $l = 1, 2$. The cross-section corresponding to the case $l = 1$ is the diffusion cross-section:

$$\phi_{st}^1 = 2\pi \int (1 - \cos \chi) b db = \sigma_M. \quad (\text{C.3})$$

The cross-section corresponding to the case involving $l = 2$ is known as the viscous cross-section:

$$\phi_{st}^2 = 2\pi \int (1 - \cos^2 \chi) b db = \sigma_\mu. \quad (\text{C.4})$$

In terms of the VHS model, these transport cross-sections in (C.3), (C.4) are related to the total collision cross-section defined in Bird, Equation (2.32, 2.33)[2]:

$$\sigma_M = \sigma_T, \quad (C.5)$$

$$\sigma_\mu = \frac{2}{3}\sigma_T. \quad (C.6)$$

If we instead consider the VSS model, the transport cross-sections are related to the total collision cross-section (Bird, Equation (2.37, 2.38)) [2]:

$$\sigma_M = \frac{2}{\alpha + 1}\sigma_T, \quad (C.7)$$

$$\sigma_\mu = \frac{4\alpha}{(\alpha + 1)(\alpha + 2)}\sigma_T. \quad (C.8)$$

In the following, we consider the formulation of $\Omega_{st}^{(1)}(1)$ for a VHS cross-section; the remaining collision integrals may be determined in a similar manner. In setting $l = 1, r = 1$ in (C.1), we have:

$$\Omega_{st}^{(1)}(1) = \left(\frac{k_b T}{2\pi m_{st}^*}\right)^{1/2} \int_0^\infty e^{-\left(\frac{m_{st}^*}{2k_b T}\right)g^2} \left[\left(\frac{m_{st}^*}{2k_b T}\right)^{1/2} g\right]^5 \sigma_T \left(\frac{m_{st}^*}{2k_b T}\right)^{1/2} dg. \quad (C.9)$$

Now, for VHS/VSS molecules, the total cross-section is inversely proportional to a power of the relative speed. This relationship is expressed as (Bird, Equation 3.60)[2]:

$$\sigma_T = \sigma_{T,ref} \left(\frac{g}{g_{ref}}\right)^{-2\nu}. \quad (C.10)$$

Note that to remain consistent with notation, we've exchanged Bird's relative collision speed $c_r, c_{r,ref}$ with Chapman and Cowling's notation of g, g_{ref} .

Substituting (C.10) into (C.9) we obtain:

$$\Omega_{st}^{(1)}(1) = \left(\frac{k_b T}{2\pi m_{st}^*} \right)^{1/2} \int_0^\infty \exp \left(- \left(\frac{m_{st}^*}{2k_b T} \right) g^2 \right) \left[\left(\frac{m_{st}^*}{2k_b T} \right)^{1/2} g \right]^5 \sigma_{T,ref} \left(\frac{g}{g_{ref}} \right)^{-2\nu} \left(\frac{m_{st}^*}{2k_b T} \right)^{1/2} dg. \quad (C.11)$$

We can re-arrange the terms in (C.11) to achieve a simplified form of the collision integral in terms of the VHS parameters. First, we move the reference quantities outside of the integral and write (C.11) as:

$$\Omega_{st}^{(1)}(1) = \left(\frac{k_b T}{2\pi m_{st}^*} \right)^{1/2} \sigma_{T,ref} g_{ref}^{2\nu} \left(\frac{m_{st}^*}{2k_b T} \right)^\nu \int_0^\infty \exp \left(- \left(\frac{m_{st}^*}{2k_b T} \right) g^2 \right) \left[\left(\frac{m_{st}^*}{2k_b T} \right)^{1/2} g \right]^{5-2\nu} \left(\frac{m_{st}^*}{2k_b T} \right)^{1/2} dg. \quad (C.12)$$

We recognize that twice the integral in (C.12) is the gamma function $\Gamma(3 - \nu)$, so we can write (C.12) as:

$$\Omega_{st}^{(1)}(1) = \left(\frac{k_b T}{2\pi m_{st}^*} \right)^{1/2} \sigma_{T,ref} g_{ref}^{2\nu} \left(\frac{m_{st}^*}{2k_b T} \right)^\nu \left(\frac{1}{2} \right) \Gamma(3 - \nu). \quad (C.13)$$

The reference parameters present in (C.13) may be re-expressed in terms of the VHS parameters d_{ref} , T_{ref} and ω . Noting that $\nu = \omega - 1/2$ (Bird, Equation 3.67)[2], we can make the following substitutions for $\sigma_{T,ref}$ and $g_{ref}^{2\omega-1}$ (Bird, Equation 4.61)[2]:

$$\sigma_{T,ref} = \pi d_{ref}^2, \quad (C.14)$$

$$g_{ref}^{2\omega-1} = \frac{\left(\frac{2k_b T_{ref}}{m_{st}^*} \right)^{\omega-1/2}}{\Gamma(5/2 - \omega)}. \quad (C.15)$$

Thus we arrive at our final form for the collision integral $\Omega_{st}^{(1)}(1)$ in terms of the VHS reference parameters:

$$\Omega_{st}^{(1)}(1) = \frac{\pi}{2} d_{ref}^2 \left(\frac{k_b T}{2\pi m_{st}^*} \right)^{1/2} \left(\frac{T_{ref}}{T} \right)^{\omega-1/2} \left[\frac{\Gamma(7/2 - \omega)}{\Gamma(5/2 - \omega)} \right]. \quad (\text{C.16})$$

Appendix D

Nelder-Mead Initial Conditions and Convergence History Example

The Nelder-Mead algorithm is used to determine the set of VHS/VSS parameters that provide the best fit to the transport coefficients determined from the SCEBD/Gupta *et al.*-Yos models. The algorithm takes as input the variable parameters being fit, and uses an iterative search procedure over the parameter space to find the set of parameters which minimize the error in the transport coefficients. The search procedure is stopped when the convergence criteria, indicated by convergence in the values of the parameter set being fit, as well as convergence in the function values, are met. [46, 59] In this work, convergence is reached when the maximum value of the infinity norm of the simplex (a measure of convergence in set of parameters) *and* the corresponding difference in function values is less than or equal to 10^{-6} .

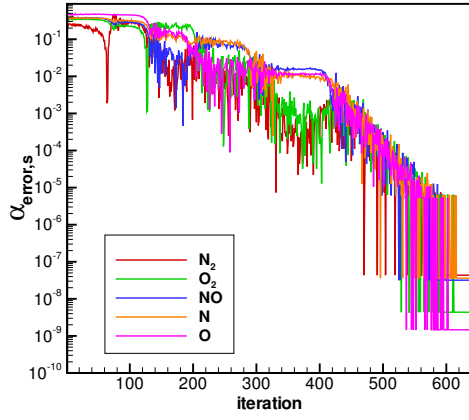
Since the initial values used for the first iteration of the search are somewhat arbitrary, it is important that the Nelder-Mead algorithm is capable of producing a consistent best-fit set of parameters that is independent of the parameter initialization. To demonstrate this, we consider the fitting of the α parameters from the collision-averaged VHS/VSS parameter set (from Table

4.1)). Recall that the common parameters d_{ref} and ω are determined from the fitting of the viscosity and translational thermal conductivity using the VHS model (in this case, the VSS reference diameters of O_2 , NO and O were relaxed slightly from their VHS values).

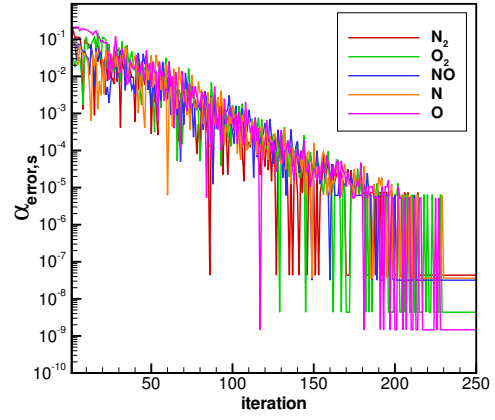
Table D.1: Predicted values of α (collision-averaged) for various α_0

	$\alpha_0 = 1.0$	$\alpha_0 = 1.5$	$\alpha_0 = 2.0$
N_2	1.3483	1.3483	1.3484
O_2	1.5471	1.5471	1.5476
NO	1.6180	1.6181	1.6188
N	1.6083	1.6085	1.6081
O	1.9014	1.9014	1.9017

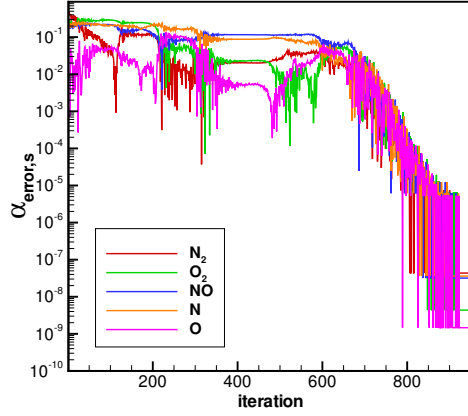
The α parameters were initialized to three different values of $\alpha = 1.0, 1.5, 2.0$, which span the physical limits of this parameter. The resulting best-fit values from the Nelder-Mead search are shown in Table D.1 for each species in the gas mixture, and the final parameter values obtained from the independent searches are in very good agreement, to within three decimal places. The corresponding convergence history of each parameter α is shown in Figure D.1 (a)-(c). These figures show the relative error in the value of α_s between the value at the current iteration and the final value. The Nelder-Mead algorithm converges most rapidly in the case where $\alpha_0=1.5$ for each species.



(a) Initial condition of $\alpha_0 = 1.0$



(b) Initial condition of $\alpha_0 = 1.5$



(c) Initial condition of $\alpha_0 = 2.0$

Figure D.1: Relative error of α_s as a function of iteration.

Appendix E

Computational Cost of CFD/Hybrid Solutions

The computational cost of the CFD and hybrid calculations are summarized below in Table E.1 for the full three-dimensional simulations presented in Chapter 5.

Table E.1: Computational Summary of CFD/Hybrid Simulations

CFD	Time (hrs.)	Cores	Memory (MB)	Cells	
Asym. (60 <i>km</i>)	33	96	392	3.2×10^6	—
Asym. (80 <i>km</i>)	30	96	323	2.6×10^6	—
Sym. (80 <i>km</i>)	53	80	620	3.5×10^6	—
Hybrid	Time (hrs.)	Cores	Memory (GB)	Cells	Particles
Asym. (60 <i>km</i>)	471	1440	1.4	5.46×10^8	2.3×10^{10}
Asym. (80 <i>km</i>)	144	1080	1.1	2.47×10^8	1.7×10^{10}
Sym. (80 <i>km</i>)	115	720	1.1	1.19×10^8	8.5×10^9

The full CFD solutions are presented in terms of the total computational time, the total number of cores used and estimated memory required per core, and the total number of finite volume cells comprising the computational domain. The hybrid solution is detailed in terms of the total computational time, the total number of cores used and (average) memory per core *at steady state*, as well as the total number of *steady-state* simulation particles and computational cells comprising the flowfield domain. The hybrid (DSMC) cal-

culations presented here are currently the largest simulations generated using the DAC code. It is emphasized, however, that these calculations were performed using a modified version of the DAC solver and libraries, to allow for calculations involving greater than 2.1×10^9 simulated particles.

Bibliography

- [1] J.D. Anderson. *Hypersonic and High Temperature Gas Dynamics*. AIAA, Inc., Reston, VA, 2000.
- [2] G.A. Bird. *Molecular Gas Dynamics and the Direct Simulation of Gas Flows*. Oxford University Press, Oxford, 1994.
- [3] F. G. Blottner, M. Johnson, and M. Ellis. Chemically reacting viscous flow program for multi-component gas mixtures. *Sandia Laboratories, Report SC-RR-70-754, Albuquerque*, December 1971.
- [4] C. Borgnakke and P. S. Larsen. Statistical collision model for monte carlo simulation of polyatomic gas mixture. *Journal of Computational Physics, Vol. 18, pp. 405-420*, 1975.
- [5] I.D. Boyd. Modeling backward chemical rate processes in the direct simulation monte carlo method. *Physics of Fluids, Vol. 19*, 2007.
- [6] I.D. Boyd, G. Chen, and G.V. Candler. Predicting failure of the continuum fluid equations in transitional hypersonic flows. *Physics of Fluids, Vol. 7, No. 1, pp 210-219*, 1995.
- [7] R. Brun. Transport properties in reactive gas flows. *AIAA Paper No. AIAA-88-2655*, 1988.

- [8] Tang C., Trumble K., Campbell C., Lessard V., and Wood W. Numerical simulations of the boundary layer transition flight experiment. *AIAA 2010-0453, 48th AIAA Aerospace Sciences Meeting and Exhibit, Orlando, FL*, 2010.
- [9] J.A. Camberos, C.R. Schrock, R.J. McMullan, and R.D. Branam. Development of continuum onset criteria with direct simulation monte-carlo using boltzmann’s h-theorem: Review and vision. *AIAA Paper No. 2006-2942*, 2006.
- [10] C. H. Campbell, M. Garske, J. Kinder, and S. A. Berry. Orbiter entry boundary layer flight testing. *AIAA 2008-0635, 46th AIAA Aerospace Sciences Meeting and Exhibit, Reno, NV*, 2008.
- [11] C. L. Chang and M. M. Choudhari. Hypersonic viscous flow over large roughness elements. *AIAA 2009-0173, 47th AIAA Aerospace Sciences Meeting and Exhibit, Orlando, FL*, 2009.
- [12] S. Chapman and T.G. Cowling. *The Mathematical Theory of Non-Uniform Gases*. Cambridge University Press, Cambridge, 1970.
- [13] S. Chigullapalli, A. Venkatramana, M.S. Ivanov, and A.A. Alexeenko. Entropy considerations in numerical simulations of non-equilibrium rarefied flows. *Journal of Computational Physics, Vol. 229, Issue 6*, 2010.
- [14] M. M. Choudhari, F. Li, and J. E. Edwards. Stability analysis of roughness array wake in a high-speed boundary layer. *AIAA 2009-0170, 47th*

AIAA Aerospace Sciences Meeting and Exhibit, Orlando, FL, 2009.

- [15] D. A. Copeland. New approximate formulas for viscosity and thermal conductivity of dilute gases. *AIAA Journal*, Vol. 41, No. 3, pp. 525-537, 2003.
- [16] S. J. Cubley and E. A. Mason. Atom-molecule and molecule-molecule potentials and transport collision integrals for high-temperature air species. *Physics of Fluids*, Vol. 18, pp. 1109-1111, 1975.
- [17] P. M. Danehy, A. P. Garcia, S. Borg, A. A. Dyakonov, S. A. Berry, J. A. (Wilkes) Inman, and D. W. Alderfer. Fluorescence visualization of hypersonic flow past triangular and rectangular boundary-layer trips. *AIAA 2007-0536, 45th AIAA Aerospace Sciences Meeting and Exhibit, Reno, NV*, 2007.
- [18] T. R. Deschenes and I. D. Boyd. Application of a modular particle-continuum method to partially rarefied, hypersonic flow. *27th International Symposium on Rarefied Gas Dynamics*, 2011.
- [19] T. R. Deschenes, T. D. Holman, I. D. Boyd, and T. E. Schwartzentruber. Analysis of internal energy transfer within a modular particle-continuum method. *AIAA Paper No. 2009-1216*, 2009.
- [20] A. Ern and V. Giovangigli. *Multicomponent Transport Algorithms*. Springer, Berlin, 1994.

- [21] J. H. Ferziger and H. G. Kaper. *Mathematical theory of transport processes in gases*. North-Holland Publishing Company, Amsterdam, Netherlands, 1972.
- [22] M.A. Gallis, J.R. Torczynski, and D.J. Rader. Molecular gas dynamics observations of chapman-enskog behavior and departures therefrom in nonequilibrium gases. *Physical Review E*, Vol. 69, 2004.
- [23] A. Garcia and W. Alder. Generation of the chapman-enskog distribution. *Journal of Computational Physics* 140 66, 1998.
- [24] A. Garcia and W. Wagner. Generation of the maxwellian inflow distribution. *Journal of Computational Physics* 217 693-708, 2006.
- [25] A.L. Garcia. *Numerical Methods for Physics*. Prentice Hall, New Jersey, 2000.
- [26] D. M. Gibson, T. S. Spisz, J. C. Taylor, J. N. Zalameda, T. J. Horvath, D. M. Tomek, A. B. Tietjen, S. Tack, and B. Bush. Hythirm radiance modeling and image analyses in support of sts-119, sts-125 and sts-128 space shuttle hypersonic re-entries (invited). *AIAA 2010-0245, 48th AIAA Aerospace Sciences Meeting and Exhibit, Orlando, FL*, 2010.
- [27] N. E. Gimelshein, S. F. Gimelshein, and D. A. Levin. Vibrational relaxation rates in the direct simulation monte carlo method. *Physics of Fluids*, Vol. 14, No. 12, 2002.

- [28] C. E. Glass and T. J. Horvath. Comparison of a 3d cfd-dsmc solution methodology with a wind tunnel experiment. *NASA/TM-2002-211777*, 2002.
- [29] T. Gökçen and R. W. MacCormack. Nonequilibrium effects for hypersonic transitional flows using continuum approach. *AIAA 1989-0461, 27th AIAA ASM Conference, Reno, NV*, 1989.
- [30] M. A. Green, C. W. Rowley, and G. Haller. Detection of lagrangian coherent structures in three-dimensional turbulence. *Journal of Fluid Mechanics, Vol. 572, pp. 111-120*, 2007.
- [31] G. Groskopf, M. Kloker, and O. Marxen. Bi-global crossplane stability analysis of high-speed boundary-layer flows with discrete roughness. *Proceedings of the Seventh IUTAM Symposium on Laminar-Turbulent Transition, Stockholm, Sweden*, 2010.
- [32] G. Groskopf, M. Kloker, and K. A. Stephani. Temperature/rarefaction effects in hypersonic boundary-layer flow with an oblique roughness element. *AIAA 2011-3251, 41st AIAA Fluid Dynamics Conference and Exhibit, Honolulu, HI*, 2011.
- [33] G. Groskopf, M. Kloker, K. A. Stephani, O. Marxen, and G. Iaccarino. Hypersonic flows with discrete surface roughness and their stability properties. In *Proceedings of the 2010 CTR Summer Program, Center for Turbulence Research, Stanford University*, 2010.

- [34] R. Gupta, J. Yos, and R. Thompson. A review of reaction rates and thermodynamics and transport properties for the 11-species air model for chemical and thermal nonequilibrium calculations to 30000k. *NASA TM 101528*, February 1989.
- [35] G. Haller. An objective definition of a vortex. *Journal of Fluid Mechanics*, Vol. 525, pp. 1-26, 2005.
- [36] D. Hash and H. Hassan. Assessment of schemes for coupling monte carlo and navier-stokes solution methods. *Journal of Thermophysics and Heat Transfer*, Vol. 10, No. 2, April-June, 1996.
- [37] H. A. Hassan and D. B. Hash. A generalized hard-sphere model for monte carlo simulations. *Physics of Fluids A*, Vol. 5, pp. 738-744, 1993.
- [38] C. Hirschfelder, J. Curtiss and R. Bird. *Molecular Theory of Gases and Liquids*. John Wiley & Sons Inc, New York, 1967.
- [39] T.D. Holman and I.D. Boyd. Effects of continuum breakdown on the surface properties of a hypersonic sphere. *Journal of Thermophysics and Heat Transfer*, Vol. 23, No. 4, pp 660-673, 2009.
- [40] T.D. Holman and I.D. Boyd. Effects of continuum breakdown on hypersonic aerothermodynamics for reacting flow. *Physics of Fluids*, Vol. 23, 2011.

- [41] T.D. Holman and I.D. Boyd. Effects of continuum breakdown on hypersonic aerothermodynamics for reacting flow. *Physics of Fluids*, Vol. 23, 2011.
- [42] J. C. R. Hunt, A. Wray, and P. Moin. Eddies, stream and convergence zones in turbulent flows. *Center for Turbulence Research Report, CTR-S88*, 1988.
- [43] K. Koura and H. Matsumoto. Variable soft sphere molecular model for inverse-power-law or lennard-jones potential. *Physics of Fluids A*, Vol. 3 pp. 2459-2465, 1991.
- [44] E. V. Kustova and E. A. Nagnibeda. The influence of non-boltzmann vibrational distribution on thermal conductivity and viscosity. *Molecular Physics and Hypersonic Flows*, Vol. 482, pp. 383-392, 1996.
- [45] E. V. Kustova, E. A. Nagnibeda, and A. Chikhaoui. On the accuracy of non-equilibrium transport coefficients calculation. *Chemical Physics*, Vol. 270, No. 3, pp. 459-469, 2001.
- [46] J. Lagarias, J. Reeds, M. Wright, and P. Wright. Convergence properties of the nelder-mead simplex method in low dimensions. *SIAM Journal on Optimization*, Vol. 9, No. 1, pp.112-147, 1998.
- [47] G. Lebeau. A user guide for the dsmc analysis code (dac) software. *Revision DAC97-L, NASA JSC*, October 2002.

- [48] G. J. LeBeau and F. E. III Lumpkin. Application highlights of the dsmc analysis code (dac) software for simulating rarefied flows. *Computer Methods in Applied Mechanics and Engineering*, Vol. 191, Issues 6-7 pp. 595-609, December 2001.
- [49] G.J. LeBeau. A parallel implementation of the direct simulation monte carlo method. *Computer Methods in Applied Mechanics and Engineering*, Vol. 174, Issues 3-4 pp. 319-337, May 1999.
- [50] C. R. Lilley and M. N. Macrossan. Methods for implementing the stream boundary condition in dsmc computations. *International Journal for Numerical Methods in Fluids*, Vol. 42, Issue 12, pp. 1363-1371, 2003.
- [51] T. E. Magin. A model for inductive plasma wind tunnels. *Ph.D. thesis, Université Libre de Bruxelles (ULB) and von Kármán Institute for Fluid Dynamics, Rhode-Saint Genèse, Belgium*, 2004.
- [52] T. E. Magin and G. Degrez. Transport algorithms for partially ionized and unmagnetized plasmas. *Journal of Computational Physics*, Vol. 198, No. 2, 2004.
- [53] E. A. Mason, R. J. Munn, and F. J. Smith. Transport coefficients of ionized gases. *Physics of Fluids*, Vol. 10, No. 8, 1967.
- [54] K. Miki, M. Panesi, E. Prudencio, and S. Prudhomme. Estimation of the nitrogen ionization reaction rate using east data and bayesian model analysis. *Physics of Plasmas*, Vol. 19, No. 2, 2012.

- [55] K. Miki, M. Panesi, E. Prudencio, and S. Prudhomme. Probabilistic models and uncertainty quantification for the ionization reaction rate of atomic nitrogen. *Journal of Computational Physics*, Vol. 231, No. 9, 2012.
- [56] R. C. Millikan and D. R. White. Systematics of vibrational relaxation. *Journal of Chemical Physics*, Vol. 39, No. 12, pp 3209-3213, 1963.
- [57] E. Nagnibeda and E. Kustova. *Non-equilibrium Reacting Gas Flows: Kinetic Theory of Transport and Relaxation Processes*. Springer-Verlag, Berlin, Germany, 2009.
- [58] NASA. Sts-119 infrared image. <http://spaceflightnow.com/shuttle/sts119/090329blt/>, 2009.
- [59] J. Nelder and R. Mead. A simplex method for function minimization. *Computer Journal* 7, pp. 308-313, 1965.
- [60] G. E. Palmer and M. J. Wright. Comparison of methods to compute high-temperature gas viscosity. *Journal of Thermophysics and Heat Transfer*, Vol. 17, No. 2, 2003.
- [61] C. Park. On convergence of computation of chemically reacting flows. *AIAA 85-0247, 23rd Aerospace Sciences Meeting, Reno, NV*, 1985.
- [62] C. Park. Review of chemical-kinetic problems of future nasa missions, i: Earth entries. *Journal of Thermophysics and Heat Transfer*, Vol. 7, No. 3, 1993.

- [63] J.G. Parker. Rotational and vibrational relaxation in diatomic gases. *The Physics of Fluids*, Vol. 2, No. 4, 1959.
- [64] NASA Ames (private communication with Chun Tang). Smooth oml database for shuttle orbiter. 2011.
- [65] Roveda R., D. B. Goldstein, and P. L. Varghese. Hybrid euler/dsmc approach for continuum/rarefied flows. *Journal of Spacecraft and Rockets*, Vol. 35, No. 4, May-June 1998.
- [66] J. D. Ramshaw and C. H. Chang. Friction-weighted self-consistent effective binary diffusion approximation. *Journal of Non-Equilibrium Thermodynamics*, Vol. 21, 1996.
- [67] E. Reshotko and A. Tumin. Role of transient growth in roughness-induced transition. *AIAA Journal* Vol. 42 No. 4, April 2004.
- [68] D. P. Rizzetta and M. R. Visbal. Direct numerical simulations of flow past an array of distributed roughness elements. *AIAA 2006-3527, 36th AIAA Fluid Dynamics Conference and Exhibit, San Francisco, CA*, 2006.
- [69] R. Roveda, D. B. Goldstein, and P. L. Varghese. Hybrid euler/direct simulation monte carlo calculation for unsteady slit flow. *Journal of Spacecraft and Rockets*, Vol. 37, No. 6, 2000.
- [70] S. P. Schneider. Effects of roughness on hypersonic boundary-layer transition. *AIAA 2007-0305, 45th AIAA Aerospace Sciences Meeting and Exhibit, Reno, NV*, 2007.

- [71] T.E. Schwartzentruber, L.C. Scalabrin, and I.D. Boyd. A modular particle-continuum numerical method for hypersonic non-equilibrium gas flows. *Journal of Computational Physics*, Vol. 225, Issue 1, pp 1159-1174, 2007.
- [72] T.E. Schwartzentruber, L.C. Scalabrin, and I.D. Boyd. Hybrid particle-continuum simulations of hypersonic flow over a hollow cylinder-flare geometry. *AIAA Journal* Vol. 46, No. 8 pp 2086-2095, 2008.
- [73] T.E. Schwartzentruber, L.C. Scalabrin, and I.D. Boyd. Hybrid particle-continuum simulations of nonequilibrium hypersonic blunt-body flowfields. *Journal of Thermophysics and Heat Transfer*, Vol. 22, No.1, 2008.
- [74] T.E. Schwartzentruber, L.C. Scalabrin, and I.D. Boyd. Multiscale particle-continuum simulations of hypersonic flow over a planetary probe. *Journal of Spacecraft and Rockets*, Vol. 45, No. 6, pp 1196-1206, 2008.
- [75] J. Stallcop, H. Partridge, and E. Levin. Collision integrals for the interaction of the ions of nitrogen and oxygen in a plasma at high temperatures and pressures. *Physics of Fluids B*, Vol. 4, No. 2, 1992.
- [76] J. R. Stallcop, H. Partridge, and E. Levin. Effective potential energies and transport cross sections for interactions of hydrogen and nitrogen. *Physical Review A*, Vol. 62, 2000.
- [77] J. R. Stallcop, H. Partridge, and E. Levin. Effective potential energies and transport cross sections for atom-molecule interactions of nitrogen

and oxygen. *Physical Review A*, Vol. 64, 2001.

- [78] K. A. Stephani and D. B. Goldstein. Dns study of transient disturbance growth and bypass transition due to realistic roughness. *AIAA 2009-0585, 47th AIAA Aerospace Sciences Meeting and Exhibit, Orlando, FL*, 2009.
- [79] K. A. Stephani, D. B. Goldstein, and P. L. Varghese. Effects of rarefaction on hypersonic boundary layer flow over discrete surface roughness. *AIAA 2010-0456, 48th AIAA Aerospace Sciences Meeting and Exhibit, Orlando, FL*, 2010.
- [80] K. A. Stephani, D. B. Goldstein, and P. L. Varghese. Development of a hybrid dsmc/navier-stokes solver with application to the sts-119 boundary layer transition flight experiments. *AIAA 2011-0534, 49th AIAA Aerospace Sciences Meeting and Exhibit, Orlando, FL*, 2011.
- [81] K. A. Stephani, D. B. Goldstein, and P. L. Varghese. Parametric study of hypersonic boundary layer flow over discrete surface roughness using a hybrid dsmc/navier-stokes solver. 2011.
- [82] K. A. Stephani, D. B. Goldstein, and P. L. Varghese. Consistent treatment of transport properties for five-species air dsmc/navier-stokes applications. *Physics of Fluids (in press)*, 2012.
- [83] K. A. Stephani, D. B. Goldstein, and P. L. Varghese. Generation of a hybrid dsmc/navier-stokes solution via a non-equilibrium surface reservoir

- approach. *Journal of Computational Physics (accepted for publication)*, 2012.
- [84] D. A. Stewart. Surface catalysis and characterization of proposed candidate tps for access-to-space vehicles. *NASA TM 112206*, July 1997.
 - [85] J. S. Strand and D. B. Goldstein. Global sensitivity analysis for dsmc simulations of hypersonic shocks. *submitted to Journal of Computational Physics*, 2012.
 - [86] C. R. Wilke. A viscosity equation for gas mixtures. *Journal of Chemical Physics, Vol. 18, No. 4, pp. 517-519*, 1950.
 - [87] M. Wright, T. White, and N. Mangini. Data parallel line relaxation (dplr) code user manual acadia version 4.01.1. *NASA/TM-2009-215388*, 2009.
 - [88] M. J. Wright, G. V. Candler, and D. Bose. Data-parallel line relaxation method for the navier-stokes equations. *AIAA Journal, Vol. 36, No. 9*, September 1998.
 - [89] J.M. Yos. Approximate equations for the viscosity and translational thermal conductivity of gas mixtures. *Report AVSSD-0112-67-RM, AVCO Missile Systems Division*, 1967.

Vita

Kelly Ann Stephani was born on February 1, 1983 in Chilton, WI to Edward E. and Jane M. (Kuehnl) Stephani. She received her Bachelor of Aerospace Engineering and Engineering Mechanics Degree from the University of Minnesota in 2005. After participating in a summer research program through Caltech at the Jet Propulsion Laboratory, she joined the graduate program at The University of Texas at Austin in the Fall of 2005. She received a Master's Degree in Aerospace Engineering in 2006, and completed her Ph.D. studies under the supervision of Professor Philip Varghese (Department Chair) and Professor David Goldstein in the Aerospace Engineering Department. This research was made possible through support from the NASA NRA and the CTR Summer Program at Stanford University.

Permanent address: 6500 Champion Grandview Way
Austin, Texas 78750

This dissertation was typeset with L^AT_EX[†] by the author.

[†]L^AT_EX is a document preparation system developed by Leslie Lamport as a special version of Donald Knuth's T_EX Program.